

Investigation of Fouling in Wavy-Fin Exhaust Gas Recirculators

by

Nagendra Krishnamurthy

A thesis submitted to the faculty of
Virginia Polytechnic Institute and State University
in partial fulfillment of the degree of

Master of Science
in
Mechanical Engineering

Danesh K. Tafti – Chair

Thomas E. Diller

Mark R. Paul

April 23, 2010

Blacksburg, Virginia, USA, 2010

Keywords: Wavy channel flow, Thermophoresis, Soot particle deposition, Wall temperature gradient,
Exhaust gas recirculator fouling

Nagendra Krishnamurthy © 2010

Abstract

Investigation of Fouling in Wavy-Fin Exhaust Gas Recirculators

Nagendra Krishnamurthy

This dissertation presents a detailed account of the study undertaken on the subject of fouling of Exhaust Gas Recirculator (EGR) coolers. The fouling process in EGR coolers is identified to be due to two primary reasons – deposition of fine soot particles and condensation of hydrocarbons known as dry soot and wet soot fouling, respectively. Several numerical simulations are performed to study the fouling process. Preliminary analysis of the particle forces for representative conditions reveal that drag, thermophoresis and Brownian forces are the significant transport mechanisms and among them, the deposition process is dominated by thermophoresis. Soot deposition in a representative turbulent plain channel shows a direct relationship of the amount of deposition with the near-wall temperature gradient. Subsequently, periodic and developing flow simulations are performed on a wavy channel geometry, a common EGR design for various Reynolds numbers and thermal boundary conditions. Constant heat flux boundary condition is used in the periodic fully-developed calculations, which assist in establishing various deposition trends. The wavy nature of the walls is noted to affect the fouling process, resulting in specific deposition patterns. For the lower Reynolds number flows, significantly higher deposition is observed due to the higher particle residence times. On the other hand, the developing flow calculations facilitate the use of wall temperature distributions that typically exist in EGR coolers. The linear dependence of the amount of deposition on the near-wall temperature gradient or in other words, the heat flux, is ascertained. It is also observed in all the calculations, that for the sub-micron soot particles considered, the deposition process is almost independent of the particle size. In addition, the nature of the flow and heat transfer characteristics and the transition to turbulence in a developing wavy channel are studied in considerable detail. Finally, a study on the condensation of heavy hydrocarbons is undertaken as a

post-processing step, which facilitates the prediction of the spatial distribution and time-growth of the combined fouling layer. From the calculations, the maximum thickness of the dry soot layer is observed to be near the entrance, whereas for the wet soot layer, the peak is found to be towards the exit of the EGR cooler. Further, parametric studies are carried out to investigate the effect of various physical properties and inlet conditions on the process of fouling.

Acknowledgements

To be able to complete the work I am presenting for my Masters, it has been a result of the help and support of a number of people. I would like to take this opportunity to thank everybody who has been directly or indirectly involved in this effort.

First of all, I would like to thank my advisor Dr. Danesh K. Tafti. He has been an enormous source of encouragement and support through the two year period. He has patiently answered all the questions I have had and been a great source of knowledge to me. I have always looked up to him for guidance and motivation to do the best in whatever I do. I would like to thank him again, for all his efforts – if not for him, this work would not have been possible.

I also thank Dr. Thomas Diller and Dr. Mark Paul for taking time off their busy schedules to be on my committee and reviewing my work.

I am grateful to Modine Manufacturing Company and US Army for funding this work. I would especially like to thank Dr. Aroon K. Viswanathan with whom I have been involved in a lot of technical discussions through the period of this project. His constant inputs and enormous technical expertise always helped in making sure that I was heading on the right path.

My colleagues in the lab – Pradeep Gopalakrishnan, Mohammad Elyyan, Sai Shrinivas, Naresh Selvarasu, Jose Tijiboy, Sunil Patil, Amit Amritkar, Kohei Takamuku, Jonathan Cowan, Vivek Sethapati, Surya Deb and Kamal Viswanath have all helped me through the numerous technical arguments and brainstorming sessions we have had. My roommates Amol, Avinash and Mahesh with whom I have spent the last two years of my life. I thank them all, for without them being around, it would have been a really tough journey for me.

Last but not the least, I am indebted to my family and friends who have inculcated the belief in me that I could go this far and made me always strive for the higher echelons in life.

Table of Contents

Abstract	ii
Acknowledgements	iv
Table of Contents	v
List of figures.....	viii
List of tables	xiii
Nomenclature.....	xiv
Chapter 1 Introduction.....	1
Chapter 2 Numerical methodology	7
2.1 Carrier phase	7
2.1.1 Governing equations	7
2.1.2 Governing equations in generalized coordinates	8
2.1.3 Fully-developed periodic flow.....	8
2.2 Discrete phase	10
2.2.1 Particle forces	10
2.2.2 Particle deposition model	11
2.2.3 Dispersed phase in periodic geometries	11
Chapter 3 Soot particle deposition in a turbulent plain channel	13
3.1 Introduction	13
3.2 Methodology	15
3.2.1 Carrier phase.....	15
3.2.2 Dispersed phase	16
3.3 Results and discussion	17
3.3.1 Turbulent channel flow	17
3.3.2 Relative effect of different particle forces.....	19

3.3.3 Particle deposition for typical operating conditions	22
3.3.4 Effect of temperature gradient on particle deposition	24
3.4 Conclusions	25
Chapter 4 Soot particle deposition in a periodic wavy channel	26
4.1 Introduction	26
4.2 Methodology	26
4.3 Geometry and computational grid	27
4.4 Validation.....	28
4.5 Effect of various particle forces	29
4.6 Results and discussion	29
4.6.1 Flow features	30
4.6.2 Base results.....	33
4.6.3 Effect of channel geometry	35
4.6.4 Effect of Reynolds number.....	38
4.6.5 Deposition trends over time and space.....	41
4.6.6 Effect of wall temperature gradient	43
4.7 Summary and conclusions	46
Chapter 5 Soot particle deposition in a developing wavy channel.....	48
5.1 Introduction	48
5.2 Methodology	48
5.3 Geometry and computational grid	49
5.4 Validation.....	50
5.5 Results and discussion	50
5.5.1 Flow features	51
5.5.2 Soot deposition with constant wall temperature	57

5.5.3 Soot deposition with varying wall temperature	60
5.5.4 Effect of wall temperature gradient	63
5.6 Summary and conclusions	64
Chapter 6 Prediction of EGR fouling – A post-processing step	66
6.1 Dry soot fouling layer	66
6.2 Wet soot fouling layer	68
6.2.1 Mole fraction and saturated mole fraction.....	68
6.2.2 Relationship of saturation pressure and saturation temperature	69
6.2.3 Hydrocarbon condensation.....	70
6.3 Fouling layer removal.....	71
6.4 Post-processing methodology	72
6.4.1 Geometry and notations	72
6.4.2 Assumptions	73
6.4.3 Methodology	74
6.5 Results and discussion	75
6.5.1 Base calculations	77
6.5.2 Parametric studies	82
6.6 Summary and conclusions	89
Appendix A Particle forces.....	91
Bibliography	94

List of figures

Figure 3-1 (a) RMS Fluctuations of normal turbulent stresses; (b) turbulent shear stress	18
Figure 3-2 Non-dimensional force magnitudes on particles of size (a) 10 nm and (b) 100 nm particles ($Re_{D_H} = 11200$, $T_w^* = 150 \text{ }^\circ\text{C}$, $T_g^* = 600 \text{ }^\circ\text{C}$).....	20
Figure 3-3 Comparison of depositions observed against stream-wise location of deposition for 10 nm particles ($Re_{D_H} = 11200$, $T_w^* = 150 \text{ }^\circ\text{C}$, $T_g^* = 600 \text{ }^\circ\text{C}$)	22
Figure 3-4 Plot of normalized percentage deposition with stream-wise location of deposition for 10 and 100 nm particles ($Re_{D_H} = 11200$, $T_w^* = 150 \text{ }^\circ\text{C}$, $T_g^* = 600 \text{ }^\circ\text{C}$).....	23
Figure 3-5 Normalized percentage deposition for every 80 length units along stream-wise direction for various temperature gradients	24
Figure 4-1 Geometric specifications of the wavy channel geometry and the near-wall grid.....	28
Figure 4-2 Iso-surfaces of coherent vorticity and time-averaged contour plots of non- dimensional u-velocity at different Reynolds numbers	31
Figure 4-3 Non-dimensional time-averaged u-velocity profiles at $x/L_x = 0.125$, 0.25 and 0.50 for $Re_{D_H} = 10000$	32
Figure 4-4 Local Nusselt number distribution along the top and bottom walls for different Reynolds numbers.....	33
Figure 4-5 Plot of normalized percentage deposition observed along stream-wise direction for 10 and 100 nm particles for $Re_{D_H} = 10000$, $T_g^* = 600 \text{ }^\circ\text{C}$ and $T_w^* = 150 \text{ }^\circ\text{C}$	34
Figure 4-6 100 nm soot particle depositions super-imposed onto one geometric period for $Re_{D_H} = 10000$, $T_g^* = 600 \text{ }^\circ\text{C}$ and $T_w^* = 150 \text{ }^\circ\text{C}$; red – top wall depositions and violet – bottom wall depositions	36

Figure 4-7 Percentage of soot particle depositions plotted against the location of deposition, along with the stream-wise direction on the top wall for $Re_{D_H} = 10000$, $T_g^* = 600 \text{ } ^\circ\text{C}$ and $T_w^* = 150 \text{ } ^\circ\text{C}$	36
Figure 4-8 Percentage of soot particle depositions plotted against the location of deposition, along with the stream-wise direction on the bottom wall for $Re_{D_H} = 10000$, $T_g^* = 600 \text{ } ^\circ\text{C}$ and $T_w^* = 150 \text{ } ^\circ\text{C}$	37
Figure 4-9 Local Nusselt number distribution on the top and bottom walls for $Re_{D_H} = 10000$	38
Figure 4-10 Plot of normalized percentage deposition of 100 nm soot particles along stream-wise direction for different Reynolds numbers with $T_g^* = 600 \text{ } ^\circ\text{C}$ and $T_w^* = 150 \text{ } ^\circ\text{C}$	40
Figure 4-11 Plot of percentage deposition on top wall for 100 nm soot particles at different Reynolds numbers with $T_g^* = 600 \text{ } ^\circ\text{C}$ and $T_w^* = 150 \text{ } ^\circ\text{C}$	40
Figure 4-12 Plot of percentage of depositions on south wall for 100 nm soot particles at different Reynolds numbers with $T_g^* = 600 \text{ } ^\circ\text{C}$ and $T_w^* = 150 \text{ } ^\circ\text{C}$	41
Figure 4-13 Plot of percentage deposition observed for 100 nm soot particles against physical time for different Reynolds numbers with $T_g^* = 600 \text{ } ^\circ\text{C}$ and $T_w^* = 150 \text{ } ^\circ\text{C}$	42
Figure 4-14 Plot of percentage deposition observed for 100 nm soot particles against stream-wise location of deposition for different Reynolds numbers with $T_g^* = 600 \text{ } ^\circ\text{C}$ and $T_w^* = 150 \text{ } ^\circ\text{C}$	42
Figure 4-15 Plot of percentage of depositions for every 5 stream-wise pitches along the flow direction against the ratio of wall temperature gradient to reference fluid temperature ($Re_{D_H} = 10000$)	44
Figure 4-16 Distribution of percentage deposition on a periodic geometry on the top wall for $Re_{D_H} = 10000$	45
Figure 4-17 Distribution of percentage deposition on a periodic geometry on the bottom wall for $Re_{D_H} = 10000$	46

Figure 5-1 Geometric specifications of the wavy channel used in the calculations	50
Figure 5-2 Time-averaged velocity and modified temperature profiles at $x/L_x = 0.5$ in the initial six pitches for $Re_{D_H} = 1000$ and 3800	52
Figure 5-3 Iso-surfaces of coherent vorticity (value = 3) in the initial four pitch and contour plots of u-velocities in 2 nd and 8 th pitches for $Re_{D_H} = 3800$	54
Figure 5-4 Iso-surfaces of coherent vorticity (value = 2) in the initial four pitch and contour plots of u-velocities in 2 nd and 8 th pitches for $Re_{D_H} = 1000$	55
Figure 5-5 Average Nusselt number distribution for every stream-wise pitch for $Re_{D_H} = 1000$ and 3800	56
Figure 5-6 Normalized percentage deposition along the developing channel for 10 and 100 nm particles at $Re_{D_H} = 3800$ with $T_w^* = 150$ °C and $T_g^* = 600$ °C	58
Figure 5-7 Number of depositions observed on the top wall super-imposed onto a single stream-wise pitch (starting from 3 rd pitch)	59
Figure 5-8 Number of depositions observed on the bottom wall super-imposed onto a single stream-wise pitch (starting from 3 rd pitch)	59
Figure 5-9 Wall temperature distribution used in the calculations	60
Figure 5-10 Normalized deposition fraction for 100 nm soot particles along the developing channel with varying wall temperature distribution at $Re_{D_H} = 3800$	61
Figure 5-11 Normalized deposition fraction for 100 nm soot particles along the developing channel with varying wall temperature distribution at $Re_{D_H} = 1000$	62
Figure 5-12 Percentage deposition observed on the top and bottom walls super-imposed onto a single stream-wise pitch for $Re_{D_H} = 3800$ and 1000	63
Figure 5-13 Dependence of normalized deposition fraction on the wall temperature gradient for $Re_{D_H} = 3800$	64

Figure 6-1 Normalized deposition fractions for different heat flux values obtained from the developing flow calculations and the corresponding linear correlations for $Re_{D_H} = 3800$ and 1000.....	67
Figure 6-2 Relationship of saturation pressure with saturation temperatures for 2-methylpentacosane, n-hexacosane and n-heptacosane	70
Figure 6-3 Representative sketch of the geometry for fouling layer prediction	73
Figure 6-4 Thickness of dry soot layer on the EGR cooler surface for $Re_{D_H} = 3800$ for various hours of operation	78
Figure 6-5 Thickness of wet soot layer on the EGR cooler surface for $Re_{D_H} = 3800$ at various hours of operation	80
Figure 6-6 Thickness of dry soot layer on the EGR cooler surface for $Re_{D_H} = 1000$ after various operational hours.....	81
Figure 6-7 Thickness of wet soot layer on the EGR cooler surface for $Re_{D_H} = 1000$ after various operational hours	82
Figure 6-8 Dry soot thickness after 5 hours of operation of the EGR cooler predicted for different values of thermal conductivity of exhaust gas for $Re_{D_H} = 3800$	83
Figure 6-9 Wet soot thickness after 5 hours of operation of the EGR cooler predicted for different values of thermal conductivity of exhaust gas for $Re_{D_H} = 3800$	84
Figure 6-10 Dry soot thickness after 5 hours of operation of the EGR cooler predicted for different values of thermal conductivity of fouling layer for $Re_{D_H} = 3800$	85
Figure 6-11 Wet soot thickness after 5 hours of operation of the EGR cooler predicted for different values of thermal conductivity of fouling layer for $Re_{D_H} = 3800$	85

Figure 6-12 Dry soot thickness after 5 hours of operation of the EGR cooler predicted for different values of inlet gas temperatures of hydrocarbon species of fouling layer for $Re_{D_H} = 3800$	86
Figure 6-13 Wet soot thickness after 5 hours of operation of the EGR cooler predicted for different values of inlet gas temperatures of hydrocarbon species of fouling layer for $Re_{D_H} = 3800$	87
Figure 6-14 Dry soot thickness after 5 hours of operation of the EGR cooler predicted for different values of initial concentration of hydrocarbon species of fouling layer for $Re_{D_H} = 3800$	88
Figure 6-15 Wet soot thickness after 5 hours of operation of the EGR cooler predicted for different values of initial concentration of hydrocarbon species of fouling layer for $Re_{D_H} = 3800$	88

List of tables

Table 3.1 Comparison of turbulent channel flow results with DNS and Correlations	19
Table 3.2 Comparison of orders of magnitude of different particle forces in representative conditions ($Re_{D_H} = 11200$, $T_w^* = 150 \text{ }^\circ\text{C}$, $T_g^* = 600 \text{ }^\circ\text{C}$).....	20
Table 3.3 Particle and fluid properties used in the calculations	21
Table 4.1 Values of particle and gas properties	30
Table 4.2 Coefficient of friction and Nusselt number for different Reynolds numbers	32
Table 4.3 Different Reynolds numbers with the corresponding Nusselt numbers calculated and particle Stokes numbers.....	38
Table 4.4 Temperature gradients, ratio of temperature gradient to reference temperature and the calculated normalized deposition fractions and preferential deposition values on the top wall for different wall temperatures for $Re_{D_H} = 10000$	43
Table 5.1 Properties of particles used in all the calculations	51
Table 6.1 Exhaust gas, particle properties and flow parameters used in the calculations	75

Nomenclature

A_c	Cross-sectional area
A_s	Surface area
c	Mean molecular velocity
C_f	Skin-friction coefficient
C_m	Millikan's modification to Stokes' drag law
d	Diameter
D_H	Hydraulic diameter
F	Force
Fr	Froude number
h	Heat transfer coefficient
k_b	Boltzmann constant
Kn	Knudsen number
L_x	Length of one period
m	Mass
\dot{m}	Mass flow rate
n	Stream-wise pitch number
Nu	Nusselt number, based on hydraulic diameter
p	Fluctuating pressure component
P	Pressure
ΔP_x	Mean pressure drop in one period
Pr	Prandtl number
q	Heat flux
Q_x	Flow rate in stream-wise direction

R	Specific gas constant
Re	Reynolds number, based on hydraulic diameter
S_0	Spectral intensity
Stk	Stokes number
t	Time
Δt	Time step
T	Temperature
u	Velocity
x, y, z	Coordinate directions
\vec{Z}	Directional Gaussian white noise

Greek symbols

β	Mean stream-wise pressure gradient
γ	Mean stream-wise temperature gradient
δ	Channel half-width
δ_f	Fouling layer thickness
η	Deposition fraction
θ	Fluctuating temperature component
κ	Thermal conductivity
λ	Mean free path
μ	Absolute viscosity
ν	Kinematic viscosity
ρ	Density
τ	Wall shear stress
φ	Phase shift between top and bottom walls

Ω_S Heat transfer area

Subscripts

0 Characteristic value

$cond$ Condensation

dep Deposition

dry Dry soot

D_H Based on hydraulic diameter

eq Equivalent

f Fouling layer

g Exhaust gas

i, j Index notation

in Inlet

m Mean quantity

out Outlet

p Particle, particulate matter

sat Saturation

ref Reference value

rem Removal

w Wall

wet Wet soot

δ Based on channel half-width

τ Based on friction velocity

Superscripts

$*$ Dimensional quantity

→ Vector quantity

+ Wall units

Acronyms

CFD Computational fluid dynamics

DNS Direct numerical simulation

EGR Exhaust Gas Recirculator

GenIDLEST Generalized Incompressible Direct and Large Eddy Simulation of Turbulence

NO_x Oxides of nitrogen

RANS Reynolds-averaged Navier Stokes

RMS Root mean square

Chapter 1

Introduction

Enormous advancements have been made in automobile technology over the past century and in current times, the dependence on automobiles as a means of transportation makes them indispensable. There is an ever increasing need for more speed, higher efficiency, better technology and more. With this growth in the demand for better technology, there is also a need to take into account the environmental impact. One of the primary concerns in this regard is the emission of harmful exhaust gases resulting in environment pollution and health hazards. Automobile exhaust from both gasoline and diesel engines consists usually of a variety of components including fine carbonaceous particulate matter, oxides of nitrogen (NO_x) and volatile unburnt hydrocarbons. Various control strategies are currently employed to reduce the emission of these by-products from the automobile engines. This work is related to the exhaust gas recirculation, an effective way of reducing the NO_x emissions from internal combustion engines. In exhaust gas recirculation, a portion of the exhaust gases is circulated through the Exhaust Gas Recirculator (EGR) cooler and the cooled exhaust is reintroduced as part of the intake manifold. The presence of cooled inert gases in the intake manifold reduces the amount of oxygen available for combustion, thereby lessening the flame temperature and as a result, reducing the amount of NO_x produced. In addition, the waste heat extracted from the EGR cooler can be used as a heat source for other processes such as absorption chillers. The EGR technology has been applied successfully to high-speed diesel and gasoline engines.

One of the problems encountered in the use of EGRs is the fouling of heat exchanger surfaces from the constituents of the exhaust gas. Exhaust gases consist mostly of carbonaceous soot particles and condensable hydrocarbons from the combustion process. Transport of soot particles, usually of sub-micron size, to fin surfaces from the mainstream is one of the driving mechanisms for fouling. This is commonly known as dry soot fouling. On the other hand, the unburnt heavy hydrocarbons also condense

onto the EGR surfaces forming a fouling layer, known as wet soot fouling. The fouling in EGRs is a combination of dry and wet soot fouling and presently, the correct physics involved is not clearly understood. With the critical role that the technology of exhaust gas recirculation plays, there is a need to better understand the fouling process in EGRs. The motivation for this work stems from this lack of understanding of the fouling process in EGRs. This work, by way of CFD simulations, seeks to study the spatial and temporal nature of the fouling layer growth, which can lead to improved EGR designs and control strategies, with a focus on the heavy-duty diesel EGR coolers.

As mentioned earlier, the fouling process is a result of mainly two processes – deposition of soot particles and condensation of heavy hydrocarbons, both constituents of the exhaust emissions. The composition of the diesel exhaust is hence of interest to the present study. Kittelson [1] and Morawska et al. [2] have presented detailed studies of engine exhaust and its composition, indicating that the particulate matter in diesel exhaust ranges in size from about 10 nm, all the way to a few microns. Particulates less than 100 nm are found to be mostly new condensates in the nucleate state and constitute most of the particles in terms of numbers, whereas larger particles are fewer and more mature, but carry most of the particulate mass. In the present work, we mainly concentrate on particle sizes ranging from 10 to 100 nm. Experimental studies on deposition of soot particles have been undertaken by Messerer et al. [3] and Lee et al. [4] among others. These studies, conducted with conditions that exist in typical exhaust pipes, observed that thermophoresis is the most dominant deposition mechanism. The importance of thermophoresis is due to two main reasons – the sub-micron size of the soot particles, for which most of the other particle forces become negligible and the presence of very high temperature gradients that exist in these conditions.

The effects of thermophoresis on particle deposition have been studied by many researchers in the past. Theoretical models for thermophoresis were developed by several authors including Brock [5], Talbot et al. [6] and Batchelor and Shen [7]. These studies concentrated on particles in the continuum

regime, which have a Knudsen number $\text{Kn} \ll 1$. It should be noted that the nano-particles, to be considered in this study, have a Knudsen number in the range of 1-20. However, the formula developed by Talbot et al. [6] showed a reasonable fit for all Knudsen numbers. Zheng [8] presented a detailed review of the theoretical and experimental studies on thermophoresis conducted thus far. More recently, Guha [9] has presented a comprehensive review of various particle deposition techniques in turbulent and laminar flows.

Numerous experimental studies have been carried out on the effect of thermophoresis on particles. Stratmann and Fissan [10] studied thermophoretic deposition of aerosol particles in a laminar tube flow. Several other works were reported on laminar tube flows including the studies by Montassier et al. [11], Munoz-Bueno et al. [12] among others. The work by Munoz-Bueno et al. [12] on aerosol deposition is particularly notable for the high temperature gradients, of the order of 10^4 K/m , that were used in the experiments. The particle size considered was 20-200 nm and hence this work is very relevant to the present study. It was shown that the deposition process is independent of the particle size, when such high temperature gradients exist. Tsai and Lu [13] studied the deposition efficiencies of plate-to-plate thermal precipitators and experimentally validated the model proposed by Talbot et al. [6] for lower range of Knudsen numbers (0.27-3.5). It is noted that all the works mentioned thus far, are in the laminar regime. Flows that exist in EGR coolers are typically in the transitional or fully turbulent regimes. Comparatively fewer studies have been undertaken on thermophoresis in turbulent flows. Romay et al. [14] presented a theoretical and experimental analysis of thermophoretic deposition of particles in turbulent flow through cylindrical pipes. Tsai et al. [15] experimentally calculated the deposition efficiencies in laminar and turbulent flows and showed that theories proposed by Talbot et al. [6] and Romay et al. [14] predict the deposition efficiency accurately when only the thermophoretic deposition efficiency was considered.

Particle transport and deposition has also been studied computationally by several authors. In particular, particle deposition in turbulent channel flows has been studied in considerable detail and a few notable ones are discussed here. Li and Ahmadi [16] studied particle transport due to lift, drag and Brownian forces in a turbulent channel flow. He and Ahmadi [17] performed numerical simulations of particle deposition with Brownian, lift, thermophoresis and gravity forces. In the context of EGR fouling, a very relevant study on the fouling of heat exchanger surfaces was conducted by Brahim et al. [18], presenting a methodology to predict the growth of fouling layer. Turbulence in the aforementioned works was modeled using RANS models available in commercial CFD codes. Thakurta et al. [19] have studied particle deposition (0.05-1.66 μm) under effect of thermophoresis using direct numerical simulation techniques.

The subjects of hydrocarbon condensation onto the EGR cooler surfaces in particular and the fouling of EGRs in general are receiving considerable attention in the recent past. Ristimaki et al. [20] studied the hydrocarbon condensation in diesel exhaust. The composition of the heavy hydrocarbon chains in the exhaust and their chemical properties such as the saturation pressure and temperatures is of interest to this study. Stull [21] has presented a collection of this data for a variety of hydrocarbons from numerous experiments conducted by various researchers. Campanella [22] suggested a method to obtain a mathematical relationship between the saturation pressure and temperature. Apart from this, the process of exhaust gas recirculation and the fouling in EGRs are being studied by many. A comprehensive review of the various strategies employed in exhaust gas recirculation is described by Zheng et al. [23]. Sluder et al. [24] studied experimentally, the composition of hydrocarbons produced by the use of different types of EGR coolers. Recently, Teng [25] studied the nature of the fouling layer deposit on EGR cooler walls and classified the fouling layer into three distinct layers, each having different physical properties.

In the calculations performed in this work, two geometries – plain turbulent channel and wavy fin EGR cooler geometries are considered. Accurate simulation of the flow fields is an equally important

task. The flow field in a turbulent plain channel has been studied thoroughly by various researchers in the past. The work by Kim et al. [26] performed using direct numerical simulation presented a comprehensive account of the flow features in a plain channel. The wavy fin geometry, comprising of a channel with sinusoidal top and bottom walls, has also been a topic of considerable interest due to its effectiveness as a compact heat exchanger design. Several different designs exist in wavy channels, corresponding to different phase shift angles (ϕ) between the top and bottom walls. Much of the literature is dedicated to the converging-diverging channels ($\phi = 180^\circ$), notable among which are the works by Wang and Vanka [27], Niceno and Nobile [28] among others. The geometry of interest in this work, with in-phase top and bottom walls ($\phi = 0^\circ$) has received comparatively lesser attention, with a few detailed experimental and numerical studies existing in literature. Nishimura et al. [29] presented detailed experimental results of the flow features existing in wavy channel flows. On the other hand, Snyder et al. [30] presented a detailed study of the flow features in a serpentine channel. Their work analyzes the distribution of the local Nusselt number and wall shear stress along the channel, once the flow is fully developed. Rush et al. [31] analyzed various wavy channel configurations experimentally, to study the dependence of the flow and heat transfer characteristics on the geometric parameters. Recently, Oviedo-Tolentino et al. [32] and Pham et al. [33] presented results on developing wavy channel flows, discussing the onset of turbulence for various geometric configurations.

Although a vast amount of literature exists, it is noted that deposition studies have not been carried out for turbulent flows with high temperature gradients, of the order of 10^6 K/m, which exist in EGR coolers. This apart, no studies on particle deposition in wavy channels is available in the literature. It is the objective of this work to present some insight into the process of fouling – occurring due to the deposition of soot particles and condensation of hydrocarbons onto the EGR cooler surfaces. The study of deposition of sub-micron (10-100 nm) particles in typical operating conditions, along with the study of condensation of heavy hydrocarbons, would assist in understanding the nature of fouling in EGRs. Also,

the effects of particle sizes are difficult to study using experiments and hence in this regard, CFD provides a good option to isolate the effects due to the individual particle sizes. The computations are performed in plain channel and wavy channel geometries with flow conditions and particle properties chosen such that they closely resemble typical EGR flows. This work, hence lays a foundation for characterizing the process of fouling and identifying the correct physics behind it.

This dissertation presents the details of the work undertaken as an effort to understand the fouling process in EGRs better and address the related issues. In this regard, a systematic study has been carried out by way of several numerical simulations, the details of which are presented in this dissertation. The mathematical equations and numerical methodology used are presented in Chapter 2. The results obtained from the various computations are described in the subsequent four chapters. In Chapter 3, soot deposition calculations performed in a turbulent plain channel are presented. This helps in the understanding of the basic particle physics in EGR flows. This is followed by studies performed on a wavy channel geometry, which is a more accurate representation of an EGR cooler. The process of soot deposition in a fully-developed flow is considered in Chapter 4, followed by discussion on the results obtained in a developing flow framework in Chapter 5. Finally, the topic of hydrocarbon condensation and its combined effect on the process of fouling is studied, which constitutes the matter of discussion in Chapter 6.

Chapter 2

Numerical methodology

In this chapter, the detailed numerical methodology used for the carrier and discrete phases in the computations is presented. Calculations are performed using an in-house code Generalized Incompressible Direct and Large Eddy Simulation of Turbulence (GenIDLEST). The details of the framework and methodology used can be found in Tafti [34]. GenIDLEST has been applied to a wide spectrum of applications in the past including dispersed phase modeling of particulate matter, which has been validated and applied to investigations of deposition and erosion of turbine components by Shah and Tafti [35] and Rozati and Tafti [36].

2.1 Carrier phase

2.1.1 Governing equations

The governing Navier-Stokes equations for incompressible fluids in non-dimensional form are as follows:

Mass conservation

$$\frac{\partial u_i}{\partial x_i} = 0 \quad \text{2.1}$$

Momentum conservation

$$\frac{\partial u_i}{\partial t} + \frac{\partial(u_j u_i)}{\partial x_j} = -\frac{\partial P}{\partial x_i} + \frac{\partial}{\partial x_j} \left(\frac{1}{Re} \frac{\partial u_i}{\partial x_j} \right) \quad \text{2.2}$$

Energy conservation

$$\frac{\partial T}{\partial t} + \frac{\partial(u_j T)}{\partial x_j} = \frac{\partial}{\partial x_j} \left(\frac{1}{RePr} \frac{\partial T}{\partial x_j} \right) \quad \text{2.3}$$

2.1.2 Governing equations in generalized coordinates

In all the computations, the above mentioned governing equations are transformed to generalized coordinates. For spatial discretization of the transformed equations, a conservative finite-volume formulation with a non-staggered grid topology is used. The cartesian velocities, pressure and temperature values are calculated and stored at the cell center, whereas contravariant volume fluxes are calculated and stored at the cell faces. A projection method is used for time integration of the continuity and momentum equations. The temporal advancement uses second order accurate predictor-corrector steps; the predictor step calculates an intermediate velocity field and the corrector step calculates the updated divergence free velocity at the new time-step.

2.1.3 Fully-developed periodic flow

A fully-developed flow assumption means that the velocity and temperature gradients do not change between the periodically repeating units of the flow in the stream-wise direction. In very long channels or fins, this approximation is consistent with the behavior of the hydrodynamic field encountered. However, it is not consistent with the temperature and pressure fields which are constantly evolving in a long channel. Hence, for the constant heat flux boundary condition used in the calculations, the temperature field is modified to make it behave as if it is fully-developed. Similarly, for the pressure field a constant pressure gradient is maintained along the stream-wise direction and the total pressure is appropriately modified to behave as fully developed by solving for the fluctuating pressure above the mean. The formulation was developed by Patankar et al. [37] and has been implemented by Zhang et al. [38] among others for several periodic geometries. The procedure is outlined here briefly. The detailed description of the procedure used can be found in Patankar et al. [37] and Zhang et al. [38].

Velocity in the Navier-Stokes equations is non-dimensionalized with friction velocity $u_\tau^* = \sqrt{\tau_{w_{eq}}^*/\rho^*}$. By applying conservation of momentum across the periodic domain, the reference velocity is hence written as:

$$u_{ref}^* = u_\tau^* = \sqrt{\frac{\tau_{w_{eq}}^*}{\rho^*}} = \sqrt{\left(-\frac{\Delta P_x^*}{L_x^*}\right)\left(\frac{D_H^*}{4\rho^*}\right)} \quad 2.4$$

where $\tau_{w_{eq}}^*$ is the equivalent wall shear stress which includes form losses in the domain, ΔP_x^* is the mean pressure drop in the stream-wise direction across a periodic length L_x^* and D_H^* is the hydraulic diameter. The temperature is non-dimensionalized with the characteristic temperature $T_0^* = q_w^* \delta^* / \kappa^*$, where $-q_w^*$ is the applied wall heat flux and δ^* is the characteristic length scale. Unlike the velocity field in a periodic domain, the temperature and pressure distributions vary continuously along the stream-wise direction and hence these two quantities are expressed in terms of the mean stream-wise gradient and a separate fluctuating component as follows:

$$P^*(\vec{x}, t) = P_{ref}^* - \beta^* \cdot x^* + p^*(\vec{x}, t) \quad 2.5$$

$$T^*(\vec{x}, t) = T_{ref}^* + \gamma^* \cdot x^* + \theta^*(\vec{x}, t) \quad 2.6$$

where, $\beta^* = -\Delta P_x^*/L_x^*$ is the stream-wise pressure gradient, p^* is the pressure fluctuation, γ^* is the stream-wise temperature gradient and θ^* is the fluctuating temperature component. Non-dimensionalization of eqns. 2.5 and 2.6 gives:

$$P(\vec{x}, t) = -\beta \cdot x + p(\vec{x}, t) \quad 2.7$$

$$T(\vec{x}, t) = \gamma \cdot x + \theta(\vec{x}, t) \quad 2.8$$

where, $\beta = 4 / D_H$ and $\gamma = \Omega_S / (Re \cdot Pr \cdot Q_x \cdot L_x)$. While the continuity equation remains unchanged due to this assumption, the momentum and the energy equation take the following form when non-dimensionalized:

Momentum conservation

$$\frac{\partial u_i}{\partial t} + \frac{\partial(u_j u_i)}{\partial x_j} = -\frac{\partial p}{\partial x_i} + \frac{\partial}{\partial x_j} \left(\frac{1}{Re} \frac{\partial u_i}{\partial x_j} \right) + \beta \vec{e}_x \quad 2.9$$

Energy conservation

$$\frac{\partial \theta}{\partial t} + \frac{\partial(u_j \theta)}{\partial x_j} = \frac{\partial}{\partial x_j} \left(\frac{1}{Pr Re} \frac{\partial \theta}{\partial x_j} \right) - \gamma u_x \quad 2.10$$

2.2 Discrete phase

The equations of motion for the discrete phase are solved in the Lagrangian framework. The particle equation of motion is a basic application of Newton's second law and is expressed as follows:

$$m_p^* \frac{d\vec{u}_p^*}{dt^*} = \sum \vec{F}_p^*; \quad \frac{d\vec{x}_p^*}{dt^*} = \vec{u}_p^* \quad 2.11$$

where m_p^* and \vec{u}_p^* are the mass and velocity of the particle respectively.

The following assumptions are made in implementing the dispersed phase model:

1. Particles are rigid and spherical in shape.
2. The discrete phase is very dilute and hence inter-particle interactions are neglected.
3. Particles exhibit only one-way coupling, i.e., particles are affected by the fluid motion but not vice versa.

2.2.1 Particle forces

The various forces acting on a particle are accounted for in the summation on the right hand side of the above equation. The individual forces are described briefly in the following section. The detailed explanation for different forces can be found in Rudinger [39]. The non-dimensional expanded form of the above equation is:

$$\begin{aligned} \frac{d\vec{u}_p}{dt} = & \vec{F}_{drag} + \vec{F}_{buoyancy} + \vec{F}_{added\ mass} + \vec{F}_{pressure} + \vec{F}_{basset} + \vec{F}_{lift} + \vec{F}_{brownian} \\ & + \vec{F}_{thermophoresis} \end{aligned} \quad 2.12$$

Drag force on a particle is exerted due to relative velocity between fluid and the particle and acts in a direction opposing the relative flow. Buoyancy force is exerted on the particle due to the volume of fluid displaced by the particle and becomes important when the density ratio approaches unity. Added mass is the force needed to accelerate the fluid surrounding the particle during particle acceleration. The pressure force term accounts for forces acting on the particle due to spatial gradients in pressure and viscous stresses. The Basset or history force accounts for the relative acceleration of the particle. Lift force is caused by the shear of the surrounding fluid which results in a non-uniform pressure distribution around the particle inducing lift. Brownian and thermophoretic forces are important in the study of sub-micron particles, and are a result of random molecular motion and forces induced due to temperature gradients, respectively. The formulations used for each of these forces are provided in Appendix A.

2.2.2 Particle deposition model

In our calculations, the deposition model is simplified to assume that any collision with a surface results in the particle depositing on that surface irrespective of the state of the particle. This assumption would simulate the worst case scenario as far as particle deposition is concerned.

2.2.3 Dispersed phase in periodic geometries

Particle trajectories are computed in the simulations, both in the developing flow and periodic fully developed calculations. In developing flow calculations, the trajectory calculations are direct, since the particle proceeds continuously through the domain. However, when the flow is periodic in nature, particles may cross a periodic boundary (stream-wise or span-wise). When a particle moves out of the domain through a periodic boundary, it is reintroduced in the computational domain at the same location on its corresponding periodic face. Since the location of deposition in the stream-wise direction is of primary interest, the number of such traverses made through the periodic boundary in the stream-wise direction is tracked. The location of deposition in the periodic geometry along with the number of

traverses for the particle is used to compute the actual location of deposition along the simulated length of the channel.

Chapter 3

Soot particle deposition in a turbulent plain channel¹

3.1 Introduction

One of the simplest and most effective methods of reducing nitrogen oxide (NO_x) emissions in internal combustion engines is to cool the exhaust gases from the engine in an Exhaust Gas Recirculator (EGR) and recirculate the gases into the intake air manifold. The introduction of the cooled inert exhaust gases results in a lower combustion peak temperature which reduces the formation of NO_x . In addition, the waste heat extracted from the EGR can be used as a heat source for other processes such as absorption chillers. The EGR technology has been applied successfully to high-speed diesel and gasoline engines. One of the problems encountered in the use of EGRs is fouling of the heat exchanger surfaces from diesel exhaust gas particulates. Transport of soot particles, usually of sub-micron size, to fin surfaces from the mainstream is one of the driving mechanisms for fouling. The particulate matter consists mostly of soot from the combustion process and condensable hydrocarbons as the exhaust cools at heat exchanger surfaces without dilution. Presently, the physical nature of fouling in EGRs is not clearly understood, although thermophoresis is thought to play a major role.

The effects of thermophoresis on particle deposition have been studied by many researchers in the past. Theoretical models of thermophoresis were developed by several authors including Brock [5], Talbot et al. [6] and Batchelor and Shen [7]. Stratmann and Fissan [10] studied thermophoretic deposition of aerosol particles in a laminar tube flow. Tsai and Lu [13] studied deposition efficiencies of plate-to-plate thermal precipitators and experimentally validated the model proposed by Talbot et al. [6] for lower range of Knudsen numbers (0.27-3.5). Munoz-Bueno et al. [12] conducted experiments of aerosol deposition in laminar flows with high temperature gradients. It was shown that deposition process is

¹ Paper presented – N. Krishnamurthy, Danesh K. Tafti and Aroon K. Viswanathan, “Modeling of Gas-Side Fouling in Exhaust Gas Recirculators – Turbulent Channel Flow”, Seventh International Conference on Enhanced, Compact and Ultra-Compact Heat Exchangers: From Microscale Phenomena to Industrial Applications, Sep. 2009.

independent of particle size, when high temperature gradients exist. Few studies have also been undertaken on thermophoresis in turbulent flows. Romay et al. [14] presented a theoretical and experimental analysis of thermophoretic deposition of particles in turbulent flow through cylindrical pipes. Tsai et al. [15] experimentally calculated the deposition efficiencies in laminar and turbulent flows and showed that theories proposed by Talbot et al. [6] and Romay et al. [14] predict the deposition efficiency accurately when only thermophoretic deposition efficiency was considered. Recently, Guha [9] has presented a comprehensive review of various particle deposition techniques in turbulent and laminar flows.

Particle transport and deposition has also been studied computationally by several authors. Li and Ahmadi [16] studied particle transport due to lift, drag and Brownian forces in turbulent channel flow. He and Ahmadi [17] performed numerical simulations of particle deposition with Brownian, lift, thermophoresis and gravity forces. Turbulence in the aforementioned works was modeled using RANS models available in a commercial CFD code. Fouling of heat exchanger surfaces was also studied recently by Brahim et al. [18] using a k- ϵ model for turbulence simulation. Thakurta et al. [19] have studied particle deposition (0.05-1.66 μm) under effect of thermophoresis using direct numerical simulation techniques.

Most of these studies (both computational and experimental) have concentrated mainly on particles of diameter larger than 0.1 μm . However, studies by Kittelson [1] and Morawska et al. [2] indicate that particulate matter in diesel exhaust ranges in size from about 10 nm, all the way to a few microns. Particulates less than 100 nm are mostly new condensates in the nucleate state and constitute most of the particles, whereas larger particles are fewer and more mature but carry most of the particulate mass. In this work, we mainly concentrate on particle sizes ranging from 10 to 100 nm. Studies on deposition in exhaust pipes have been undertaken by Tippayawong [40], Messerer et al. [3] and Lee et al. [4] among others.

However, thermophoresis and its effects on deposition have not been studied for turbulent flows with high temperature gradients, which exist in an EGR. The study of deposition of sub-micron (10-100 nm) particles in typical operating conditions would give insight into the nature of fouling in EGRs. Also, the effects of particle sizes are difficult to study using experiments and CFD provides a good option to isolate the effects due to the individual particle sizes. The computations are performed in a representative channel geometry with flow conditions and particle properties chosen such that they closely resemble the EGR flow. The turbulence in the flow is accounted for by solving the complete Navier-Stokes equations on a sufficiently fine mesh at the given Reynolds number. The effect of turbulent flow is investigated together with particles of different sizes and different force characterizations. This chapter hence lays a foundation for characterizing the process of fouling and identifying the correct physics behind it.

3.2 Methodology²

Calculations are performed using an in-house code Generalized Incompressible Direct and Large Eddy Simulation of Turbulence (GenIDLEST). GenIDLEST has been applied to a wide spectrum of applications including dispersed phase modeling of particulate matter, which has been validated and applied to investigations of deposition and erosion in turbine components (Tafti [34], Shah and Tafti [35] and Rozati and Tafti [36]).

3.2.1 Carrier phase

Fluid flow field computations are carried out by solving the non-dimensional form of the Navier-Stokes equations. A fully-developed flow assumption is used in all the calculations. This assumption means that the velocity and temperature gradients do not change between the periodically repeating units of the flow in the stream-wise direction. In very long channels or fins (total length \gg development length) this approximation is consistent with the behavior of the hydrodynamics encountered. However, it is not

² Details provided in Chapter 2

consistent with the temperature and pressure fields which are constantly evolving in a long channel. Hence, for the constant heat flux condition used in the calculations, the temperature field is modified to make it behave as if it is fully-developed (Patankar et al. [37] and Zhang et al. [38]). Similarly, for the pressure field a constant pressure gradient is maintained along the stream-wise direction and the total pressure is appropriately modified to behave as fully developed by solving for the fluctuating pressure above the mean.

Velocity and temperature in the Navier-Stokes equations are non-dimensionalized with friction velocity u_τ^* , characteristic temperature T_0^* respectively. The channel half-width δ^* is used as the characteristic length scale and correspondingly time is non-dimensionalized with δ^*/u_τ^* . The wall friction velocity is defined as $u_\tau^* = (\tau_{w_{eq}}^*/\rho^*)^{1/2}$, where $\tau_{w_{eq}}^*$ is an equivalent mean wall shear which also includes form losses in the domain, if present, and the characteristic temperature is defined as $T_0^* = (q_w^* \cdot \delta^*/\kappa^*)$, where $-q_w^*$ is the applied wall heat flux. To obtain different temperature gradients, the wall temperature is varied keeping the gas temperature fixed. Based on temperatures T_w^* and T_g^* obtained from the physical flow of interest and the Nusselt number obtained from the calculations, the near-wall temperature gradient is calculated as:

$$\left. \frac{dT^*}{dy^*} \right|_{wall} = - \frac{Nu_\delta}{\delta^*} \cdot (T_w^* - T_g^*) \quad 3.1$$

3.2.2 Dispersed phase

The particle calculations are done by following individual particle trajectories in a Lagrangian framework. It is assumed that particles are spherical in shape, do not interact with each other and only exhibit one-way coupling (fluid affects particle motion but not vice versa). The non-dimensional equation for the forces acting on a particle per unit mass (or particle acceleration) can then be written as:

$$\frac{d\vec{u}_p}{dt} = \vec{F}_{drag} + \vec{F}_{buoyancy} + \vec{F}_{added\ mass} + \vec{F}_{pressure} + \vec{F}_{basset} + \vec{F}_{lift} + \vec{F}_{brownian} \\ + \vec{F}_{thermophoresis} \quad 3.2$$

Drag force is exerted due to relative velocity between fluid and the particle and acts in a direction opposing the relative flow. Added mass is the force needed to accelerate the fluid surrounding the particle during particle acceleration. The pressure force term accounts for forces acting on the particle due to spatial gradients in pressure and viscous stresses. The Basset or history force accounts for the relative acceleration of the particle. Lift force is caused by the shear of the surrounding fluid which results in a non-uniform pressure distribution around the particle inducing lift. Brownian and thermophoretic forces are important in the study of sub-micron particles, and are a result of random molecular motion and forces induced due to temperature gradients, respectively.

In particle trajectory calculations, the periodic nature of the flow is taken into account by inserting a particle that crosses a periodic boundary back into the computational domain at its corresponding periodic boundary location. In the stream-wise direction, the number of such traverses for each particle is then used to compute the actual location of deposition along the flow direction.

3.3 Results and discussion

3.3.1 Turbulent channel flow

Calculations are carried out in turbulent channel flow at a Reynolds number $Re_\tau = 180$ based on channel half-width δ^* and wall friction velocity u_τ^* . A grid of $64 \times 64 \times 64$ computational cells was used in the x-, y-, and z- directions, respectively. The grid spacing used in wall coordinates was $\Delta x^+ = 17.67$, $\Delta z^+ = 8.84$ in the homogeneous wall parallel directions, with the first grid point in the inhomogeneous y-direction placed at $y_1^+ = 0.9$ with 5 grid points within $y^+ < 6$. The maximum spacing at the center of the channel was $\Delta y^+ = 11.56$. The non-dimensional time step used was 1×10^{-3} .

After specifying a fixed mean pressure gradient in the flow direction and a constant heat flux boundary condition at the channel walls, the calculation was initialized with a perturbed mean turbulent channel flow profile, which was allowed to evolve in time till the solution reached a stationary state. The mean velocity or the flow rate in the channel results from a balance between friction at the walls and the specified mean pressure gradient.

Figure 3-1 shows the root mean square (RMS) fluctuations of the three-velocity components and turbulent shear stress normalized by the friction velocity. The results are compared to the direct numerical simulation (DNS) data of Kim et al. [26] (KMM) and the agreement is found to be very good.

Table 3.1 summarizes the major results comparing them to data from earlier DNS results and to correlations in the literature and it is seen that all the predictions agree very well.

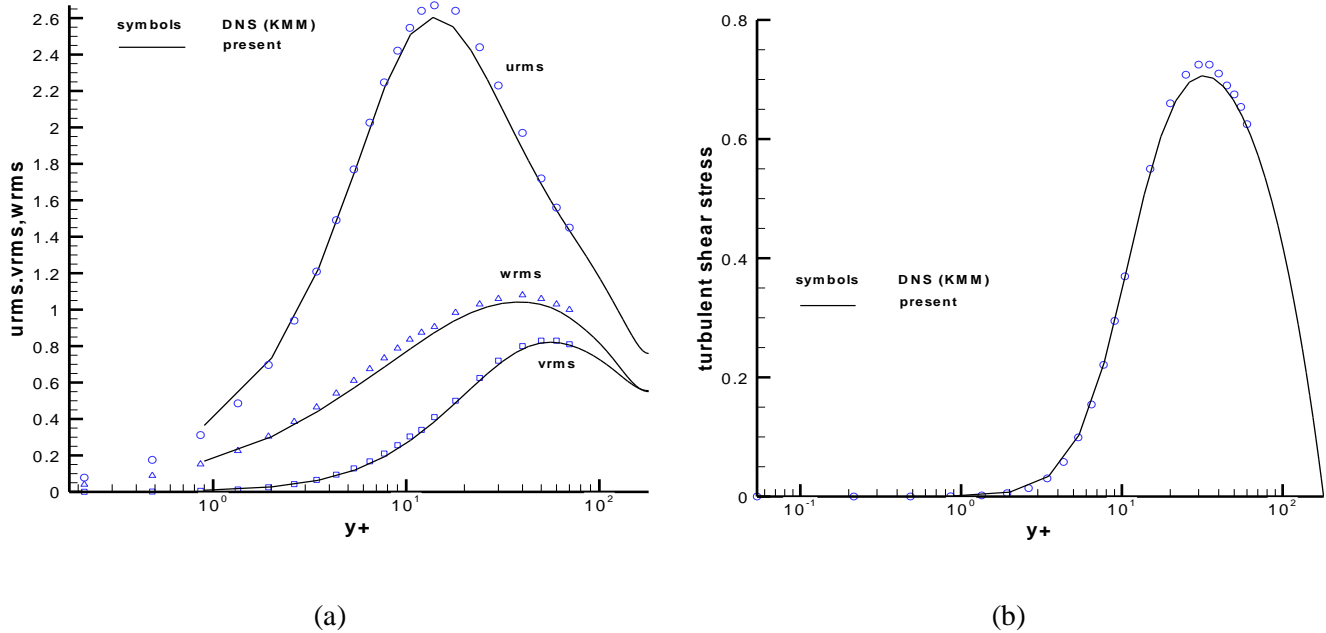


Figure 3-1 (a) RMS Fluctuations of normal turbulent stresses; (b) turbulent shear stress

Table 3.1 Comparison of turbulent channel flow results with DNS and Correlations

	Present	Kim et al. [26]	Correlations (Incropera [41])
$Re_\tau = u_\tau^* \cdot \delta^* / \nu^*$	180	180	
$Re_{D_H} = u_m^* \cdot D_H^* / \nu^*$	11200	11200	
$C_f = \tau_w^* / (1/2) \cdot \rho^* \cdot u_m^{*2}$	8.21×10^{-3}	8.18×10^{-3}	Petukhov: 8.45×10^{-3}
$Nu_{D_H} = h^* \cdot \delta^* / \kappa^*$	36.8	-	Dittus-Boelter: 35.86

3.3.2 Relative effect of different particle forces

Order of magnitude analysis

An order of magnitude analysis is performed on the relative contribution of forces in a turbulent channel flow. The Reynolds number, based on hydraulic diameter Re_{D_H} , in a typical EGR flow varies from 8000-20000, which is in the fully turbulent flow regime. Based on flow and particle properties used for the calculations, the relative magnitude of forces is computed and provided in Table 3.2.

To confirm and validate the order of magnitude analysis and to investigate the relative effects of different particle transport mechanisms in EGR flow conditions, particle forces are evaluated for 10 nm and 100 nm particles in a turbulent channel flow at Re_{D_H} of 11200. The wall is maintained at 150 °C and inlet gas temperature is 600 °C. Figure 3-1 shows the non-dimensional magnitudes of y-direction forces computed. The magnitudes of drag and thermophoretic forces are clearly noted to be of higher magnitudes. The following observations are made regarding particle forces:

1. Between drag and lift forces, lift force is at least 1-2 orders of magnitude smaller.
2. Buoyancy, added mass, pressure and Basset forces can be neglected.

3. Only forces of relative importance for particle size range 10-100 nm are drag, Brownian and thermophoretic forces.

Table 3.2 Comparison of orders of magnitude of different particle forces in representative conditions ($Re_{D_H} = 11200$, $T_w^* = 150^\circ C$, $T_g^* = 600^\circ C$)

d_p^* (nm)	F_{drag}	F_{buoy}	F_{added}	F_{press}	F_{bass}	F_{lift}	F_{brown}	F_{therm}
1	10^3	10^{-4}	$< 10^{-4}$	$< 10^{-4}$	$< 10^{-2}$	10^1	10^6	10^3
10	10^2	10^{-4}	$< 10^{-4}$	$< 10^{-4}$	$< 10^{-2}$	10^0	10^4	10^2
100	10^1	10^{-4}	$< 10^{-4}$	$< 10^{-4}$	$< 10^{-1}$	10^{-1}	10^1	10^1
1000	10^{-1}	10^{-4}	$< 10^{-4}$	$< 10^{-4}$	$< 10^{-3}$	10^{-2}	10^{-2}	10^{-1}

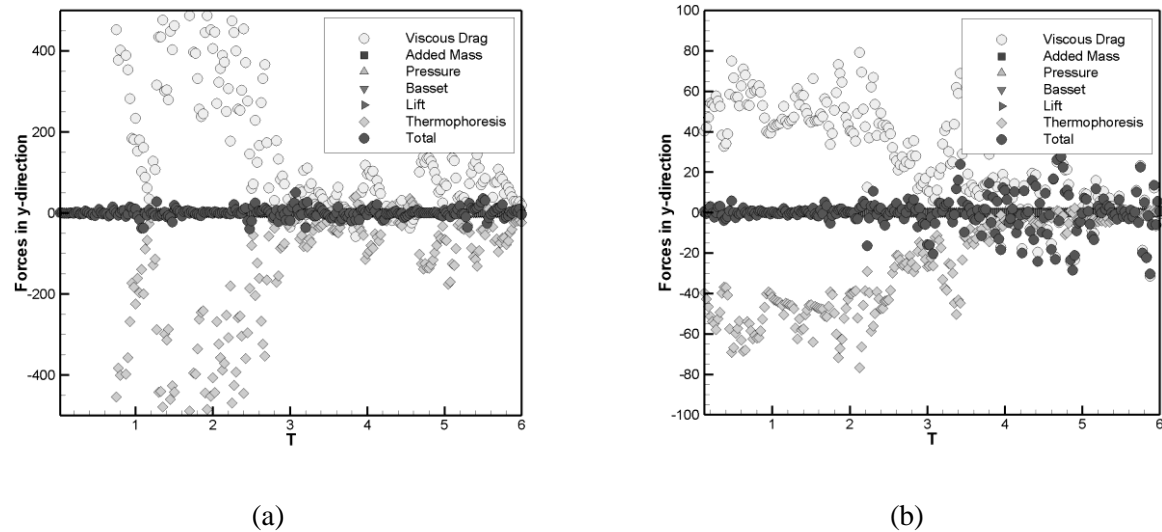


Figure 3-2 Non-dimensional force magnitudes on particles of size (a) 10 nm and (b) 100 nm particles ($Re_{D_H} = 11200$, $T_w^* = 150^\circ C$, $T_g^* = 600^\circ C$)

Relative effect of drag, Brownian and thermophoretic forces

Further, to investigate the effect of force mechanisms on the deposition process, calculations for two cases are performed – (i) without thermophoresis and (ii) without Brownian motion. The flow and

particle properties considered are the same as used for all the calculations, provided in Table 3.3. For these conditions, the drag and Brownian forces are of comparable magnitude to the thermophoretic force. As seen in the order of magnitude analysis, the Brownian force is in fact 1-2 orders higher for 10 nm particles.

Table 3.3 Particle and fluid properties used in the calculations

Particle properties (Carbon)		
Density	2267 kg/m ³	
Specific heat	710 J/kg/K	
Thermal conductivity	129 W/m/K	
Diameters	10 nm	100 nm
Particle time scale	6.8 x 10 ⁻⁹ s	9.5 x 10 ⁻⁸ s
Stokes number	2.5 x 10 ⁻⁵	3.6 x 10 ⁻⁴
Fluid properties (air)		
Absolute viscosity	3.249 x 10 ⁻⁵ Ns/m ²	
Density	1.553 kg/m ³	
Thermal conductivity	0.0502 W/m/K	
Specific heat	1070 J/kg/K	
Gas constant	287 J/kg/K	
Reynolds number (Re_{D_H})	11200 (from calculation)	
Nusselt number (Nu_{D_H})	36.8 (from calculation)	
Prandtl number	0.7	

For the calculation without thermophoresis, a final deposition percentage of less than 0.1% was observed compared to 40% deposition for the case with thermophoresis. The effect of Brownian motion

on deposition is established by the calculations which are carried out without Brownian motion for 10 and 100 nm particles. The calculations are performed for 5 non-dimensional time units. Figure 3-3 presents a comparison of runs with and without Brownian motion for 10 nm particles. The number of depositions is plotted against the number of channel half-widths traversed along the flow direction. It is seen that the depositions observed show very similar characteristics. Similar results are observed for the calculation with 100 nm particles. This study indicates that Brownian motion, which is inherently random, does not contribute much to the deposition process and establishes that thermophoresis is the dominant deposition mechanism in EGR operating conditions.

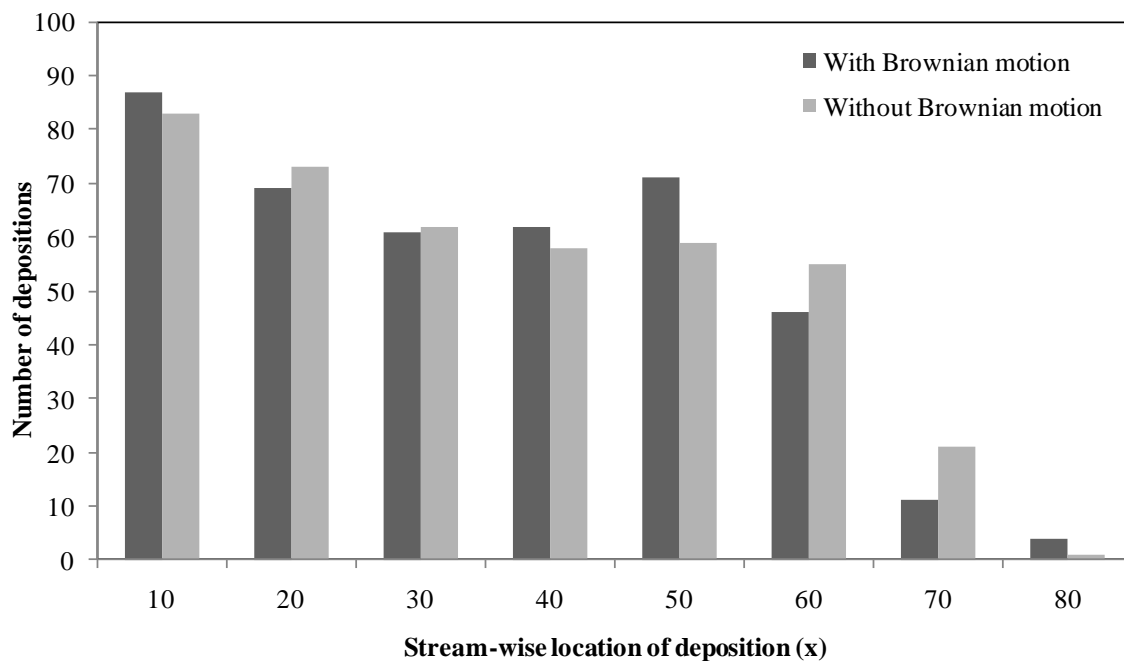


Figure 3-3 Comparison of depositions observed against stream-wise location of deposition for 10 nm particles ($Re_{D_H} = 11200$, $T_w^* = 150^\circ\text{C}$, $T_g^* = 600^\circ\text{C}$)

3.3.3 Particle deposition for typical operating conditions

A fully developed turbulent channel with periodicity along the stream-wise (x-) and lateral (z-) directions is considered. Flow and particle properties are the same as used for the relative effect of

particle forces on deposition and is given in Table 3.3. The Reynolds number (Re_{DH}) of the flow is maintained at approximately 11200. The particles are initially suspended randomly on a plane perpendicular to the flow direction.

The inlet gas temperature is 600 °C and the wall temperature is maintained at 150 °C. Using Eq. 3.1, the resulting effective near wall temperature gradient is then calculated to be 4.18×10^6 K/m, which is a typical value in most EGRs. The number of depositions is studied with respect to the location and time of deposition. Fig. 4 shows a histogram plot of percentage of depositions along the stream-wise direction for 10 and 100 nm particles. The equivalent stream-wise distance is calculated by tagging particles each time they leave the periodic computational domain and by re-introducing them into the domain, till they deposit. Deposition is expressed as a normalized percentage deposition which is defined as the ratio of number of particles deposited to the number of particles remaining in the channel.

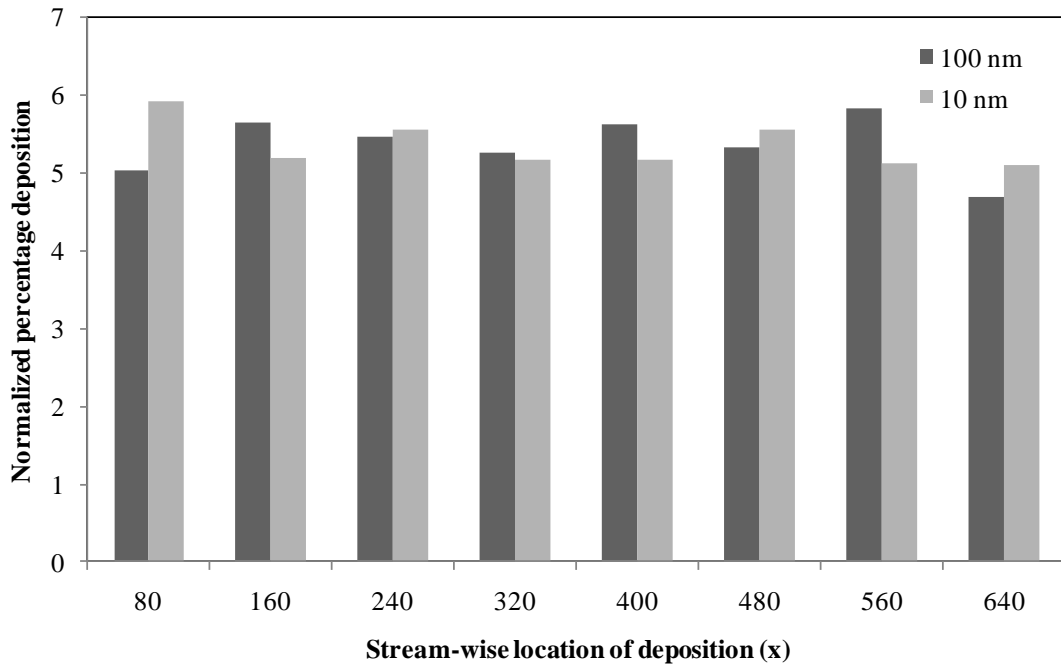


Figure 3-4 Plot of normalized percentage deposition with stream-wise location of deposition for 10 and 100 nm particles ($Re_{DH} = 11200$, $T_w^* = 150$ °C, $T_g^* = 600$ °C)

The plot clearly indicates that the deposition process for these conditions is independent of the particle size. It is seen that the number of depositions occurring in the channel is roughly uniform. For a sampling length of 80 channel half-widths, 5-6% of the particles remaining in the channel get deposited. Analysis of deposition with respect to time of deposition also shows a similar uniform trend.

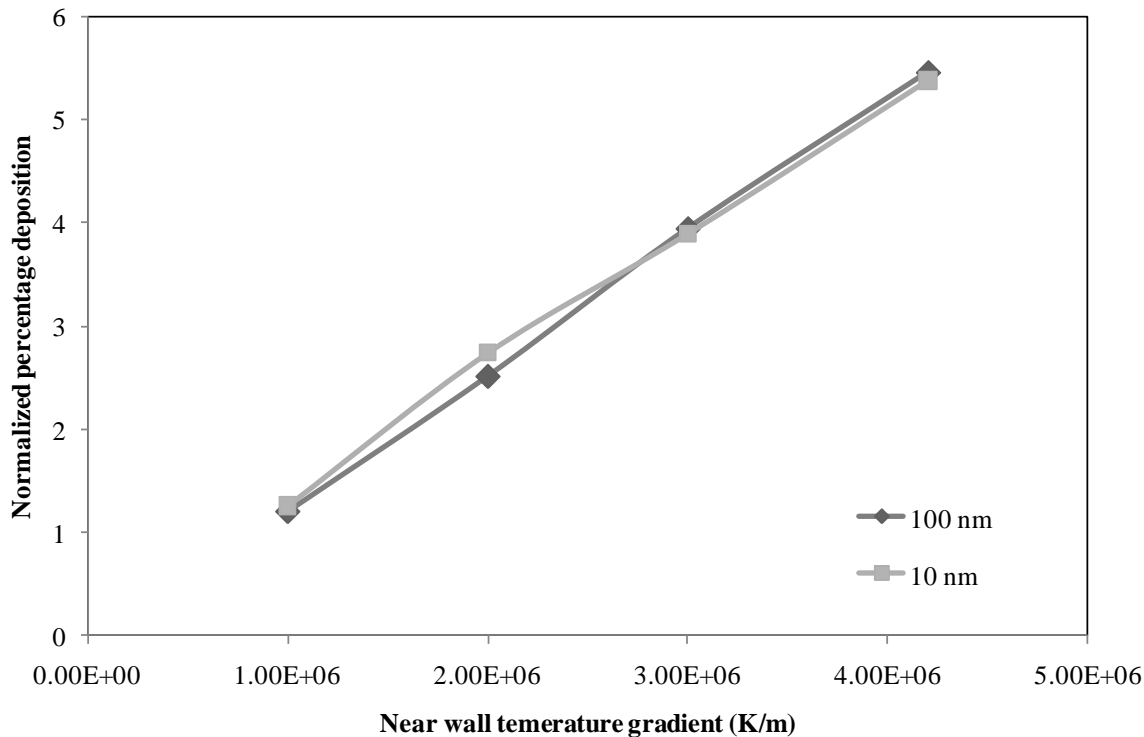


Figure 3-5 Normalized percentage deposition for every 80 length units along stream-wise direction for various temperature gradients

3.3.4 Effect of temperature gradient on particle deposition

The effect of gas-to-wall temperature difference is studied by performing calculations for different wall temperatures. The gas temperature is maintained at 600 °C. Wall temperatures used for calculations are 150 °C, 277 °C, 385 °C and 493 °C which correspond to equivalent near-wall temperature gradients of 4.2×10^6 K/m, 3×10^6 K/m, 2×10^6 K/m and 1×10^6 K/m respectively, calculated from eq. 3.1. The inlet gas temperature is taken as the reference temperature for the thermophoretic force

calculation. Figure 3-5 shows the plot of percentage of depositions observed for 80 channel half-widths along stream-wise direction for different temperature gradients. It is seen that deposition varies linearly with the gas-to-wall temperature difference. The deposition percentage is normalized with the number of particles remaining in the channel.

It should be noted that again, the 10 and 100 nm particles exhibit similar deposition trends. The effect of particle size on deposition process is in line with the experimental results of Munoz-Bueno et al. [12], who had observed similar behavior in laminar flows.

3.4 Conclusions

The process of soot deposition in a typical EGR is studied through calculations in a representative turbulent channel flow. For operating conditions in EGR flow, the particle forces of comparable magnitude are viscous drag, Brownian and thermophoretic forces. Of these, thermophoresis is found to be the major deposition mechanism, whereas drag and Brownian forces' contribution to the deposition process is negligible. Several gas-to-wall temperature differences (or temperature gradients) are considered to study the impact on the deposition process. It is observed that the percentage deposition shows a linear behavior with variation in temperature gradient. It is also noted that 10 and 100 nm particles exhibit similar deposition characteristics, thus suggesting that the deposition is independent of the particle size for the range of particle diameters (10-100 nm) considered.

Chapter 4

Soot particle deposition in a periodic wavy channel

4.1 Introduction

In this chapter, we look at a more representative wavy fin surface, which is used in EGR cooler. Wavy fins perturb the flow in the EGR cooler, to enhance mixing and heat transfer coefficients without the penalty of a large pressure drop. Calculations are performed to simulate soot particle deposition in a periodic sinusoidal channel. The effect of channel geometry, flow Reynolds number and the applied near-wall temperature gradients on the deposition process is analyzed.

4.2 Methodology

Calculations are performed using the in-house code GenIDLEST. The mathematical equations used and the particulars of pressure and temperature calculations in a periodic domain calculation are elaborately described in Section 2.1 and Section 3.2.1. The equations used for the dispersed phase and the treatment of the particle trajectories in periodic framework are provided in Section 2.2.

Alongside, it is noted that a uniform heat flux thermal boundary condition is implemented in all the calculations. This necessitates a brief description of the method employed for the computation of Nusselt number and near-wall temperature gradient which is presented here. As mentioned in Section 2.1.3, the temperature is non-dimensionalized with the characteristic temperature $T_0^* = q_w^* \delta^* / \kappa^*$, where $-q_w^*$ is the applied wall heat flux and δ^* is the characteristic length scale. In the context of wavy channel flow, δ^* is the channel half-width. The negative sign in $-q_w^*$ indicates the removal of heat at the walls and is set to a non-dimensional value of 1. The local Nusselt number is then computed as given below:

$$Nu_\delta = -\frac{1}{\bar{\theta}_w - \bar{\theta}_{ref}} \quad 4.1$$

where, $\bar{\theta}_w$ is the non-dimensional wall temperature, $\bar{\theta}_{ref}$ is the non-dimensional mean temperature in the domain and the Nusselt number is based on channel half-width δ^* . The bar in the denominator represents

an average taken over the entire domain. Again, the negative sign is added to account for the removal of heat. It should be noted that the use of Nu without a subscript means that it is the Nusselt number based on the hydraulic diameter. The value of Nusselt number thus computed is then used to compute the dimensional average near-wall temperature gradient and hence the dimensional heat flux as given below:

$$\frac{dT^*}{dy^*} \Big|_w = \frac{Nu_\delta}{\delta^*} \cdot (T_g^* - T_w^*) \quad 4.2$$

$$q_w^* = -\kappa^* \cdot \frac{dT^*}{dy^*} \Big|_w \quad 4.3$$

Eq. 4.2 and Eq. 4.3 express the relationship between the average near-wall temperature gradient, the temperature difference between the exhaust gas and the walls and the heat flux at the walls. In the discussions presented henceforth, these quantities will be used synonymously. Also, the term “average near-wall temperature gradient” will be referred to as “wall temperature gradient”.

4.3 Geometry and computational grid

The wavy channel geometry used in the calculations consists of in-phase sinusoidal top and bottom walls. All the dimensions are non-dimensionalized with the channel half-width. The non-dimensional peak-to-crest amplitude is 4.54 and the periodic length L is 9.525. In all the discussions, the peak of the sine wave is referred to as crest and the valley as trough. A computational grid of resolution $96 \times 64 \times 64$ in the x-, y- and z- directions respectively is used in all the calculations. The grid with the geometric specifications is shown in Figure 4-1. The domain is periodic in the stream-wise (x) and lateral (z) directions.

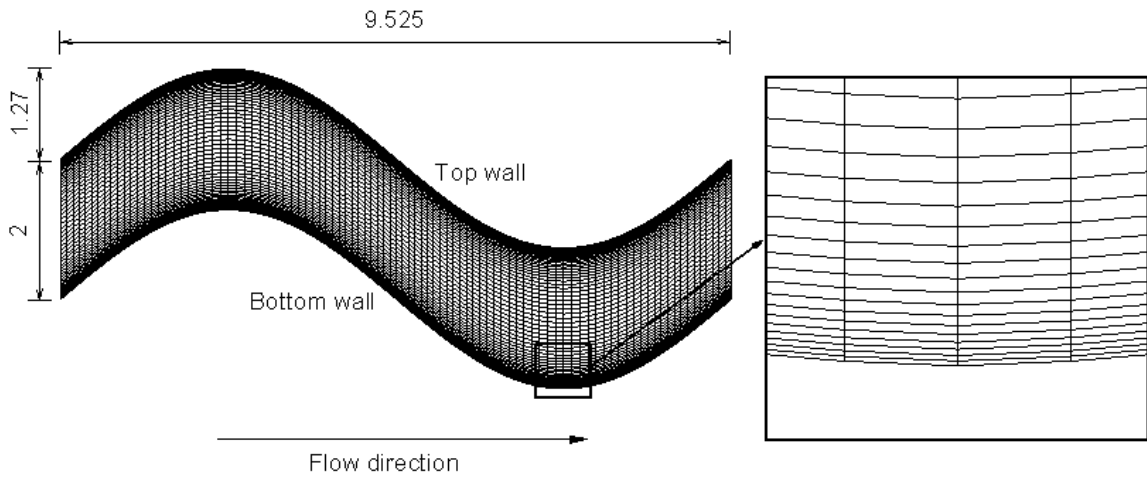


Figure 4-1 Geometric specifications of the wavy channel geometry and the near-wall grid

4.4 Validation

To qualify the grid distribution used in the calculations, computations are performed for a plain channel flow. The flow field obtained is compared to the direct numerical simulation (DNS) results of Kim et al. [26] and the Nusselt number to standard heat transfer correlation. The complete details are provided in Section 3.3.1. Comprehensive results of the flow field and heat transfer in a wavy channel with similar geometric specifications considered in this work are not available. Hence, the comparisons provided with the plain channel flow calculations are a good measure of the accuracy of the results obtained from GenIDLEST. In the calculations, the same grid distribution in the y- and z- directions is maintained while a higher number of grid points in the stream-wise direction is used, since the wavy channel length is 9.525 against the plain channel length of 2π . Also, the Reynolds numbers considered in all the calculations presented in this chapter are less than the $Re_{DH} = 11200$ for the plain channel flow presented earlier.

4.5 Effect of various particle forces

A detailed study of the effect of different particle forces in representative EGR flow conditions is undertaken. Under these conditions, it is observed that thermophoresis and drag are the significant mechanisms which would affect the soot particle deposition process. The particulars are provided in Section 3.3.2. Based on this, all the particle calculations performed consider the effect of these two dominant particle force mechanisms.

4.6 Results and discussion

In the presented work, the main goal is to simulate the flows that usually exist in EGRs and thereby study the process of fouling of the surfaces due to soot particle deposition. Hence, three Reynolds numbers – 1000, 3800 and 10000 are considered for the calculations, which constitute the range of typical EGR flows. The soot particle size in the exhaust gases usually varies over a wide range of values. The study by Kittelson [1] on the particle size distribution indicates the presence of particles ranging from a few nanometers all the way to a few micrometers. Most of the numbers however, are constituted by submicron particles in the range of 10-100 nm and hence, the focus of the present work is on particles of two sizes – 10 nm and 100 nm. These particles are mostly in the nuclei mode and are assumed to be made up of elemental carbon. In Table 4.1, the particle properties used in the calculations are provided.

In the calculations, constant heat flux boundary condition at the walls is imposed, which implies a fixed wall temperature gradient. This is implemented by maintaining the exhaust gas temperature at 600 °C while varying the wall temperature value to obtain the appropriate temperature gradient at the walls, or in other words, the heat flux at the walls. Particle calculations are initialized once the flow field in the channel is fully developed. Initially, particles are suspended on the y-z plane, which is perpendicular to the flow direction. Calculations are performed for three Reynolds numbers at various temperature gradients and the results are discussed in the following sections. Two particle diameters – 10 nm and 100 nm are considered.

Table 4.1 Values of particle and gas properties

Particle properties (Carbon)		
Density (kg/m ³)	2267	
Specific heat (J/Kg/K)	710	
Thermal conductivity (W/m/K)	129	
Diameter (nm)	100	10
Stokes number ($Re_{D_H} = 10000$)	8.903×10^{-4}	6.383×10^{-5}
Stokes number ($Re_{D_H} = 3800$)	4.457×10^{-4}	3.19×10^{-5}
Stokes number ($Re_{D_H} = 1000$)	1.585×10^{-4}	1.136×10^{-5}

4.6.1 Flow features

In Figure 4-2, the three dimensional iso-surfaces of coherent vorticity (refer Chong et al. [42] for details) and contour plots of non-dimensional u-velocity with flow streamlines obtained from the time-averaged mean flow field at $Re_{D_H} = 1000, 3800$ and 10000 are provided. The size of the turbulent eddies is observed to increase as the Reynolds number decreases. At lower Reynolds numbers (1000 and 3800), small recirculation zones exist in the mean, before the crest region of the top wall and the trough region of the bottom wall as seen in Figure 4-2. These recirculation zones become gradually smaller as the Reynolds number is increased, disappearing completely for $Re_{D_H} = 10000$.

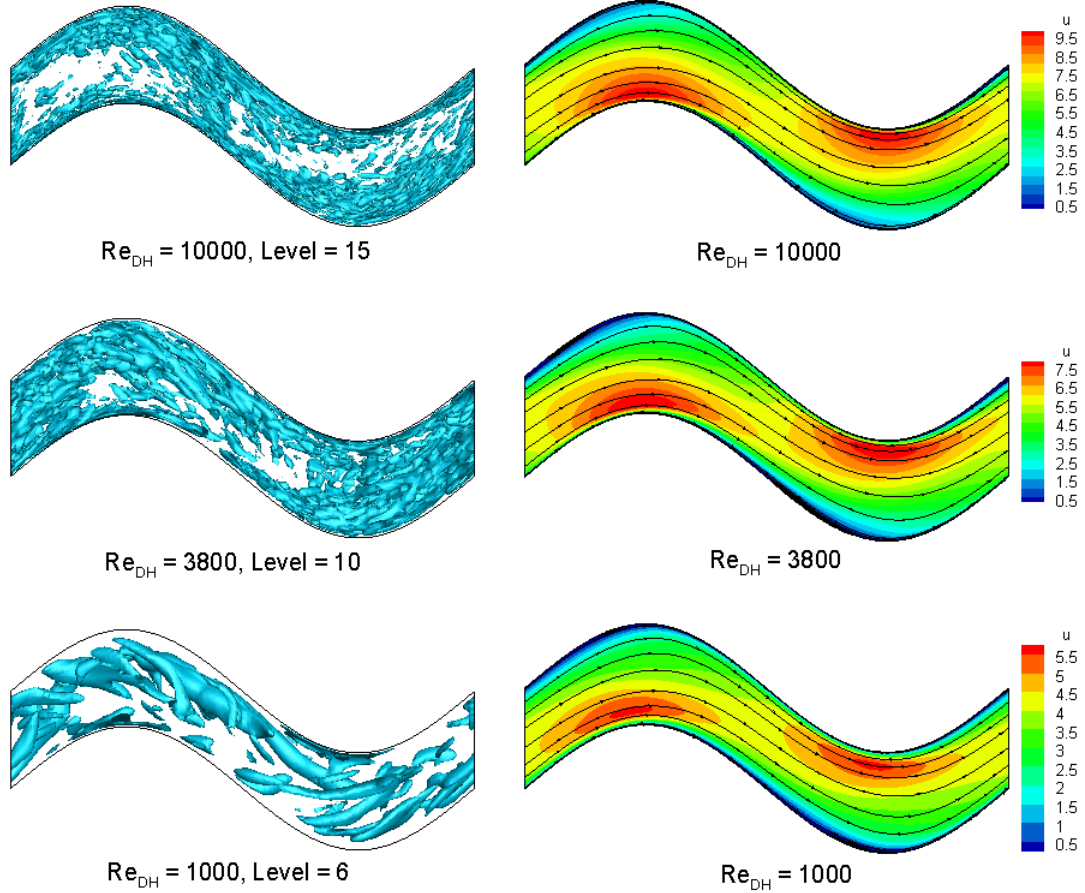


Figure 4-2 Iso-surfaces of coherent vorticity and time-averaged contour plots of non-dimensional u-velocity at different Reynolds numbers

Figure 4-3 presents the time-averaged u-velocity profiles at three cross sections for $Re_{DH} = 10000$. A higher velocity is observed near the bottom wall for $x/L_x = 0.125$ and 0.25 . This is the region of flow acceleration occurring due to the constriction of flow. The three x-locations provided here are in the first half ($0.0 \leq x/L_x \leq 0.5$) of the wavy geometry and similar symmetrically opposite profiles occur in the other half ($0.5 \leq x/L_x \leq 1.0$). Similar profiles are obtained for the other Reynolds numbers.

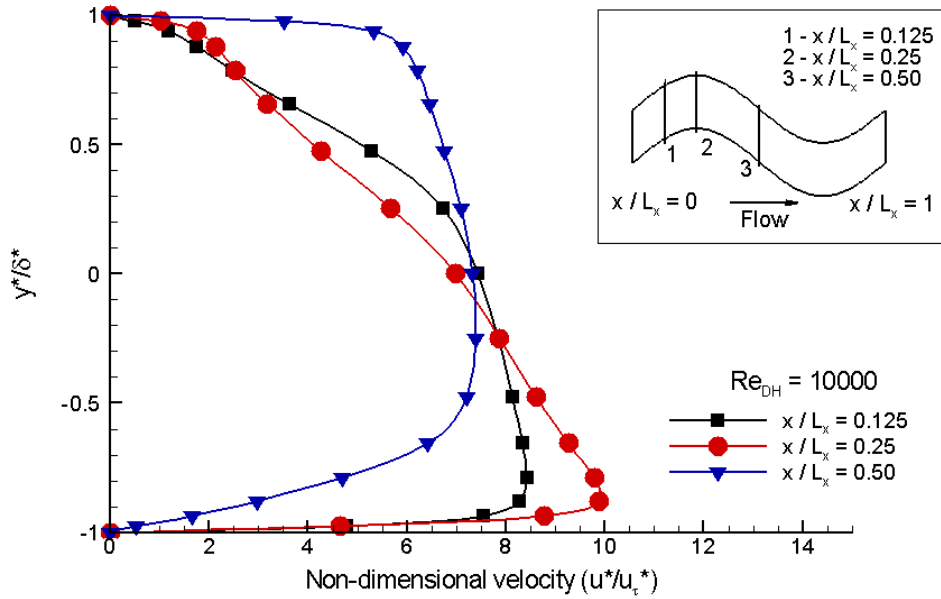


Figure 4-3 Non-dimensional time-averaged u-velocity profiles at $x/L_x = 0.125, 0.25$ and 0.50 for

$$Re_{DH} = 10000$$

The local Nusselt number distributions on the two walls are plotted in Figure 4-4. It is noted that a higher heat transfer occurs before the trough on the top wall and the crest on the bottom wall, due to the flow impingement in these regions of the walls. In the context of particle deposition, this could be an important factor, considering that thermophoresis plays a major role in deposition in the presence of high temperature gradients. Table 4.2 presents the friction factor and Nusselt numbers obtained for the three Reynolds numbers considered.

Table 4.2 Coefficient of friction and Nusselt number for different Reynolds numbers

Reynolds number, Re_{DH}	Coefficient of friction, C_f	Nusselt number, Nu
1000	0.1628	25.56
3800	0.0857	44.27
10000	0.0509	75.48

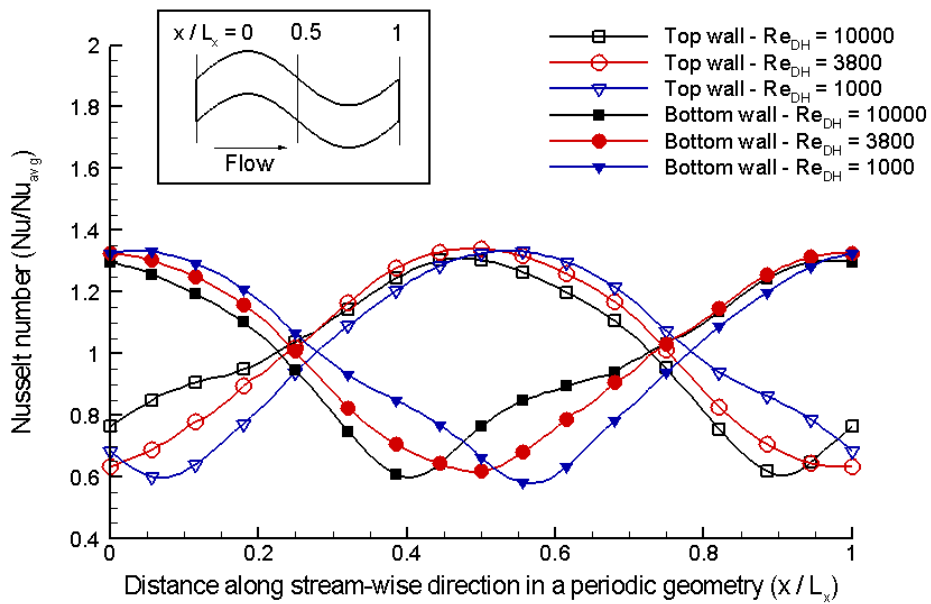


Figure 4-4 Local Nusselt number distribution along the top and bottom walls for different Reynolds numbers

4.6.2 Base results

In this section, results obtained for a flow Reynolds number of 10000 are presented. The Reynolds number is based on the mean channel velocity and hydraulic diameter. From the calculations, the Nusselt number Nu for the flow is calculated to be 74.40. The exhaust gas and the wall temperatures are maintained at 600 °C and 150 °C respectively which results in a wall temperature gradient of 9.45×10^6 K/m.

The number of depositions observed with the stream-wise location of deposition is recorded. A sampling length of five stream-wise pitches is used in all the discussions to analyze the space-averaged deposition behavior. The deposition trends in each of the figures are expressed as deposition fractions, normalized with the number of soot particles remaining in the channel at the entrance to the sampling section.

$$\text{Normalized deposition fraction} = \frac{\text{Number of particles deposited}}{\text{Number of particles entering the sampling section}} \quad 4.4$$

In Figure 4-5, the observed normalized deposition fractions are plotted against the stream-wise location of deposition. Each point in the plot represents the amount of soot deposition observed in the five preceding stream-wise pitches. It is seen that the normalized percentage deposition value is approximately same, over the length of the channel. The total number of depositions observed on the top and bottom walls are approximately same.

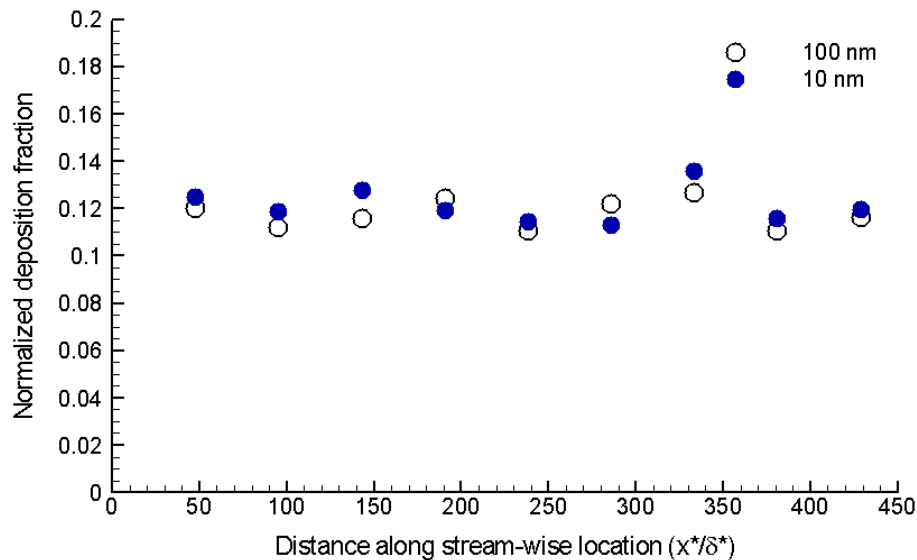


Figure 4-5 Plot of normalized percentage deposition observed along stream-wise direction for 10 and 100 nm particles for $\text{Re}_{D_H} = 10000$, $T_g^* = 600^\circ\text{C}$ and $T_w^* = 150^\circ\text{C}$

Also, the 10 nm and 100 nm soot particles exhibit similar deposition trends, showing same variation of depositions along the length of the channel as well as the same amount of depositions on the top and bottom walls for the two particle diameters. This behavior is also observed in the deposition calculations performed on periodic plain channel discussed in Section 3.3.3. This observation is in agreement with the experimental observations of Munoz-Bueno et al. [12]. The experiments noticed the

significance of thermophoresis as a deposition mechanism and also the independence of particle size on the deposition process in the presence of high wall temperature gradients. The maximum temperature gradients considered in these experiments were around 5.0×10^4 K/m, which is still 1-2 orders smaller compared to the gradients that exist in EGR flows, thus supporting the independence of soot particle size in the calculations at much higher temperature gradients.

4.6.3 Effect of channel geometry

The wavy nature of the EGR cooler walls considered in the present work could result in specific soot particle deposition patterns. All the calculations presented are performed on a periodically repeating geometry and hence to study the effect of the channel geometry, all the depositions are imposed onto a single periodic geometry for this study. Figure 4-6 shows the plot of depositions of 100 nm particles obtained on the top and bottom walls represented in red and violet shades respectively. It is seen that a preferential deposition is observed on the top wall in the region after the crest. Similarly on the bottom wall, higher deposition is observed in the region after the trough.

To confirm the occurrence of preferential deposition, plots of soot particle depositions on the top and bottom walls are provided in Figure 4-7 and Figure 4-8, respectively. The ordinate in the plots is the number of depositions observed on the wall as a percentage of the total number of depositions on it. It is noted that the distribution of the depositions for 10 nm soot particles is comparatively more uniform, i.e., the peaks are slightly lower and lows are slightly higher. This is due to the quicker alignment with fluid flow of 10 nm particles compared to 100 nm particles because of the smaller momentum that the 10 nm particles have of their own. Nevertheless, similar preferential deposition behavior is observed for particles of either size.

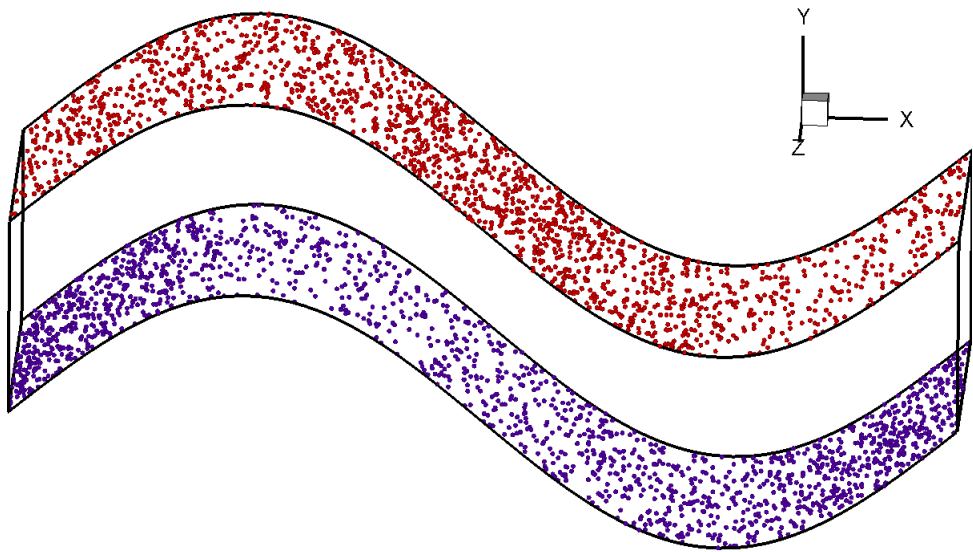


Figure 4-6 100 nm soot particle depositions super-imposed onto one geometric period for $Re_{D_H} = 10000$, $T_g^* = 600^\circ C$ and $T_w^* = 150^\circ C$; red – top wall depositions and violet – bottom wall depositions

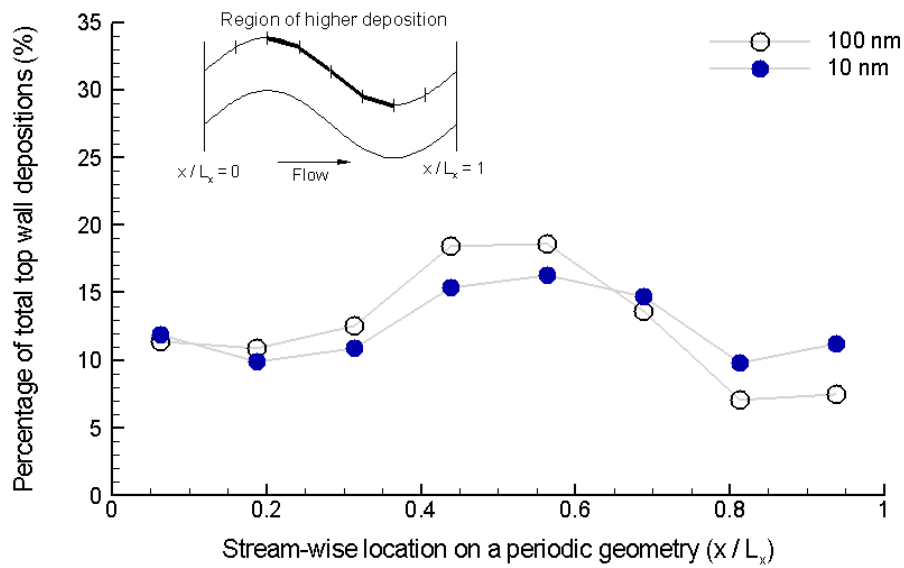


Figure 4-7 Percentage of soot particle depositions plotted against the location of deposition, along with the stream-wise direction on the top wall for $Re_{D_H} = 10000$, $T_g^* = 600^\circ C$ and $T_w^* = 150^\circ C$

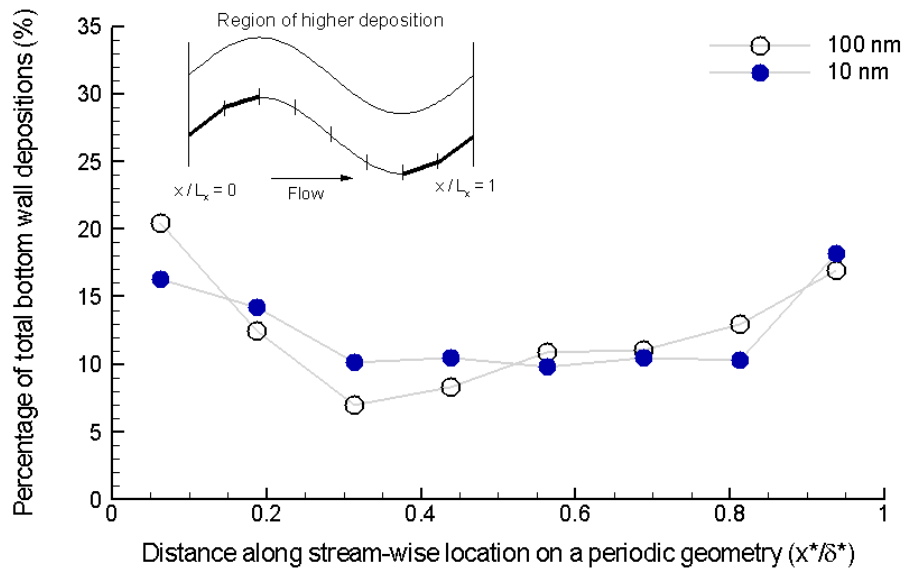


Figure 4-8 Percentage of soot particle depositions plotted against the location of deposition, along with the stream-wise direction on the bottom wall for $Re_{H} = 10000$, $T_g^* = 600 \text{ }^{\circ}\text{C}$ and $T_w^* = 150 \text{ }^{\circ}\text{C}$

The preferential deposition can be explained by the flow features in the wavy channel. The resulting change in the flow direction makes the flow impinge into the wall in these two regions. The accelerating nature of the flow also results in thinner thermal boundary layers with larger local temperature gradients and correspondingly higher local Nusselt number values. This results in higher thermophoretic force on the soot particles in this region acting towards the walls, leading to higher deposition. Figure 4-9 shows the distribution of local Nusselt number on the top and bottom walls. It is seen that the regions of higher deposition on the two walls are regions of higher temperature gradients as well, having significantly higher local Nusselt numbers (approximately 110) when compared to the average on the entire wall (approximately 74). Summarizing, the additional momentum imparted due to the flow and the higher thermophoretic forces due to the larger temperature gradients in these regions of higher heat transfer result in preferential deposition on both the walls.

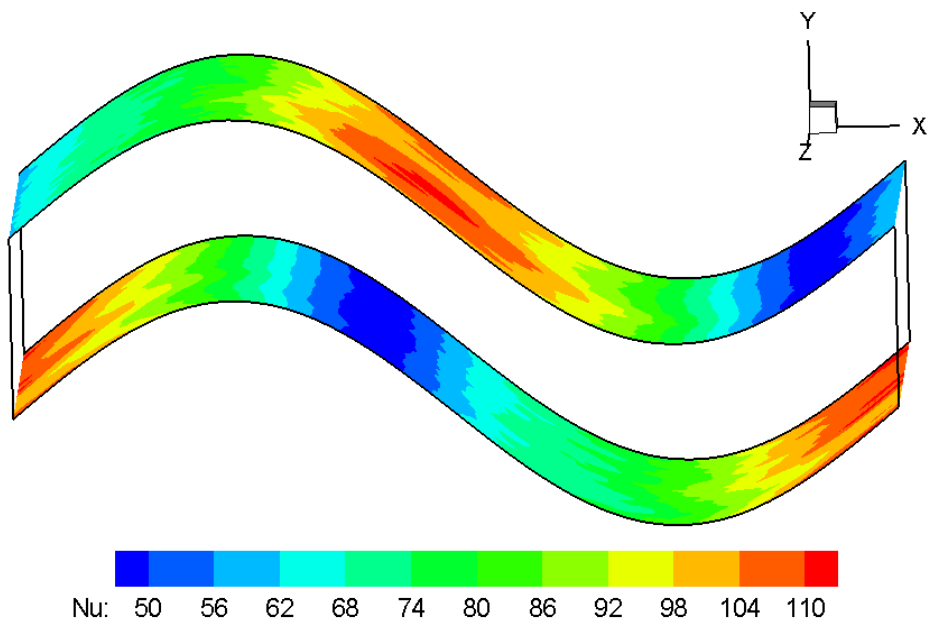


Figure 4-9 Local Nusselt number distribution on the top and bottom walls for $Re_{H} = 10000$

4.6.4 Effect of Reynolds number

Calculations are performed to study the particle deposition process in a wavy channel geometry for three Reynolds numbers as listed in Table 4.3. Corresponding average Nusselt numbers computed and particle Stokes numbers are also listed. The wall temperature is maintained at 150 °C in all the calculations.

Table 4.3 Different Reynolds numbers with the corresponding Nusselt numbers calculated and particle Stokes numbers

Reynolds number	Nusselt number	Stokes number	
		100 nm	10 nm
10000	74.40	8.903×10^{-4}	6.383×10^{-5}
3800	42.48	4.457×10^{-4}	3.19×10^{-5}
1000	28.00	1.585×10^{-4}	1.136×10^{-5}

Figure 4-10 shows the plot of normalized percentage deposition for 100 and 10 nm soot particles at different Reynolds numbers. The normalized percentage deposition over each length of five streamwise pitches is provided. The deposition trends are again noted to be similar for the two particle sizes. For a given Reynolds number, the amount of deposition is seen to be approximately the same. The number of depositions however, is observed to increase considerably as the Reynolds number of the flow is decreased. This is due to the increased particle residence time as the Reynolds number decreases. As a result of this, the thermophoretic forces act on the soot particles for longer durations, hence increasing the number of depositions. For the flow Reynolds number of 1000, the normalized deposition values are noticed to exhibit comparatively more variation. This occurs mainly due to the fact that most of the particles get deposited and the number of particles remaining in the channel is small. Hence, the erratic behavior is just a numerical effect brought in by the high amounts of deposition observed in the initial parts of the channel.

Figure 4-11 and Figure 4-12 show the deposition patterns observed on the top and bottom walls, respectively, for 100 nm particles. A similar trend is observed for 10 nm particles as well. The plots show that at all the Reynolds numbers considered, preferential deposition is seen on the walls. As the Reynolds number decreases, the trend becomes comparatively uniform. As explained in the earlier discussions, the process of flow assisting the deposition in these regions due to impingement and increased wall temperature gradients becomes less prominent at the lower flow velocities due to the higher particle residence times. This results in the relatively uniform deposition at lower Reynolds numbers. However, the location of preferential deposition on the two walls is noted to be the same. In Figure 4-11, an unusual peak is noticed at the beginning of the periodic channel, which is attributed to the initial suspension of particles and is not related to any of the deposition mechanisms.

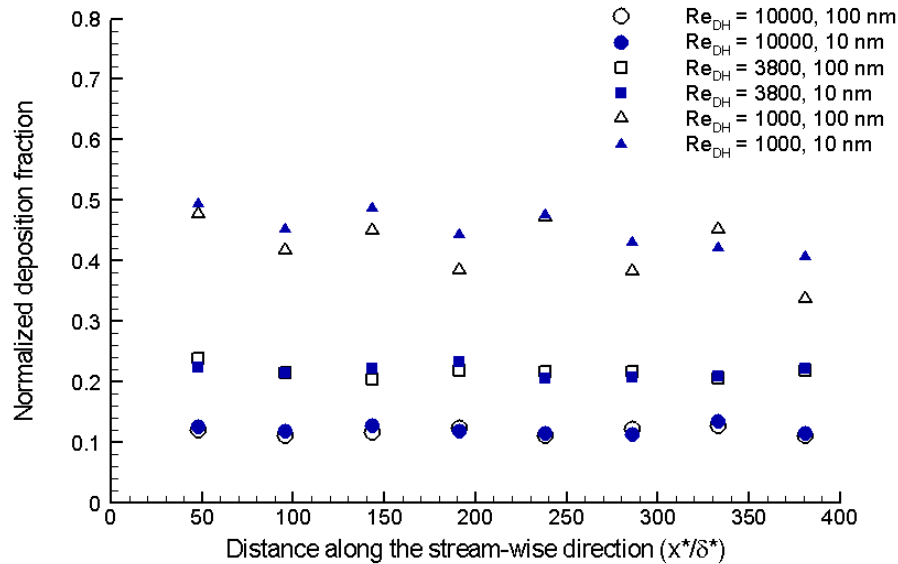


Figure 4-10 Plot of normalized percentage deposition of 100 nm soot particles along stream-wise direction for different Reynolds numbers with $T_g^* = 600^\circ\text{C}$ and $T_w^* = 150^\circ\text{C}$

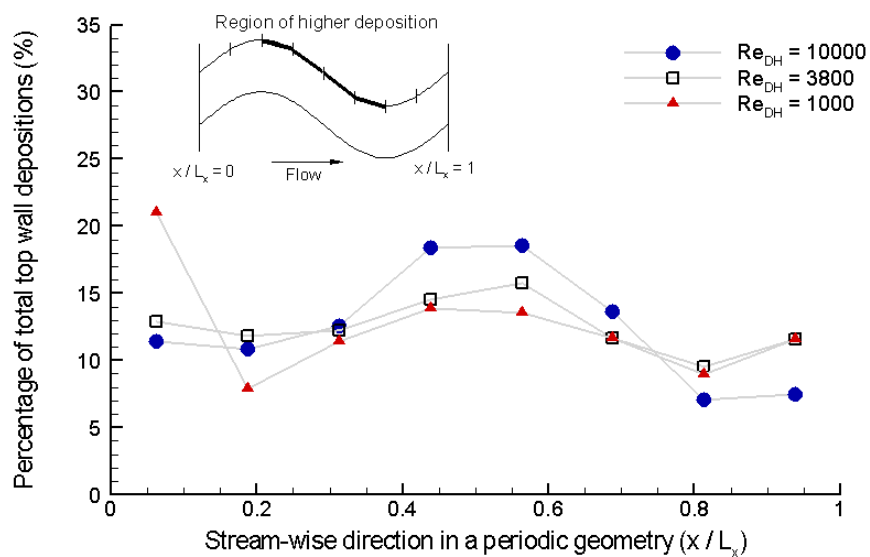


Figure 4-11 Plot of percentage deposition on top wall for 100 nm soot particles at different Reynolds numbers with $T_g^* = 600^\circ\text{C}$ and $T_w^* = 150^\circ\text{C}$

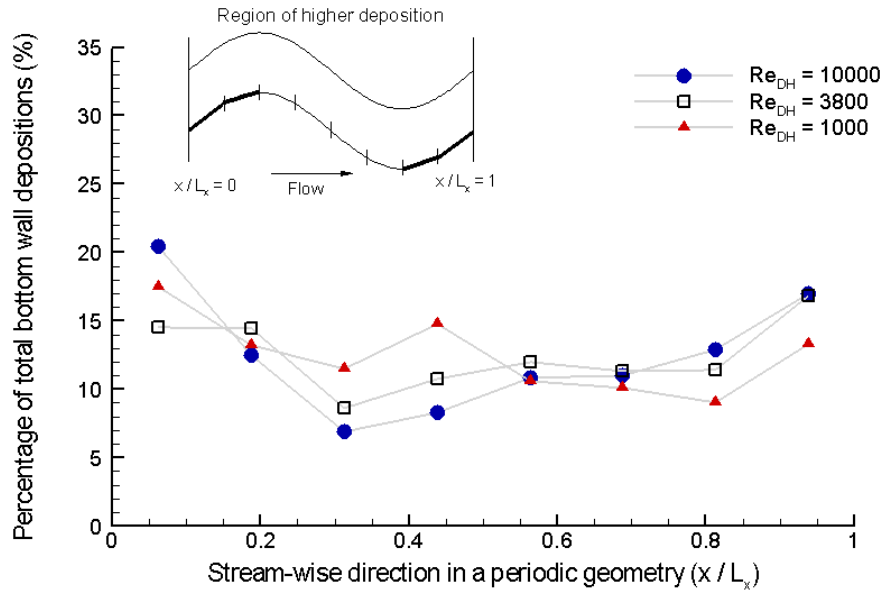


Figure 4-12 Plot of percentage of depositions on south wall for 100 nm soot particles at different Reynolds numbers with $T_g^* = 600^\circ\text{C}$ and $T_w^* = 150^\circ\text{C}$

4.6.5 Deposition trends over time and space

To study the soot deposition trends at different Reynolds numbers further, the number of depositions is plotted against the physical time and location of deposition in Figure 4-13 and Figure 4-14, respectively. In Figure 4-13, the physical time for all the cases is non-dimensionalized with the time scale used for $Re_{DH} = 10000$. It is noted that the number of depositions for a given physical time increases as the Reynolds number increases. However, it should be noted that for higher Reynolds numbers, the fluid velocity is also higher, resulting in the flow and the particles in the flow field to move much larger distances along the channel compared to the lower Reynolds numbers. This aspect is clearly depicted in Figure 4-14. It is seen that with respect to the location of deposition, lower Reynolds numbers result in higher deposition. This behavior is mainly due to the particles having a higher residence times in flows at low Reynolds numbers.

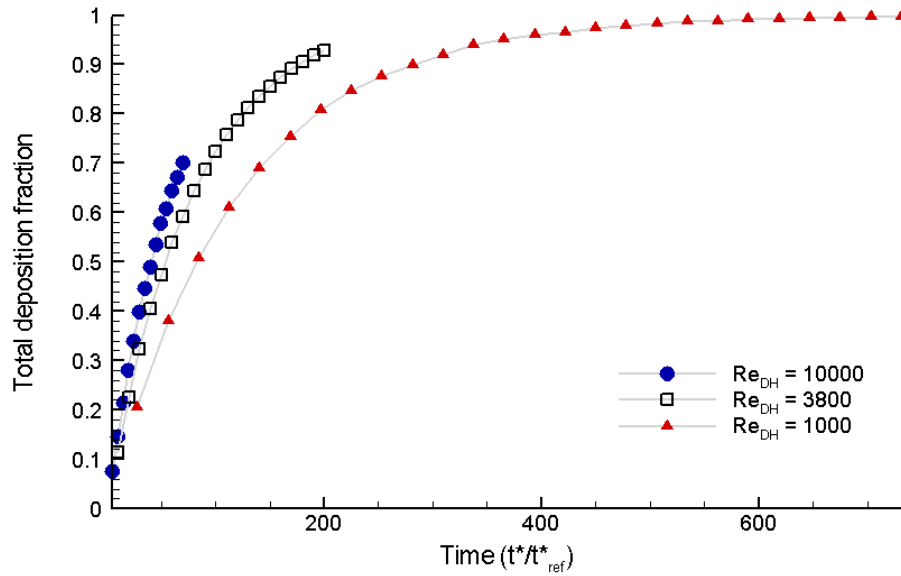


Figure 4-13 Plot of percentage deposition observed for 100 nm soot particles against physical time for different Reynolds numbers with $T_g^* = 600^\circ\text{C}$ and $T_w^* = 150^\circ\text{C}$

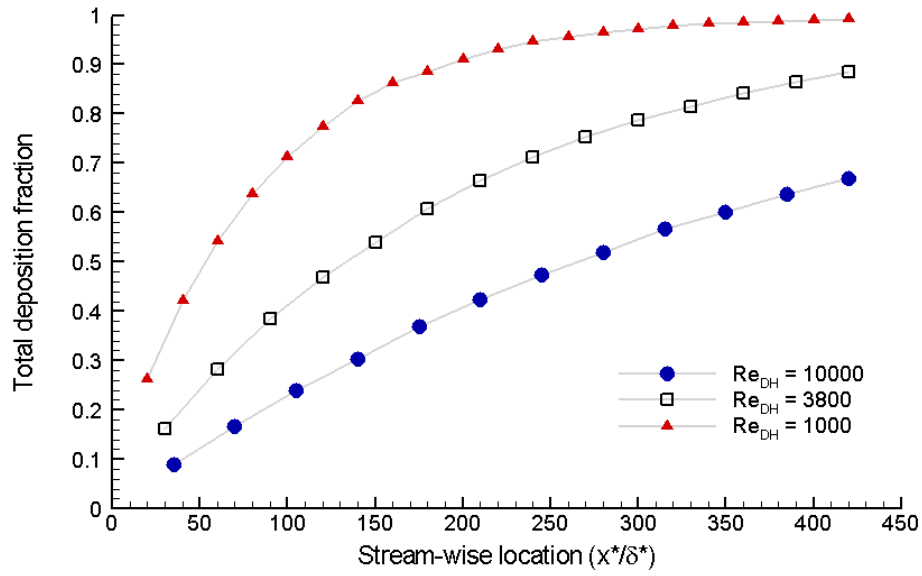


Figure 4-14 Plot of percentage deposition observed for 100 nm soot particles against stream-wise location of deposition for different Reynolds numbers with $T_g^* = 600^\circ\text{C}$ and $T_w^* = 150^\circ\text{C}$

4.6.6 Effect of wall temperature gradient

Calculations are performed with various wall temperature gradients to study the effect of heat flux at the walls on particle deposition. Various wall temperature values are used while maintaining the gas temperature constant at 600 °C. The Reynolds number in the channel is maintained at 10000. The corresponding wall temperature gradient is computed as mentioned in Section 4.2. The wall temperature is taken as the reference temperature for calculation of the thermophoretic force. The calculated near wall-temperature gradients, its ratio over reference temperature and the observed normalized deposition fractions for different wall temperatures are provided in the Table 4.4. Again, five stream-wise pitches are taken as the sampling length for the normalization of deposition fractions.

Table 4.4 Temperature gradients, ratio of temperature gradient to reference temperature and the calculated normalized deposition fractions and preferential deposition values on the top wall for

different wall temperatures for $Re_{H} = 10000$

Wall temperature T_w^* (in K)	Temperature gradient at wall $\frac{dT^*}{dy^*} \Big _w$ (in K/m)	Ratio of wall temperature gradient over reference fluid temperature	Normalized deposition fractions	
			100 nm	10 nm
423	9.450×10^6	2.23×10^4	0.701	0.708
550	6.783×10^6	1.23×10^4	0.502	0.508
658	4.515×10^6	6.86×10^3	0.334	0.331
766	2.247×10^6	2.93×10^3	0.187	0.172
850	4.83×10^5	5.68×10^2	0.088	0.086

Figure 4-15 shows the plot of deposition fractions for 10 nm and 100 nm soot particles observed for different wall temperature gradients. The abscissa in the plot is taken as the ratio of the wall

temperature gradient to the reference temperature used in the calculation. Since the thermophoretic force formulation involves this exact ratio, the deposition pattern is studied with this ratio rather than just the temperature gradient term. This helps in confirming the dependence of particle deposition on the thermophoretic force, as established in the study on effect of particle forces in Section 3.3.2. It is seen that for both the soot particle sizes considered, the normalized deposition fraction exhibits a linear variation for different wall temperature gradients.

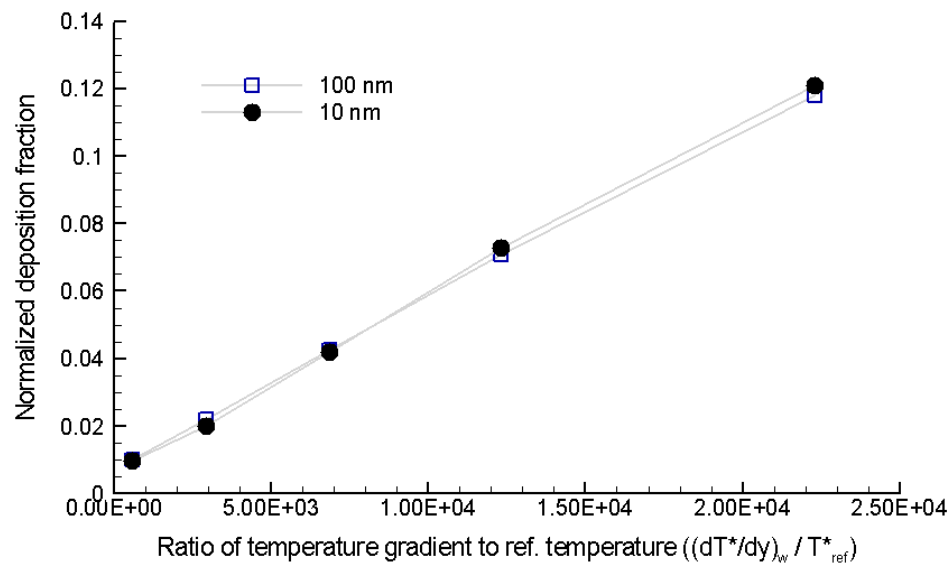


Figure 4-15 Plot of percentage of depositions for every 5 stream-wise pitches along the flow direction against the ratio of wall temperature gradient to reference fluid temperature ($Re_{D_H} = 10000$)

Preferential deposition for different temperature gradients

The locations of particle depositions are super-imposed on a single periodic geometry to study the effect of different temperature gradients on the preferential deposition observed in wavy channels. Figure 4-16 and Figure 4-17 give the plots of percentage deposition at various wall temperatures on the top and bottom walls, respectively. It is noted that the peak values are much higher for the lower temperature

gradients indicating more dominant preferential deposition for flow with lower temperature gradients. As the temperature gradient decreases, due to the lower thermophoretic force, the particles tend to align with the flow quicker. Thus, more number of depositions is observed in the regions where the flow is directed towards the walls. On the other hand, in the regions where the flow is directed away from the walls, much smaller number of depositions is observed due to the significantly reduced wall temperature gradient.

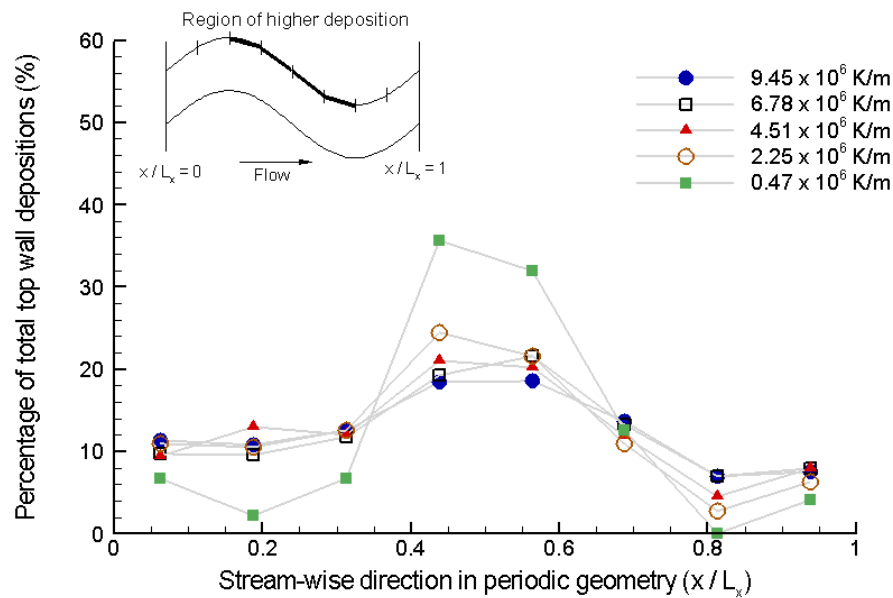


Figure 4-16 Distribution of percentage deposition on a periodic geometry on the top wall for $\text{Re}_{\text{D}_H} = 10000$

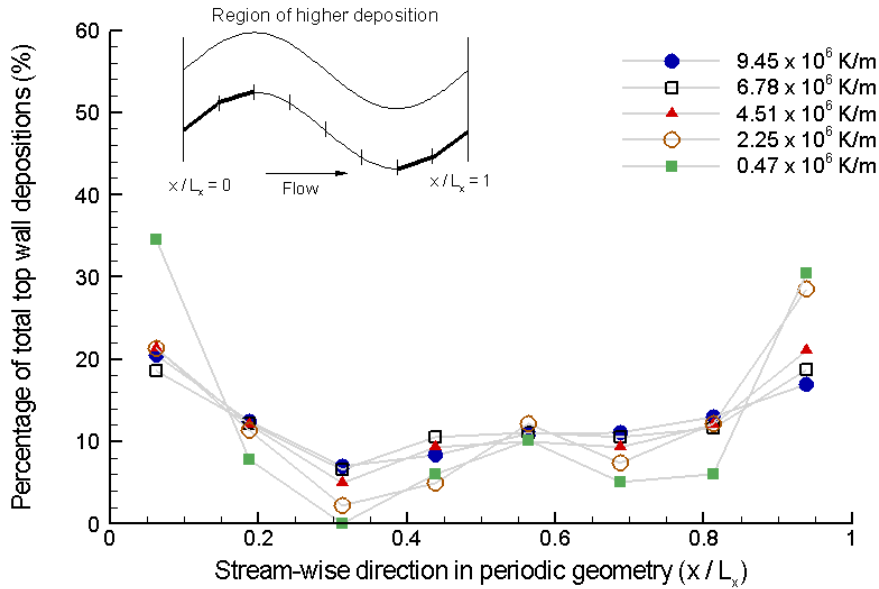


Figure 4-17 Distribution of percentage deposition on a periodic geometry on the bottom wall for

$$Re_{DH} = 10000$$

4.7 Summary and conclusions

In this chapter, the process of particle deposition in a wavy channel geometry, periodic in the stream-wise and lateral directions is studied. The effect of channel geometry, Reynolds number and the applied temperature gradient on the deposition is analyzed in considerable detail. The salient conclusions from the calculations are presented below.

1. The 10 nm and 100 nm particles exhibit similar deposition characteristics.
2. Preferential deposition is observed in some regions of the walls, indicating dependence of the deposition process on the channel geometry. The nature of the flow field and the corresponding thermal field in the wavy channel mainly contribute to preferential deposition.
3. Particle deposition is very sensitive to the Reynolds number of the flow. The lower Reynolds number flows exhibit considerably higher deposition. Preferential deposition is observed in all the different Reynolds number flows considered.

4. The applied wall temperature gradient is also an important factor in the process of deposition. The amount of deposition decreases with reduction in wall temperature gradient.

Chapter 5

Soot particle deposition in a developing wavy channel

5.1 Introduction

In continuation with the study of fouling in wavy fin EGR coolers, this chapter presents soot particle deposition in a developing wavy channel flow. In contrast to the periodic calculations where constant heat flux boundary condition was used, the developing flow framework allows the specification of wall temperature distributions. This allows better representation of the thermal boundary conditions which typically exist in EGR flows. Two thermal boundary conditions - spatially constant and spatially varying wall temperature distributions are used. The calculations are performed for 10 nm and 100 nm sized soot particles at two representative flow Reynolds numbers.

5.2 Methodology

All the calculations are performed using the in-house code Generalized Incompressible Direct and Large Eddy Simulation of Turbulence (GenIDLEST). The governing mathematical equations used for the carrier and dispersed phases are provided in Section 2.1 and Section 2.2 respectively.

The inlet velocity u_{in}^* and the channel half-width δ^* are used as the reference velocity and length scales, respectively. The non-dimensional form of the temperature is given below:

$$\theta = \frac{T^* - T_{ref}^*}{T_0^*} \quad 5.1$$

where, $T_0^* = T_{in}^* - T_{ref}^*$ is the characteristic temperature and T_{ref}^* is the reference temperature. For constant wall temperature boundary condition, T_w^* is used as the reference value. When a varying wall temperature boundary condition is implemented, the wall temperature at the inlet of the channel is used as the reference. The wall temperature distributions used for the calculations are discussed in Section 5.5.3. With the above temperature non-dimensionalization, the non-dimensional heat flux is then given by:

$$q'' = -\frac{d\theta}{dy}\Big|_w \quad 5.2$$

The heat flux is non-dimensionalized with $q_0^* = \kappa^* \cdot T_0^* / \delta^*$. The average near-wall temperature gradient, hereafter referred to as the wall temperature gradient, and the heat flux at the walls hence can be used interchangeably. The dimensional value of the wall temperature gradient can be calculated in terms of the dimensional heat flux as:

$$\frac{dT^*}{dy^*}\Big|_w = \frac{q''^*}{\kappa^*} \quad 5.3$$

The local Nusselt number at the walls at each location on the wall is calculated as:

$$Nu_{local} = \frac{q''}{\theta_w - \theta_m} \quad 5.4$$

where, θ_m is the non-dimensional bulk mean temperature and θ_w is non-dimensional wall temperature at that location. The mean Nusselt number Nu_{DH} is then computed by performing an area averaging of the local Nusselt number values.

5.3 Geometry and computational grid

The developing flow simulations are performed in a wavy fin EGR cooler geometry, spanning a length of ten stream-wise pitches. Each pitch consists of sinusoidal wave shaped top and bottom walls, which are in-phase, thus maintaining a constant separation width of $2\delta^*$. This is the same geometry used in the periodic wavy channel calculations presented in Chapter 4. Figure 5-1 shows the specifications of the geometry used in the simulations. A plain-channel section is used at the exit of the channel as shown, to avoid any outflow disturbances propagating into the domain. The computational grid used is also shown, with a close-up view of the near-wall mesh. A resolution of $96 \times 64 \times 64$ is used for each pitch, in the x-, y- and z- directions, respectively, with a total grid size of 4.3 million cells for the full geometry. The domain is periodic in the lateral (z-) direction.

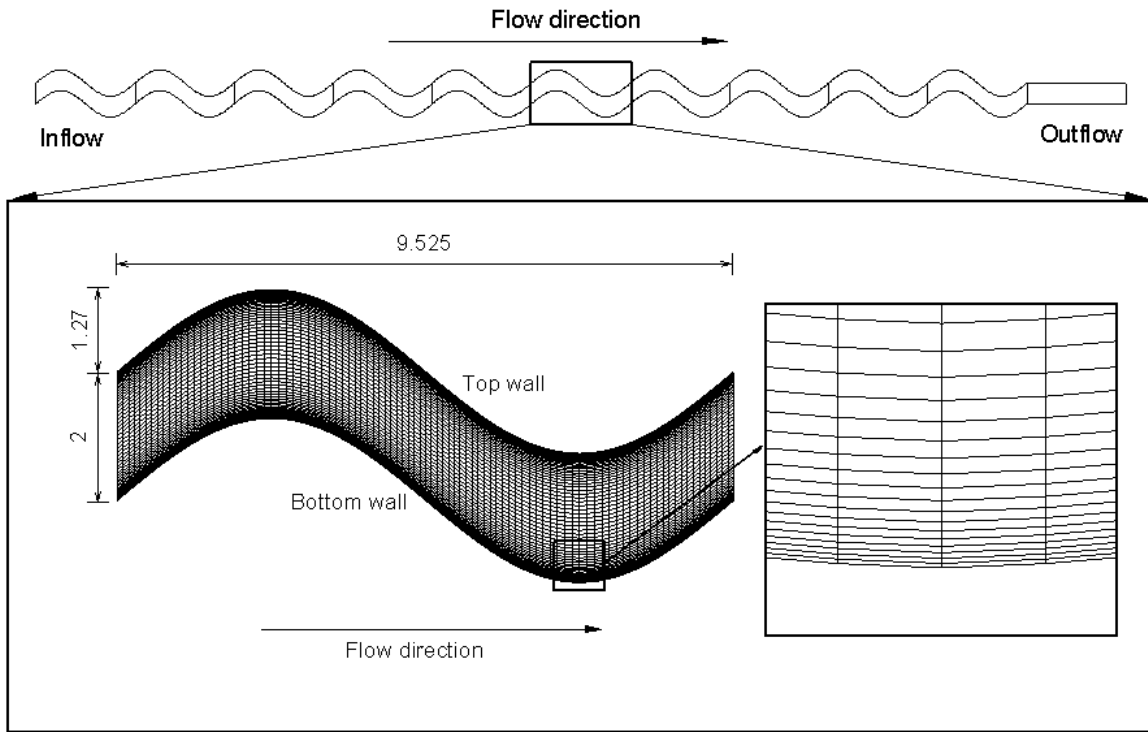


Figure 5-1 Geometric specifications of the wavy channel used in the calculations

5.4 Validation

The main focus of the particle deposition study in the developing EGR cooler is in the regions where the flow is fully developed. Hence, the validation presented for the periodic wavy channel in Section 4.4 is sufficient for the developing flow calculations as well. This is a fair assumption, since actual EGR coolers typically are made up of 30-40 stream-wise pitches and for the Reynolds numbers considered in the presented calculations, the flow is fully developed by the end of 2-3 pitches.

5.5 Results and discussion

In order to simulate the process of fouling in EGR coolers, calculations are performed for flow fields that exist in a typical EGR cooler. Two flow Reynolds numbers – 1000 and 3800, which are representative of typical EGR cooler flows, are considered. As mentioned in Section 4.6, most of the soot

particles are in the size range of 10 nm – 100 nm. Again, properties of elemental carbon are used for the particles and are provided in Table 5.1.

Table 5.1 Properties of particles used in all the calculations

Particle properties (carbon)		
Density (kg/m ³)	2267	
Specific heat (J/Kg/K)	710	
Thermal conductivity (W/m/K)	129	
Diameter (nm)	100	10
Stokes number ($Re_{DH} = 3800$)	7.697×10^{-4}	6.751×10^{-5}
Stokes number ($Re_{DH} = 1000$)	4.602×10^{-4}	-

Two thermal boundary conditions are considered - constant wall temperature and a spatially varying wall temperature. The constant wall temperature case helps in the fundamental study of the soot particle deposition trends in a wavy channel EGR cooler geometry. On the other hand, the varying wall temperature case aids the understanding soot particle fouling simulation in conditions that typically exist in an EGR cooler.

At the start of the each simulation, soot particles are inserted into the computation domain at the inlet surface, on the y-z plane perpendicular to the flow direction. The initial locations of the particles are generated randomly on the inlet plane. The deposition trends in the EGR cooler will be expressed as the normalized deposition fraction observed in a sampling length of one stream-wise pitch and is defined as:

$$\text{Normalized deposition fraction} = \frac{\text{Number of particles deposited}}{\text{Number of particles entering the sampling section}} \quad 5.5$$

5.5.1 Flow features

Development length

The initial uniform laminar flow entering the wavy channel conforms to the flow geometry in the initial few pitches. The flow becomes nominally fully developed by the end of 3rd and 2nd pitches for $Re_{DH} = 1000$ and 3800, respectively. To confirm the hydrodynamic and thermal development length of the flow, the time-averaged u-velocity and temperature profiles at geometrically identical locations ($x / L_x = 0.5$) in the initial six pitches is plotted in Figure 5-2 obtained with a spatially varying wall temperature boundary condition is presented.

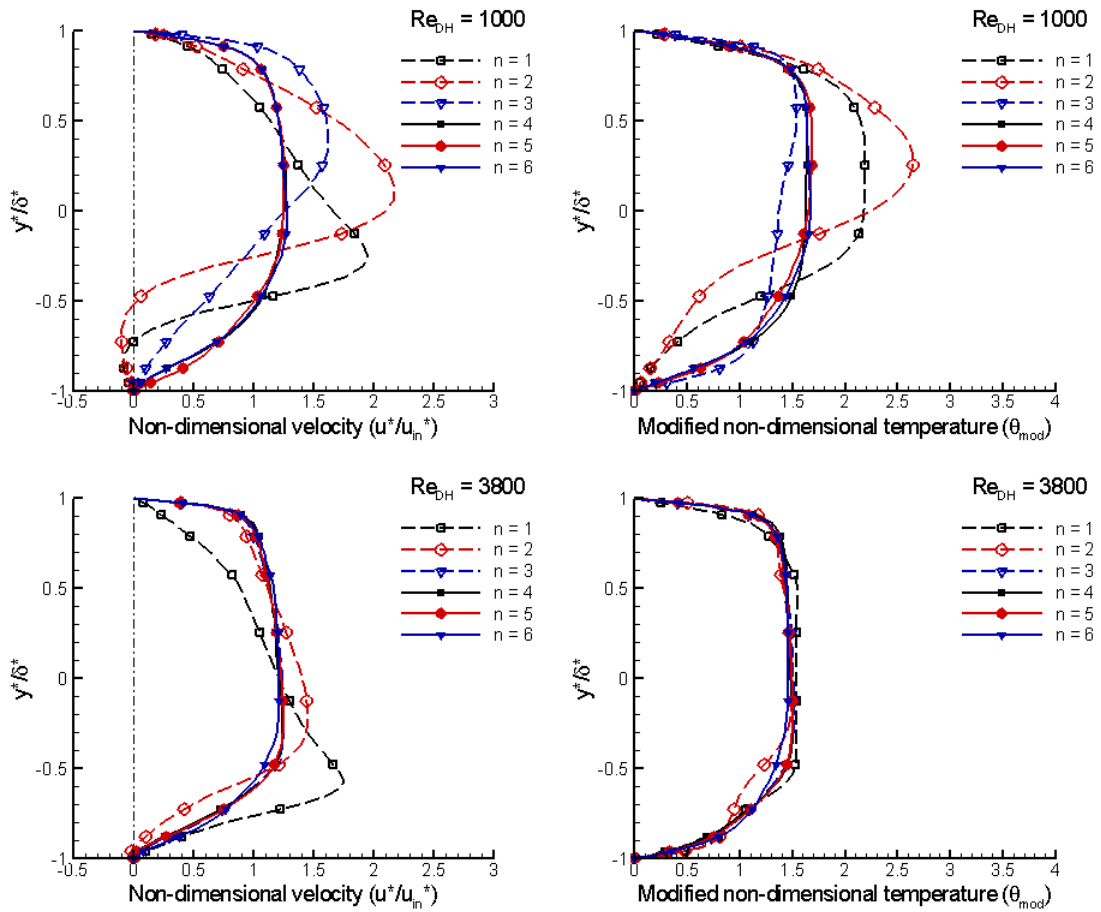


Figure 5-2 Time-averaged velocity and modified temperature profiles at $x/L_x = 0.5$ in the initial six pitches for $Re_{DH} = 1000$ and 3800

The modified temperature for thermal profile comparison is given by:

$$\theta_{mod} = \frac{\theta - \theta_w}{\theta_m - \theta_w} \quad 5.6$$

It is clearly seen that both the velocity and temperature profiles are nominally fully-developed by the end of the 3rd and 2nd pitches for $Re_{D_H} = 1000$ and 3800, respectively.

Flow structure and transition to turbulence

The location of transition to turbulence has an impact on the deposition by increasing the wall temperature gradients. In order to visualize the presence of turbulent structures in the flow field, the instantaneous three dimensional iso-surfaces of coherent vorticity are plotted. In Figure 5-3, the iso-surfaces of coherent vorticity and contour plots of the time-averaged u-velocities in the 2nd and 8th pitch are shown for $Re_{D_H} = 3800$. It is noted that due to the uniform velocity profile used at the inlet, the flow is laminar in the 1st pitch. The process of transition is initiated by shear layer separation and two-dimensional Kelvin-Helmholtz instabilities which quickly transition from the base instability to three-dimensional instabilities as seen in the top view of the iso-surfaces plot provided in Figure 5-3 for $Re_{D_H} = 3800$.

The contour plots indicate the presence of recirculation zones predominantly in the regions where the flow is still laminar or is transitioning to turbulence. Once the flow transitions to turbulence, the recirculation zones become noticeably smaller or completely disappear.

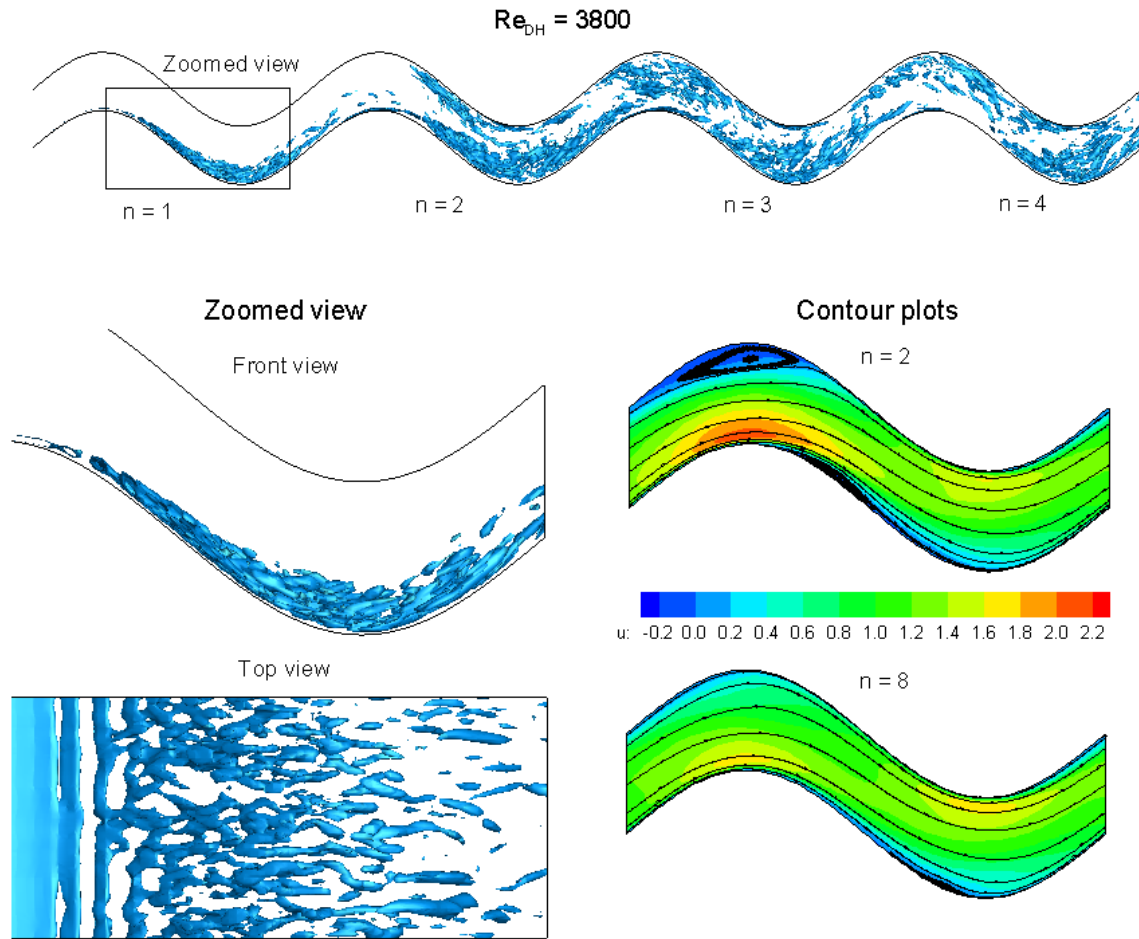


Figure 5-3 Iso-surfaces of coherent vorticity (value = 3) in the initial four pitch and contour plots of u-velocities in 2nd and 8th pitches for $Re_{DH} = 3800$

The nature of the flow features observed for $Re_{DH} = 1000$ are similar to those observed for $Re_{DH} = 3800$ and is presented in Figure 5-4. A few differences exist, however, and are discussed here. It is observed that the flow is still in the laminar regime in the 2nd pitch compared to the transitional flow for $Re_{DH} = 3800$. Hence, the recirculation zones are much larger for $Re_{DH} = 1000$ and exist on both the walls, while for $Re_{DH} = 3800$, they are smaller and are non-existent on the bottom wall due to the turbulent nature of the flow. Also, for $Re_{DH} = 1000$, the transition process is delayed due to the

comparatively lower flow velocity. The resulting instabilities in the flow are observed only in the 2nd pitch, compared to the 1st pitch for $Re_{DH} = 3800$. The initiation of transition is hence observed only by the end of the 2nd pitch, followed by increased mixing in the 3rd pitch to render the flow fully turbulent. As a consequence, an increase in the overall heat transfer in the 3rd pitch is observed indicated by the increased Nusselt number in this pitch.

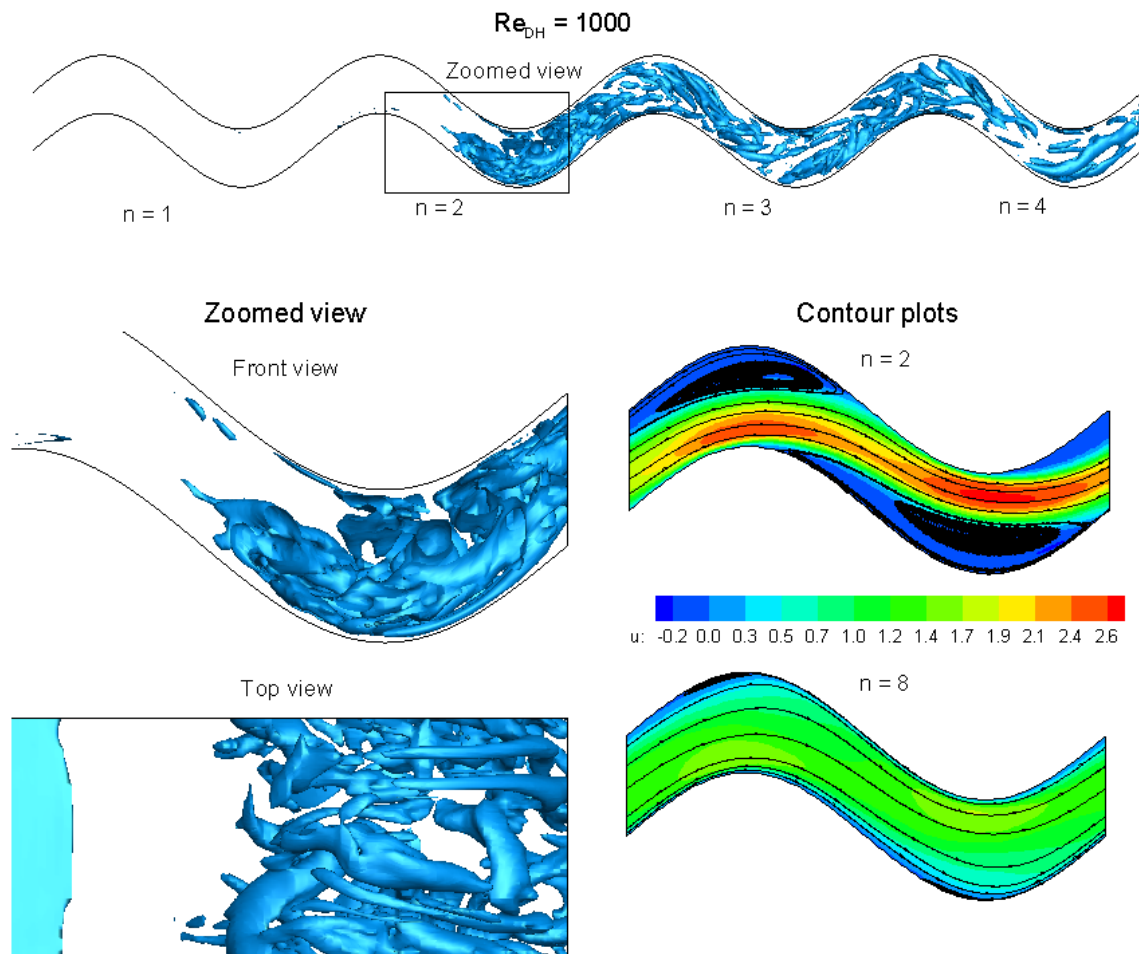


Figure 5-4 Iso-surfaces of coherent vorticity (value = 2) in the initial four pitch and contour plots of u-velocities in 2nd and 8th pitches for $Re_{DH} = 1000$

In the fully-developed region, the flow structure existing for both Reynolds numbers is same as that obtained from the periodic wavy channel calculations. Similarly, the local Nusselt number

distribution for the fully-developed region is the same as that obtained for periodic calculations. The detailed results are presented in Section 4.6.1.

Figure 5-5 provides the variation of the average Nusselt number for each stream-wise pitch obtained for both the Reynolds numbers. The effect of flow development is clearly seen for both the Reynolds numbers as the Nusselt number attains a uniform value after 4th and 3rd pitch for $Re_{DH} = 1000$ and 3800 respectively. For $Re_{DH} = 1000$, a higher Nusselt number is observed in the 3rd pitch due to the turbulent mixing that occurs in this region of the flow which eventually renders the flow fully turbulent. On the other hand, the transition to turbulence for $Re_{DH} = 3800$ is more gradual because the flow is turbulent from the 1st pitch and hence the variation in Nusselt number is comparatively smoother.

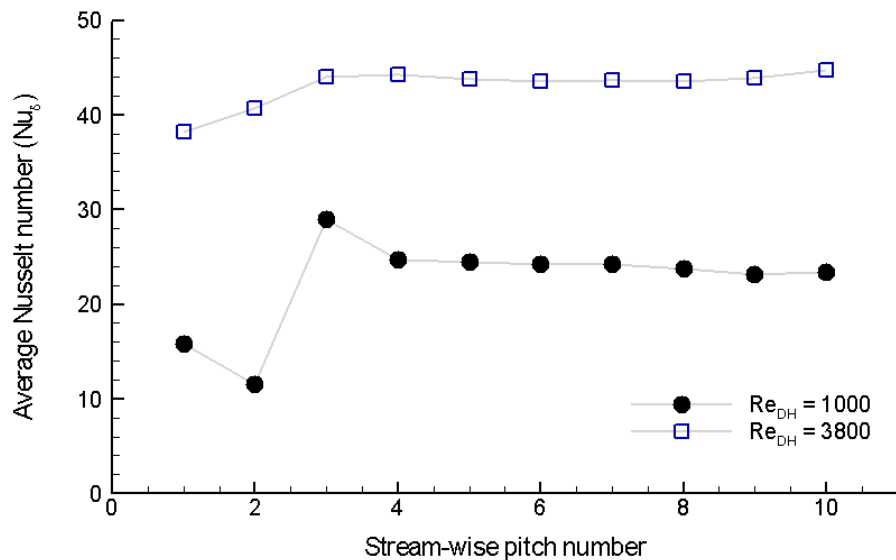


Figure 5-5 Average Nusselt number distribution for every stream-wise pitch for $Re_{DH} = 1000$ and 3800

5.5.2 Soot deposition with constant wall temperature

This section presents discussion on the soot particle deposition with constant wall temperature boundary condition. Calculations are performed for the two soot particle sizes – 10 nm and 100 nm. The flow Reynolds number Re_{D_H} is maintained at 3800. An inlet gas temperature of 600 °C and wall temperature of 150 °C are used. In non-dimensional terms, these values correspond to 1 and 0, respectively.

Deposition

In Figure 5-6, the normalized deposition fraction obtained in each stream-wise pitch is plotted against the pitch index. The sampling length is one stream-wise pitch, which means that each point on the plot corresponds to the amount of soot deposition observed in the corresponding pitch, normalized with the number of particles entering the pitch. It is seen that the amount of soot deposition decreases along the length of the channel. This is due to the continuously decreasing exhaust gas temperature, which results in a drop in the temperature gradient or in effect the heat transfer to the walls. This is observed in the plot of time-averaged near-wall temperature gradient across the channel length. It is noticed that the nature of variation of amount of deposition is very similar to the variation of wall temperature gradient. This indicates a direct relation between the amount of deposition occurring and the corresponding wall temperature gradient or heat transfer. This aspect is further explored in the subsequent discussions.

Also, the 10 and 100 nm soot particles exhibit similar deposition trends, showing the same variation of depositions along the length of the channel as well as the same amount of depositions on the top and bottom walls for the two particle diameters. This behavior is also observed in the deposition calculations performed on periodic plain and wavy channels discussed in Chapter 3 and Chapter 4, respectively. This observation is in agreement with the experimental observations of Munoz-Bueno et al. [12]. The experiments noticed the significance of thermophoresis as a deposition mechanism and also the independence of particle size on the deposition process in presence of high near-wall temperature

gradients. The maximum temperature gradients considered in these experiments were around 5.0×10^4 K/m, which is still 1-2 orders lesser compared to the gradients that exist in EGR flows.

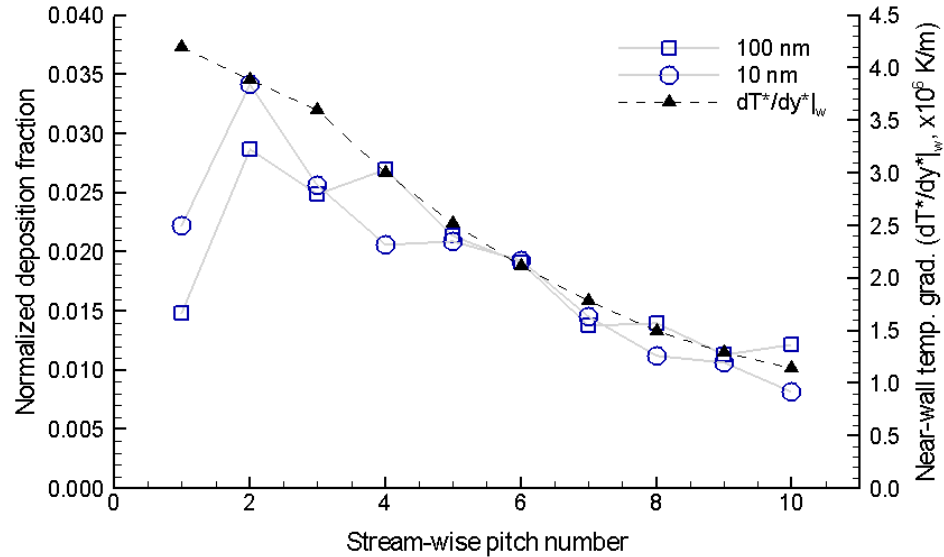


Figure 5-6 Normalized percentage deposition along the developing channel for 10 and 100 nm particles at $Re_{D_H} = 3800$ with $T_w^* = 150^\circ C$ and $T_g^* = 600^\circ C$

Preferential deposition

Soot deposition patterns are studied on the top and bottom walls separately and on a single stream-wise pitch onto which all depositions are super-imposed. In the first 2 pitches of the channel, different deposition patterns are observed. This is due to a combined effect of (i) developing flow in this region and (ii) the inlet conditions used. As a uniform velocity profile at the inlet in the x- direction is used, the flow and the soot particles impinge on the bottom wall as soon as they enters the channel and hence, higher soot deposition is seen on the bottom wall compared to the top wall in this region. Hence, to investigate the preferential deposition, the initial two pitches are excluded. Figure 5-7 and Figure 5-8 provide plots of soot depositions super-imposed on a single stream-wise pitch, starting from the third pitch. It is observed that for both 10 nm and 100 nm soot particles, higher amounts of deposition are seen

in certain regions on the top and bottom walls which correspond to regions of higher heat transfer. This is a process also seen in periodic wavy channels and is explained in detail in Section 4.6.3.

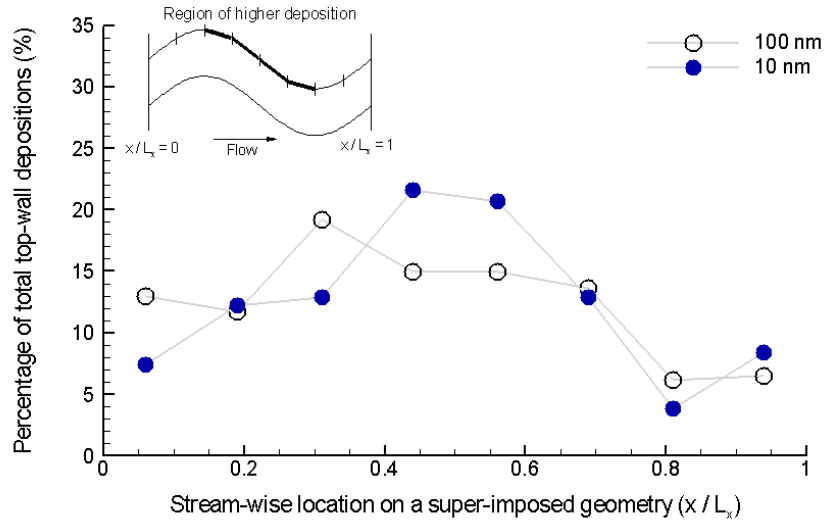


Figure 5-7 Number of depositions observed on the top wall super-imposed onto a single stream-wise pitch (starting from 3rd pitch)

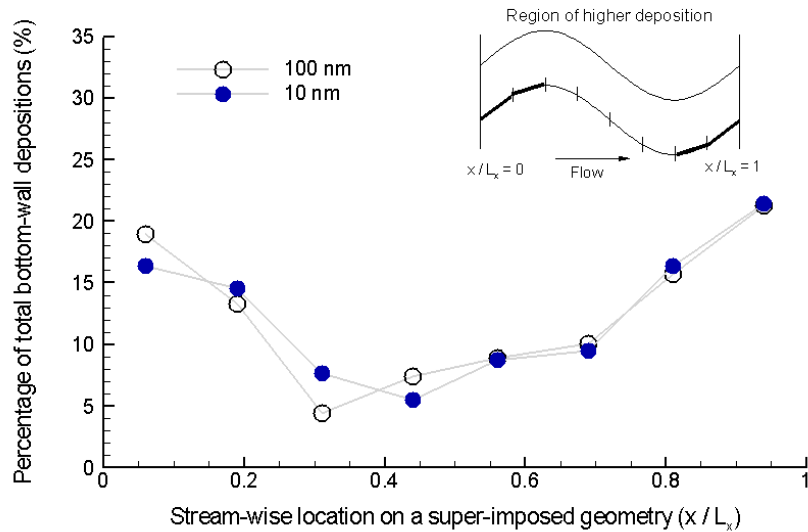


Figure 5-8 Number of depositions observed on the bottom wall super-imposed onto a single stream-wise pitch (starting from 3rd pitch)

5.5.3 Soot deposition with varying wall temperature

For a typical counter-flow EGR cooler arrangement, the wall temperature is higher near the inlet due to the hot exhaust gas entering the cooler and gradually decreases towards the exit. A spatially varying temperature distribution on the EGR cooler surface is used. Two flow Reynolds numbers – 1000 and 3800 are considered. In Figure 5-9, the wall temperature distributions used for the two Reynolds numbers are shown. It should be noted that in the temperature non-dimensionalization, the wall temperature at the inlet ($x = 0$) is taken as the reference temperature and hence, the value at the inlet is 0.

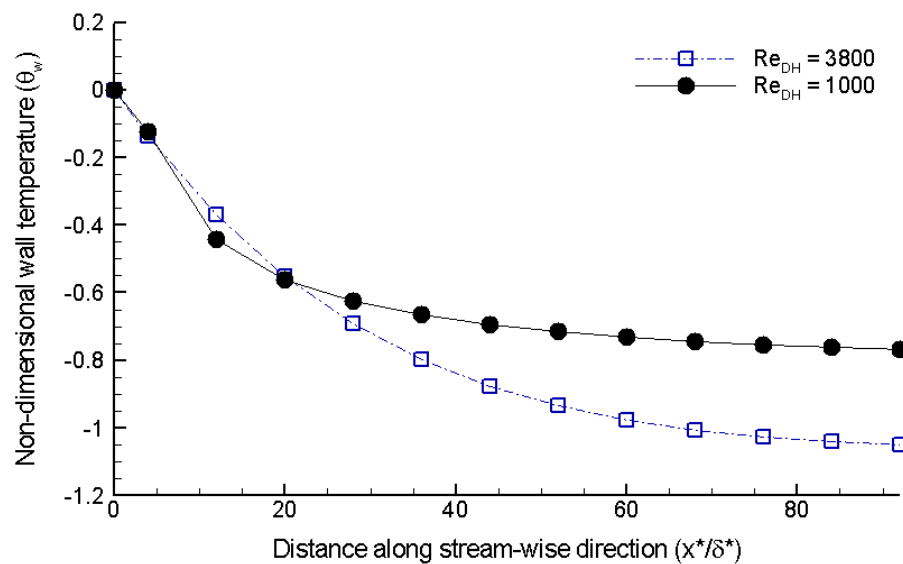


Figure 5-9 Wall temperature distribution used in the calculations

It is established in Section 5.5.2 that for the high temperature gradients existing in an EGR cooler, the process of soot deposition is similar for 10 nm and 100 nm soot particles. This independence of particle size on the deposition process is also observed in the plain channel and periodic wavy channel calculations, described in Sections 3.3.3 and 4.6.2, respectively. Hence, the following calculations are performed with only 100 nm soot particles.

Deposition

Figure 5-10 shows the normalized deposition fraction observed along the length of the channel for $Re_{DH} = 3800$ and 1000, respectively. The amount of soot depositions is observed to decrease along the length of the channel, similar to the trends exhibited in the constant wall temperature boundary condition. Likewise, the variation of the amount of soot deposition observed compares well with the variation of wall temperature gradient along the stream-wise direction. It is noted that maximum soot deposition is seen in the region between 2nd to 4th pitches, which directly corresponds to the region of largest wall temperature gradient or heat transfer.

The maximum value of deposition fraction for $Re_{DH} = 1000$ is noted to be more than twice the corresponding value for $Re_{DH} = 3800$. This difference is in line with the deposition behavior observed in the periodic wavy channel geometry, described in Section 4.6.4.

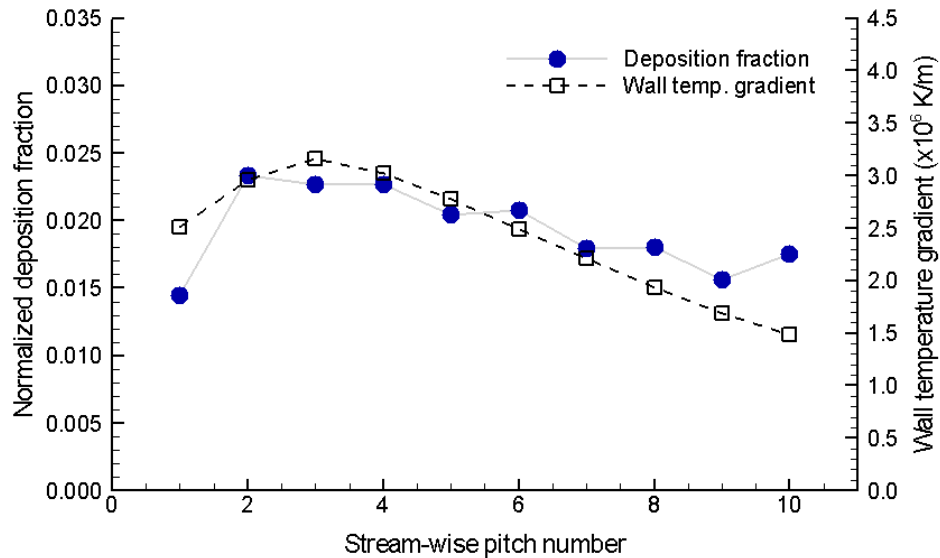


Figure 5-10 Normalized deposition fraction for 100 nm soot particles along the developing channel with varying wall temperature distribution at $Re_{DH} = 3800$

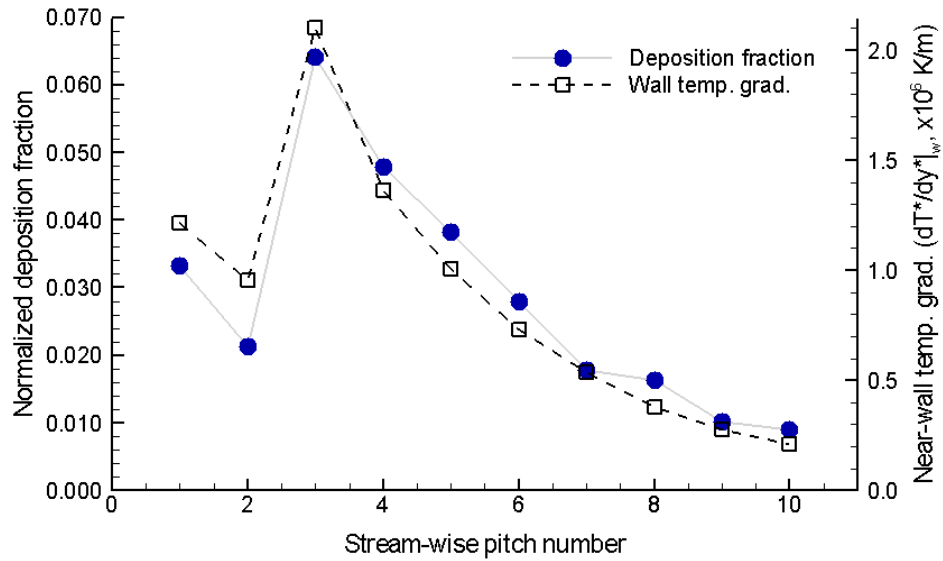


Figure 5-11 Normalized deposition fraction for 100 nm soot particles along the developing channel with varying wall temperature distribution at $Re_{DH} = 1000$

Preferential deposition

To study the occurrence of preferential deposition in certain regions, soot deposition patterns are studied on the top and bottom walls separately by super-imposing the observed depositions onto a single stream-wise pitch. For $Re_{DH} = 3800$, the first two pitches and for $Re_{DH} = 1000$, the depositions occurring in the first three pitches are excluded since the flow is not fully-developed in this region. In Figure 5-12, the super-imposed depositions on the top and bottom walls are provided for $Re_{DH} = 3800$ and 1000 respectively. Again, higher deposition is observed in the regions on the top and bottom walls where higher temperature gradients exist.

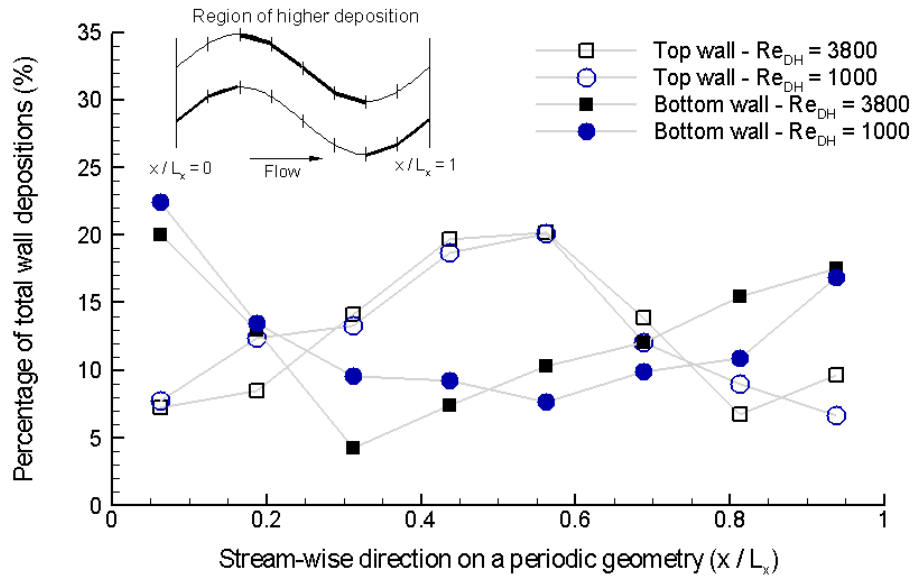


Figure 5-12 Percentage deposition observed on the top and bottom walls super-imposed onto a single stream-wise pitch for $Re_{DH} = 3800$ and 1000

5.5.4 Effect of wall temperature gradient

To study the effect of wall temperature gradient on the soot deposition further, the results obtained from all the calculations performed for $Re_{DH} = 3800$ are super-imposed onto a single plot. Since, it is found that the deposition process is independent of soot particle size, the calculations for both the particle sizes are combined together. Figure 5-13 presents the normalized deposition fractions obtained for each stream-wise pitch against the wall temperature gradient. It is seen that the normalized deposition fraction exhibits a linear variation with the wall temperature gradient. This is in line with the observations made earlier, based on the similar trends followed by the deposition and wall temperature gradient curves.

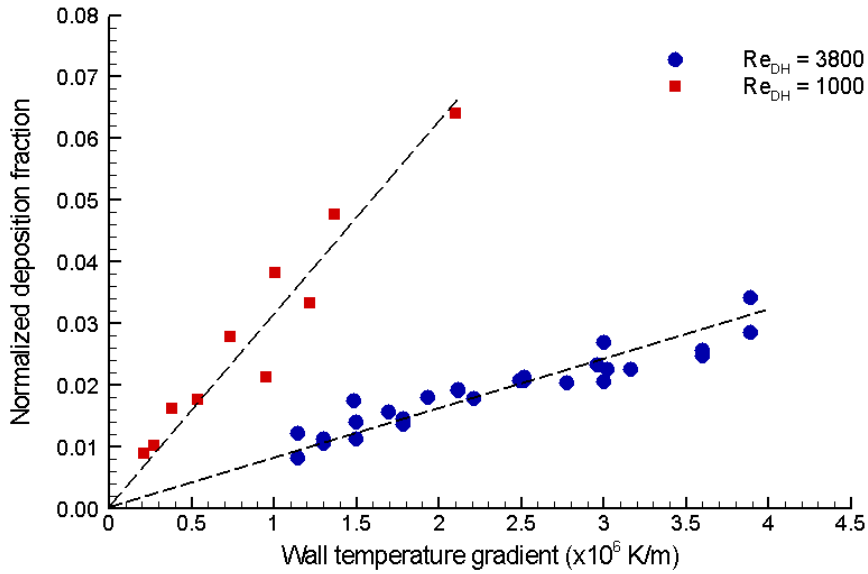


Figure 5-13 Dependence of normalized deposition fraction on the wall temperature gradient for

$$Re_{DH} = 3800$$

5.6 Summary and conclusions

Calculations are performed to simulate a developing EGR cooler flow, consisting of ten streamwise pitches. Two representative flow Reynolds numbers – 1000 and 3800 are considered. The characteristics of the flow in the entrance region and the transition to turbulence are analyzed. The flow features of the fully developed flow that exists in most of the EGR cooler length are studied. Soot deposition calculations are performed for two thermal boundary conditions – constant wall temperature and a spatially varying wall temperature profiles and the observed trends are studied. The major conclusions for this study are outlined below:

1. The flow becomes fully developed by the end of 2nd pitch for $Re_{DH} = 3800$ and 3rd pitch for $Re_{DH} = 1000$. The wavy nature of the walls results in flow destabilization, subsequently leading to turbulence.

2. Soot particles of both particle sizes – 10 nm and 100 nm exhibit similar deposition characteristics, indicating the independence of particle size on the process of deposition in the presence of high temperature gradients.
3. The amount of soot deposition decreases along the stream-wise direction for both the Reynolds numbers. This is a consequence of the decreasing thermophoretic force in the stream-wise direction caused by the cooling of the exhaust gas.
4. Soot deposition occurs preferentially in certain regions of the walls. These correspond to the regions of higher heat transfer or wall temperature gradient.
5. The normalized deposition fraction, calculated for a sampling length of each wave shows a linear relationship with the average wall temperature gradient or the average heat flux at the walls. This underlines the importance of thermophoresis as the dominant deposition mechanism.

Chapter 6

Prediction of EGR fouling – A post-processing step

The fouling of EGRs is a combination of two processes – (i) Soot particle deposition or dry soot fouling and (ii) Hydrocarbon condensation or wet soot fouling. The fouling layer is affected by various factors such as the temperatures of the gas and surfaces, thickness of fouling layer that may already exist and its physical properties. The present chapter presents a post-processing methodology to compute the time-dependent fouling layer thickness over the full length of the EGR coolers.

6.1 Dry soot fouling layer

Deposition of soot particulate matter present in the exhaust gas on the EGR surfaces is referred to as dry soot fouling layer. The growth of the dry soot layer in time due to deposition of soot particles is to be calculated. Results obtained from the particle deposition calculations presented in the previous chapters are used for this purpose. Deposition correlations for deposition fractions η_{dep} against heat flux at the walls are used to determine the amount of deposit onto the EGR surface. In Figure 6-1, the calculated normalized deposition fractions are plotted with the corresponding heat flux values at the walls for two Reynolds numbers. It is observed that the amount of deposition decreases with a decrease in the heat flux at the walls. The deposition fractions presented are normalized with the number of particles entering a periodic unit and are calculated as:

$$\eta_{dep} = \frac{\text{Number of particle depositions}}{\text{Number of particles entering the periodic unit}} \quad 6.1$$

The deposition curves are approximated by linear correlations, so that the values of deposition fractions can be extrapolated for lower values of wall heat flux, which typically exist in the downstream parts of the EGR cooler. Following are the correlations obtained for the two Reynolds numbers for which calculations are performed.

For $Re_{D_H} = 1000$,

$$\eta_{dep} = 1.0724 \times 10^{-6} \cdot q_w^* + 1.6767 \times 10^{-2} \quad 6.2$$

For $Re_{D_H} = 3800$,

$$\eta_{dep} = 6.6456 \times 10^{-8} \cdot q_w^* + 1.1421 \times 10^{-2} \quad 6.3$$

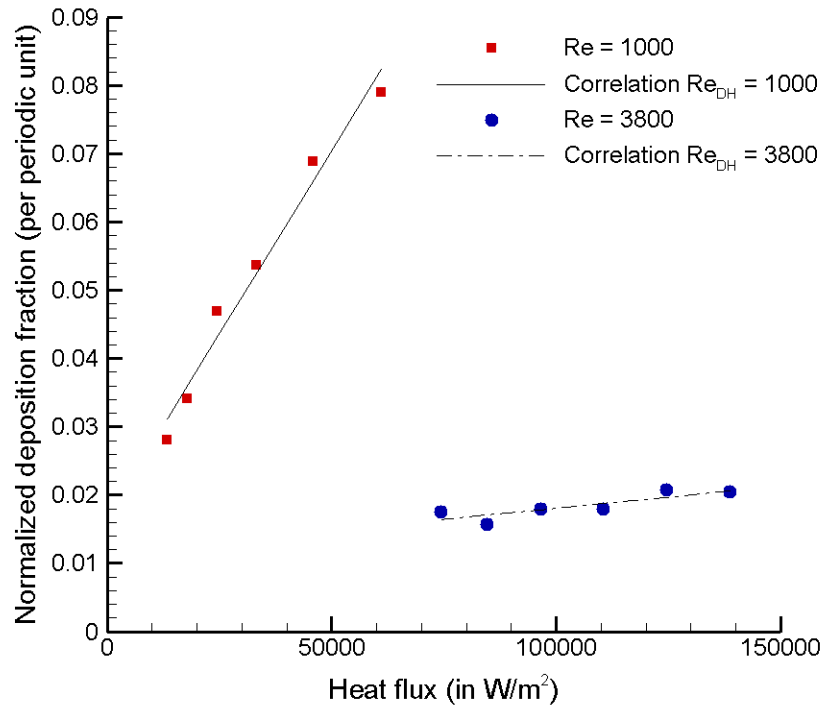


Figure 6-1 Normalized deposition fractions for different heat flux values obtained from the developing flow calculations and the corresponding linear correlations for $Re_{D_H} = 3800$ and 1000

The deposition correlations provided in Eq. 6.2 and Eq. 6.3 are applicable over a considerably wide range of heat flux values. Most of the heat transfer from the exhaust gas takes place in the initial parts of the EGR cooler where the heat flux values are in the range for which the deposition calculations have been carried out and shown in Figure 6-1. However, below a certain minimum value of heat flux, the deposition observed would be negligibly small and the deposition fraction for these values of heat flux can be taken as 0. To determine this lower threshold value of heat flux, the thermophoretic velocity of a

particle is calculated based on the near-wall temperature gradient. The process of deposition of soot particles is assumed to happen if the time taken for the particles to reach the wall, computed based on the thermophoretic velocity is less than the time taken for particles to flow out of the EGR cooler, computed based on the mean flow velocity. Otherwise, the soot particles are assumed not to deposit and hence the deposition fraction is set to zero.

If \dot{m}_{in_p} is the rate of particulate mass entering the periodic domain, then the fouling layer thickness due to soot particle deposition is given by:

$$\delta_f^{*} = \frac{\dot{m}_{in_p}^* \cdot \eta_{dep} \cdot \Delta t^*}{\rho_{dep}^* \cdot A_s^*} \quad 6.4$$

6.2 Wet soot fouling layer

Along with particulate matter, the exhaust gases entering the EGR coolers are also contains various chemical species. The chemical species include oxides of carbon, nitrogen, sulfur, water vapor and a range of hydrocarbons among others. Of the hydrocarbon species present, the heavy compounds are 2-methylpentacosane ($C_{25}H_{52}$), n-hexacosane ($C_{26}H_{54}$) and n-heptacosane ($C_{27}H_{56}$). Wet soot layer formation occurs mainly due to condensation of these heavy hydrocarbons on the EGR surfaces. Condensation is the change of state of a given substance from gaseous phase to liquid phase. Occurrence of the process of condensation is dependent on the variation of saturation pressure with saturation temperature. The methodology for computation of the amount of hydrocarbon condensation is provided below.

6.2.1 Mole fraction and saturated mole fraction

Initial values for the amounts of hydrocarbons are obtained from the percentage composition of emission from a standard heavy-duty diesel exhaust. Usually, the amounts of various species in diesel exhaust are expressed as volume fractions. It is noted that for ideal mixtures, the mole fraction values are

equal to the corresponding volume fraction values. Using the mole fraction value, the partial pressure of each species in the flow field is computed as:

$$P_i^* = y_i \times P_{total}^* \quad 6.5$$

The amount of condensate formed is dependent on the saturation pressure of the gaseous species at the given temperature. Further, a specified value of saturation pressure means that the maximum mole fraction (or the saturated mole fraction) of the species that can be present in the gaseous phase is fixed at that temperature and is given by:

$$y_{sat} = \frac{P_{sat}^*}{P_{total}^*} \quad 6.6$$

6.2.2 Relationship of saturation pressure and saturation temperature

Experimental studies have been undertaken in the past by Stull [21] to determine the variation of saturation temperature T_{sat}^* and pressure P_{sat}^* for various hydrocarbons, including the ones commonly found in heavy-duty diesel exhaust. A general method to find a correlation relating P_{sat}^* with T_{sat}^* is described in Campanella [22]. In Figure 6-2, the saturation pressure is plotted on the y-axis on a log scale against $1000/T_{sat}^*$ on the x-axis. With this choice of abscissa and ordinate, it is seen that the relationship between T_{sat}^* and P_{sat}^* for each of the three hydrocarbons exhibits a linear behavior. Also, the values of T_{sat}^* corresponding to a given value of P_{sat}^* show a variation of less than 4% for the three species and this aspect can also be qualitatively observed in Figure 6-2. Thus, instead of studying the effects of condensation of the three different species, it is valid to consider the effects of condensation of a single species. Hence, condensation and its effects on EGR cooler is studied by considering the presence of a single heavy hydrocarbon species – n-hexacosane. For n-hexacosane, the variation of saturation pressure with temperature as obtained from the plot can be expressed as:

$$\log_{10} P_{sat}^* = -\frac{4719.34}{T_{sat}^*} + 12.025 \quad 6.7$$

$$P_{sat}^* = 10^{-\frac{4719.34}{T_{sat}^*} + 12.025} \quad 6.8$$

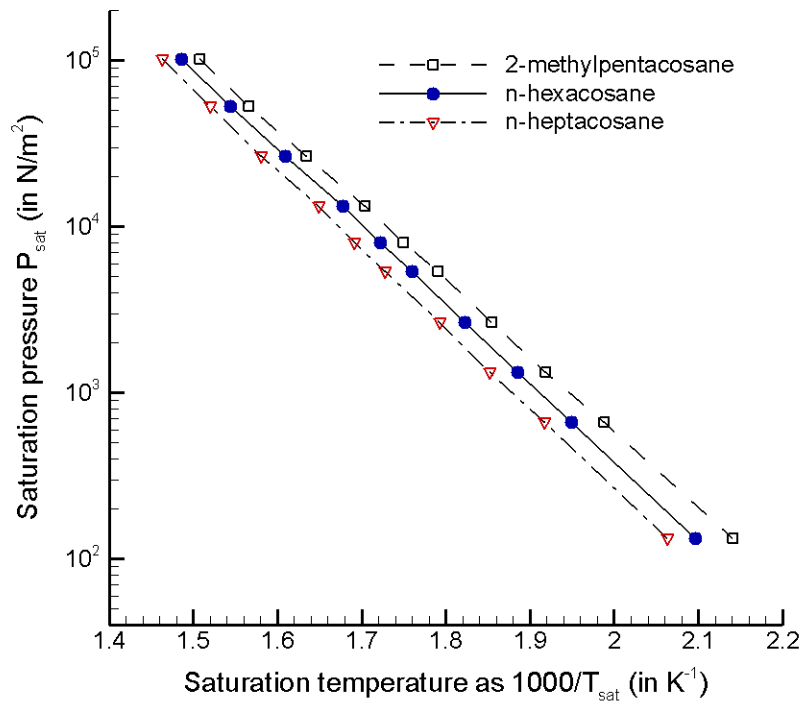


Figure 6-2 Relationship of saturation pressure with saturation temperatures for 2-methylpentacosane, n-hexacosane and n-heptacosane

6.2.3 Hydrocarbon condensation

This section describes the general methodology used to compute the amount of condensation of hydrocarbons. These computations are performed as a post-processing step after the fluid and thermal fields are obtained from the calculations. The following assumptions are made:

1. Ideal gas assumptions hold for the mixture and all its components.
2. Mass diffusion of species due to concentration gradients is negligible.
3. Transport and re-evaporation of condensed mass is not considered.

- Physical properties like density and thermal conductivity of the condensed mass is assumed to be the same, irrespective of the temperature at which condensation takes place. Since the pressure drop in the EGR cooler is small compared to the total pressure of 3 atm., the temperature range over which condensation occurs is also small making this a valid assumption.

The methodology for computing hydrocarbon condensation is provided below:

- For each periodic unit, saturation pressure P_{sat} corresponding to its temperature is computed using Eq 6.8.
- The saturated mole fraction y_{sat} is computed using the calculated P_{sat}^* value using Eq 6.6.
- Condensation would happen if the mole fraction of the species y_i in the gas is higher than the saturation mole fraction y_{sat} . The mole fraction of the species after condensation would then be equal to y_{sat} . The total amount of condensed mass in a time interval Δt^* is given by:

$$m_{cond}^* = \rho_{sp}^* \cdot (y_i - y_{sat}) \cdot A_c^* \cdot u_m^* \cdot \Delta t^* \quad 6.9$$

Here, A_c^* is the cross-sectional area of the periodic unit. The above equation uses the fact that for ideal mixtures, mole fraction values are same as the corresponding volume fraction values. Since transport of condensed mass is not considered, it is assumed to deposit at the same x-location.

- The procedure is repeated for the entire computational domain, proceeding in the stream-wise direction.

The fouling layer thickness due to the condensed hydrocarbon mass on the EGR surface would then be given by:

$$\delta_{f wet}^* = \frac{m_{cond}^*}{\rho_{cond}^* \cdot A_s^*} \quad 6.10$$

6.3 Fouling layer removal

A simple model for the removal of deposited fouling layer from the EGR cooler surfaces is used.

Teng [25] studied the nature of EGR fouling layers and noted that the soot deposit is usually considered

to be made up of three layers: a dense base layer, a medium intermediate layer and a loose surface layer. The removal process occurs due to erosion of the top layer of the deposit. It is noted that this happens mainly due to the momentum of the flowing exhaust gas eroding the porous top layer. The mass rate of deposit removal is hence given by:

$$\dot{m}_{rem}^* = C \cdot (\rho^* \cdot U_m^{*2}) \cdot \delta_f^* \quad 6.11$$

Since much information is not available on the removal of soot deposits, the above mentioned model is a very simplistic approach to model the removal process. The constant C used in Eq. 6.11 is a removal constant that is determined based on the available data of soot particle deposits found in EGR coolers. The removal process is applied to both dry and wet soot deposit layers. The removal constants however, would be different for the two layers due to their different physical properties.

6.4 Post-processing methodology

6.4.1 Geometry and notations

An EGR cooler consists of a periodically repeating geometry in the stream-wise direction. Calculations are performed on the entire EGR cooler and for a certain time of operation. The spatial distribution and growth of the fouling layer in time is of primary interest. Figure 6-3 shows a representative sketch of two periodic units used for the fouling layer prediction. Due to the presence of the fouling layer, the temperature of the wall at the outer surface, denoted by T_w^* would be different from the temperature at the inner surface which is in contact with the flowing exhaust gas and is denoted by T_f^* . The fluid enters the periodic unit at temperature $T_{m,in}^*$ and exits at temperature $T_{m,out}^*$. An energy balance is applied at the boundary which includes the fouling layer and the outer wall. The heat transfer due to convection from the hot exhaust gas to the inner surface of fouling layer is hence equal to the heat transfer by conduction through the fouling layer to the outer wall.

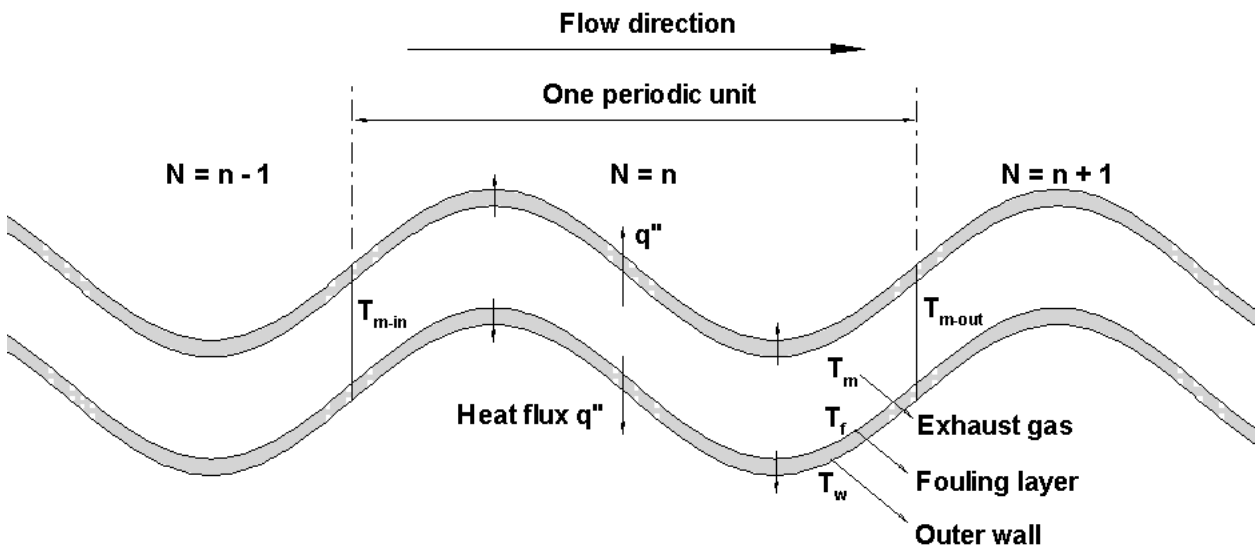


Figure 6-3 Representative sketch of the geometry for fouling layer prediction

6.4.2 Assumptions

Apart from the assumptions used for species condensation, the post-processing calculations are based on certain assumptions and are listed below.

1. The heat transfer coefficient remains constant irrespective of the change in geometry due to the fouling layer growth. A mean value of the heat transfer coefficient computed from the average Nusselt number is used for this purpose.
2. The physical processes involved are considered to be quasi-steady.
3. The outer surface temperature, referred to as wall temperature, is assumed to remain constant and not vary with time. Only the fluid mean temperature and inner surface temperature, called fouling layer temperature varies in time.
4. Thermal conductivity of both dry and wet soot layers is a constant and does not vary with the thickness of the fouling layer.

6.4.3 Methodology

The method of computing fouling layer thickness due to deposition of soot particles and condensation of heavy hydrocarbons is explained in the previous section. Here, the step-by-step methodology to predict the growth of fouling layer in space and time is presented.

1. Calculate heat flux q_w^* for the periodic unit, based on heat transfer coefficient h^* , mean exhaust gas temperature T_m^* and fouling layer temperature T_f^* .

$$q_w^* = h^* \cdot (T_m^* - T_f^*) \quad 6.12$$

2. Deposition correlations for normalized deposition fractions η_{dep} against heat flux at the walls are used to determine the thickness of deposit $\delta_{f_{dry}}^*$ (refer section 6.1).
3. Thickness of the hydrocarbon condensation deposit $\delta_{f_{wet}}^*$ that would be formed based on the pressure and temperature values is computed (refer section 6.2).
4. The total fouling layer thickness is then given by the summation of the dry and wet soot layers.

$$\delta_f^* = \delta_{f_{dry}}^* + \delta_{f_{wet}}^* \quad 6.13$$

5. In the EGR cooler, heat transfer by conduction from the inner surface to the outer surface should be the same as the heat transfer from the exhaust gases to the inner surface. The fouling layer temperature T_f^* is then calculated as:

$$T_f^* = T_w^* + q_w^* \cdot \frac{\delta_f^*}{\kappa_f^*} \quad 6.14$$

6. Since, heat is being removed from the exhaust gases, the mean temperature of gas at the exit of a periodic unit can be computed by using a basic energy balance. Finally, the new mean temperature of the gas would be computed as:

$$T_{m_{out}}^* = T_{m_{in}}^* - \frac{q_w^* \cdot A_f^*}{\dot{m}_{in_f}^* \cdot C_p^*} \quad 6.15$$

$$T_m^* = \frac{T_{m_{in}}^* + T_{m_{out}}^*}{2} \quad \text{6.16}$$

Each of the above mentioned equations 6.12-6.16 are solved to advance the solution for one time-step Δt^* . Several of these time-steps are performed to compute the thickness of the fouling layer at the end of a specified time of operation of the EGR cooler. Further, the procedure is repeated each periodic unit sweeping in the stream-wise direction.

6.5 Results and discussion

This section presents results obtained from the post-processing methodology. Since the particle deposition correlations are to be used in the model, the calculations are performed for two Reynolds numbers cases, for which particle deposition simulations have been carried out. Table 6.1 lists the properties of exhaust gas, particles and hydrocarbon species used in the calculations. Later, the growth of the two fouling layers computed from the methodology is discussed in detail.

Table 6.1 Exhaust gas, particle properties and flow parameters used in the calculations

Gas properties	
Kinematic viscosity (m^2/s)	1.9×10^{-5}
Thermal conductivity (W/m-K)	0.042295
Density (kg/m^3)	2.9083
Specific heat (J/kg-K)	1070
Specific gas constant (J/kg-K)	287.0
Particle properties (carbon)	
Diameter (nm)	100
Density (kg/m^3)	2000
Thermal conductivity (W/m-K)	129.0

Species properties (n-hexacosane)		
Molecular weight	366.72	
Density – Liquid state (kg/m ³)	800.0	
Density – Vapor state (kg/m ³)	Computed from ideal gas law at and inlet pressure and 423K	
Fouling layer properties		
Thermal conductivity (W/m-K) (nominal)	0.1	
Geometric and Flow properties		
Number of periodic units	40	
Inlet gas temperature (K)	873	
Wall temperature (K)	Specified wall temperature till 10 th periodic unit 373 from 10 th periodic unit till exit	
Inlet pressure (Pa)	3.0×10 ⁵	
Initial particulate mass concentration (%)	0.006	
Initial species concentration (ppm) (nominal)	15	
Reynolds number (based on D_H^*)	1000	3800
Nusselt number (based on D_H^*)	21.98	43.98
Removal constant – Dry soot	7.0×10 ⁻⁹	9×10 ⁻¹⁰
Removal constant – Wet soot	2.0×10 ⁻¹⁰	1.0×10 ⁻¹¹

Dry soot fouling occurring due to soot particle deposition is dependent on the heat flux at the EGR cooler surfaces as given by Eq. 6.2 and Eq. 6.3. On the other hand, the amount of wet soot fouling occurring due to hydrocarbon condensation depends on the variation of temperature of the exhaust gas along the length of the EGR cooler and the amount of species mole fraction it can hold at that temperature. However, it is important to note that the amount of heat transfer is dependent on thickness of

the fouling layer already formed and this in turn affects the temperature of the exhaust gas along the cooler. This means that, the dry soot layer growth will depend on the thickness of fouling layer (both dry and wet soot) already existing. Likewise, the presence of a fouling layer results in changes in the exhaust gas temperatures which corresponds to changes in the nature of wet soot layer growth along the length of the EGR cooler. Thus, the growth of fouling layer over a period of time is a continuously evolving process with inter-dependencies on the existing fouling layer thicknesses, heat transfer rates and corresponding temperature profile along the EGR cooler.

6.5.1 Base calculations

The soot layers predicted from the computations are presented as plots giving the spatial variations for different times of operation. Each line on the plot represents the thickness of dry soot layer along the length of the EGR cooler. Each marking on the line represents the average thickness of the layer in a periodic unit. It should be noted that though the plots for dry and wet soot fouling layers are presented separately, the methodology used for computation considers the growth of both layers simultaneously. Hence, each of the calculations presented takes into account the dependencies and computes the two fouling layer thicknesses for a time-step Δt^* . The process is repeated over several such time-steps to obtain the growth over a certain period of operation.

Case 1: Reynolds number 3800

Figure 6-4 provides a plot of the spatial variation of dry soot layer at the end of different operational times. The layer thickness at the end of 400 hours of operation is noted to attain a peak around approximately the 10th wave and then the thickness reduces in the stream-wise direction. Decrease in the layer thickness is gradual, showing a reduction of approximately 10% over a length of 25 periodic units. The sudden drop in the thickness after the 35th periodic unit is attributed to the procedure used to determine the threshold minimum heat flux for which the deposition correlation is applicable.

Initially, it is observed that the layer thickness increases as the operation time increases. However, the rate of growth of the layer reduces significantly after approximately 70 hours of operation. The decrease in the growth rate is attributed to two factors – (i) reduced heat transfer rate and (ii) increased removal rate. Reduced heat transfer in the cooler is due to the presence of the fouling layer itself. As established by the particle deposition studies, a reduced heat transfer rate at the walls results in lesser particle deposition and hence reduces the rate of growth of the dry soot layer. Also, with the presence of a thicker fouling layer, the removal rate also increases and hence, this increase in the process of removal contributes to the reduction in the growth of the layer thickness. Thus, the combination of reduced heat transfer rate and the fouling layer removal results in the stabilization of the dry soot layer after certain operation hours.

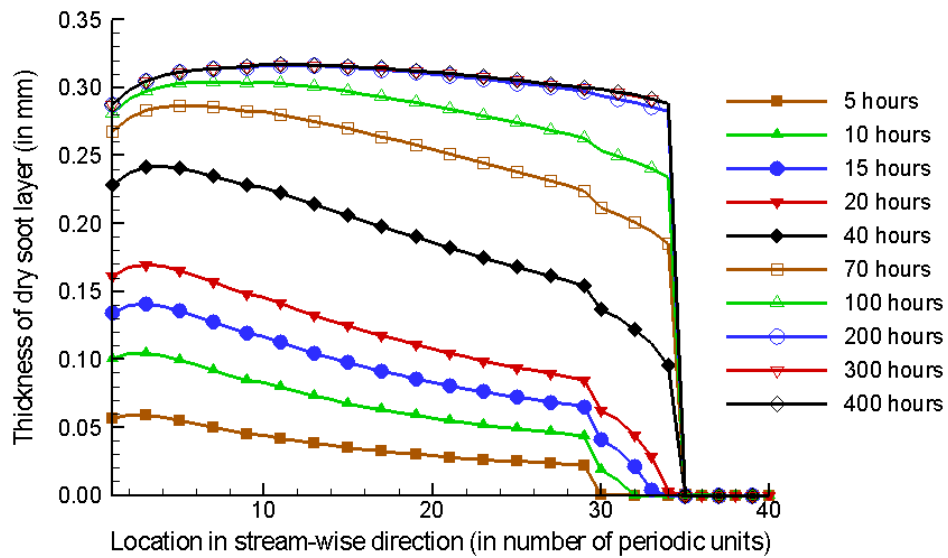


Figure 6-4 Thickness of dry soot layer on the EGR cooler surface for $Re_{D_H} = 3800$ for various hours of operation

The wet soot layer growth is provided in Figure 6-5. It is noted that condensation of hydrocarbons is not observed in the initial parts of the EGR cooler. The condensation layer starts building up from

approximately the 28th periodic unit. The thickness of the layer increases continuously till the end of the cooler. The growth in time however, is different from the behavior observed for dry soot layer. Most of the fouling due to condensation occurs in the few initial hours of operation, approximately in the range of the first 5 hours after which the layer starts decreasing slowly over time. The process of condensation is dependent on the partial pressure of the hydrocarbon species and the corresponding saturation temperature at that pressure. The variation of partial pressure of the hydrocarbon along the length of the cooler is less than 1%. The corresponding value of saturation temperature is around 415 K with a variation of less than 0.03% along the length of the cooler. Even for the three heavy hydrocarbon species prominently found in heavy-duty diesel exhaust, the saturation temperature value is approximately in the range of 405 K to 422 K. Due to the fouling of the EGR cooler surface due to the dry and wet soot layers, the net heat transfer from the gas reduces. This reduction in heat transfer rate results in an increase in the mean temperature of the gas through the cooler and correspondingly a decrease in condensation. After the initial 20 hours of operation, the temperature of the gas is more than 415K through the length of the channel and hence no condensation is observed after this time. The removal of the wet soot layer takes place continuously and hence the thickness of the wet soot layer decreases as the cooler is operated for longer durations. The presence of wet soot layer however is towards the end, whereas most of the heat transfer takes place in the initial parts of the EGR cooler.

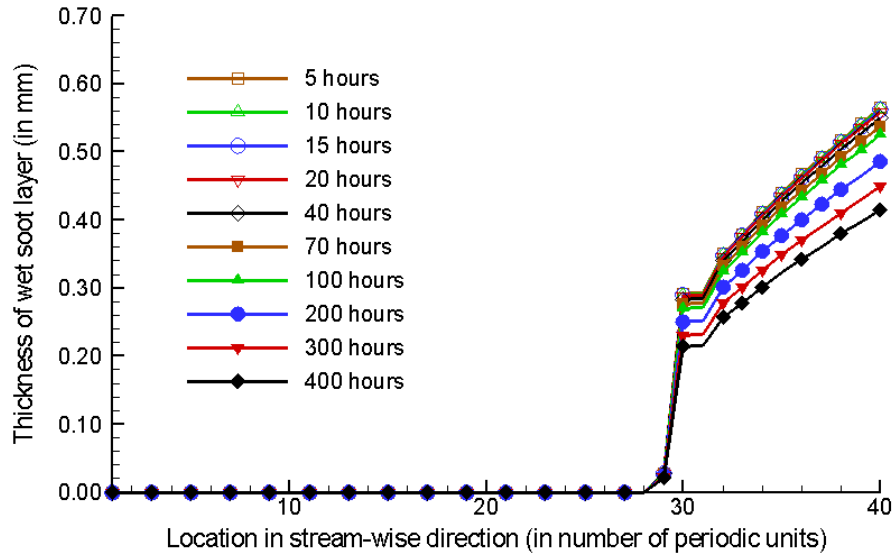


Figure 6-5 Thickness of wet soot layer on the EGR cooler surface for $Re_{DH} = 3800$ at various hours of operation

Case 2: Reynolds number 1000

The plots of thicknesses obtained for dry and wet soot layers for $Re_{DH} = 1000$ case are presented in Figure 6-6 and Figure 6-7. The observed behavior of the growth of dry and wet soot layers are qualitatively similar to those observed for $Re_{DH} = 3800$ case. However, there are certain differences between the two cases in the trends which are discussed here.

The maximum thickness of dry soot layer is observed around the 4th periodic unit. The drop in the thickness however, is steep compared to the $Re_{DH} = 3800$ case. This behavior is attributed to the variation of deposition fraction with heat flux for the two Reynolds number cases. The $Re_{DH} = 1000$ case shows a much higher sensitivity to change in heat flux. Since the dry soot deposition is related to the heat flux as given by the correlations Eqns. 6.2 and 6.3, the layer thickness predicted shows a correspondingly steeper trend for the $Re_{DH} = 1000$ case. The dry soot layer stabilization occurs after approximately 100 hours of operation.

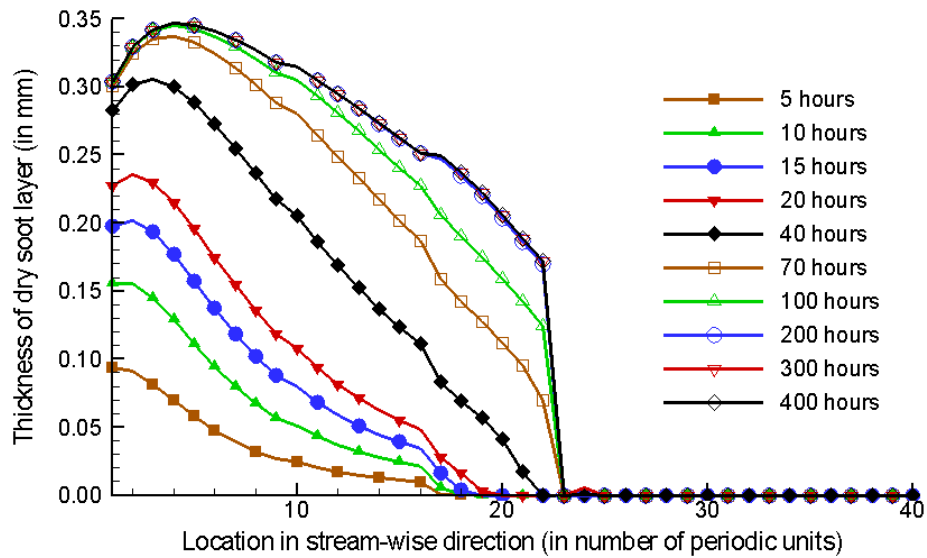


Figure 6-6 Thickness of dry soot layer on the EGR cooler surface for $Re_{H} = 1000$ after various operational hours

The wet soot layer, again, is not found in the initial parts of the EGR cooler. The layer starts developing from approximately the 16th periodic unit and its thickness increases in the downstream direction. The peak value in the wet soot layer initially occurs around the 20th periodic unit, but gradually shifts downstream as the operation time increases. This behavior is due to the variation of temperature field inside the EGR cooler. When the fouling in EGR cooler is less, the gas is cooled below the saturation temperature value of 415K. The peak in the condensation fouling is observed in the region where the temperature of the gas is around this value. As the fouling on the cooler walls increases, the heat transfer rate reduces and the gas attains 415K temperature further downstream. Hence, as the cooler operation time increases, the peak in the condensation layer shifts downstream. The thickness of the wet soot layer is the largest after approximately 70 hours of operation after which the layer thickness starts decreasing due to removal. The gas is not cooled down below its saturation temperature and the removal takes place continuously, thus decreasing the layer thickness.

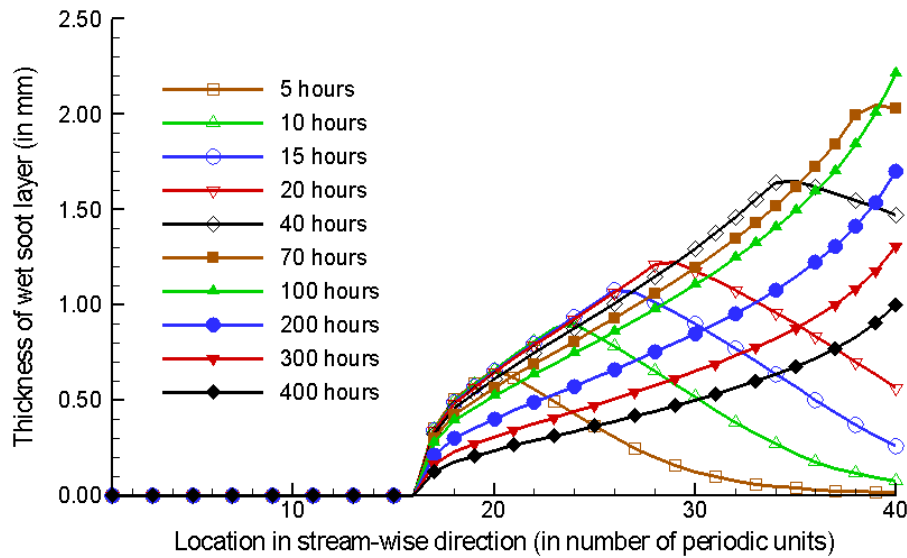


Figure 6-7 Thickness of wet soot layer on the EGR cooler surface for $Re_{D_H} = 1000$ after various operational hours

6.5.2 Parametric studies

The growth of both dry soot and wet soot fouling layers on EGR cooler surfaces is a complex phenomenon and is dependent on various factors. The parameters which show relatively high sensitivity to the fouling layer thickness are thermal conductivity of the gas and thermal conductivity of the fouling layer. Change in values of these properties results in a change in values of fouling layer thicknesses, exhaust gas temperature and cooler effectiveness, which are all related to each other. Therefore, parametric studies are done to study the effect of these parameters on the fouling layer thickness in particular and are presented here.

Thermal conductivity of the exhaust gas

The effect of thermal conductivity of the exhaust gas on the fouling layer growth is studied. Calculations are performed for three values of thermal conductivity (κ_g^*) and the predicted dry and wet soot thicknesses are plotted in Figure 6-8 and Figure 6-9 respectively. The thickness values are after 5

hours of operation of the cooler. It is observed that the layer thickness increases with increase in the value of κ_g^* . The dry soot thickness increases only slightly and this is due to the increase in heat transfer coefficient corresponding to the increase in κ_g^* . The wet soot layer, however, shows a greater sensitivity to the change in κ_g^* . The higher heat transfer results in exhaust gas attaining lower temperatures much earlier in the cooler than when the heat transfer rates are lower. Thus, the thickness plots start developing much earlier (by around 23rd periodic unit) when the value of κ_g^* is increased.

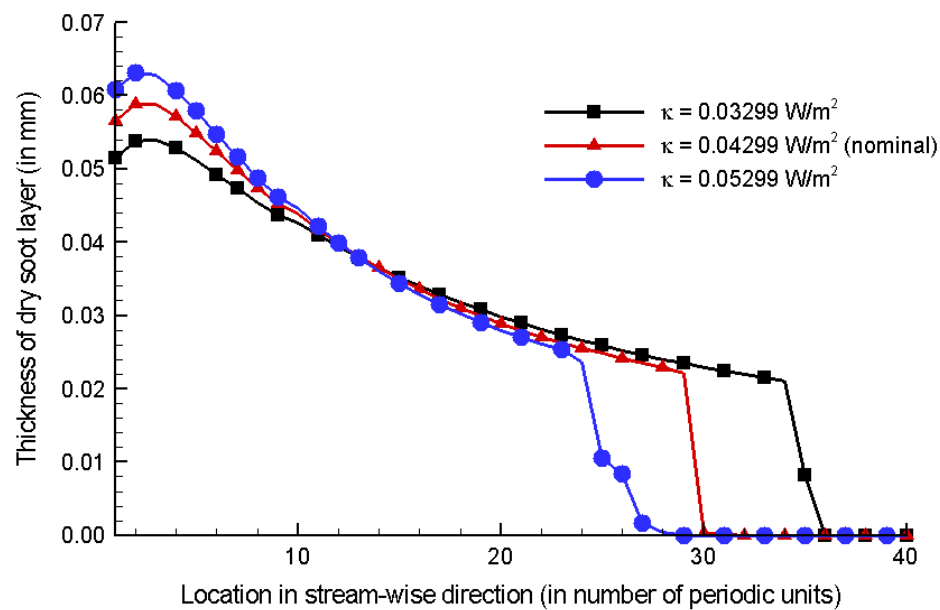


Figure 6-8 Dry soot thickness after 5 hours of operation of the EGR cooler predicted for different values of thermal conductivity of exhaust gas for $\text{Re}_{D_H} = 3800$

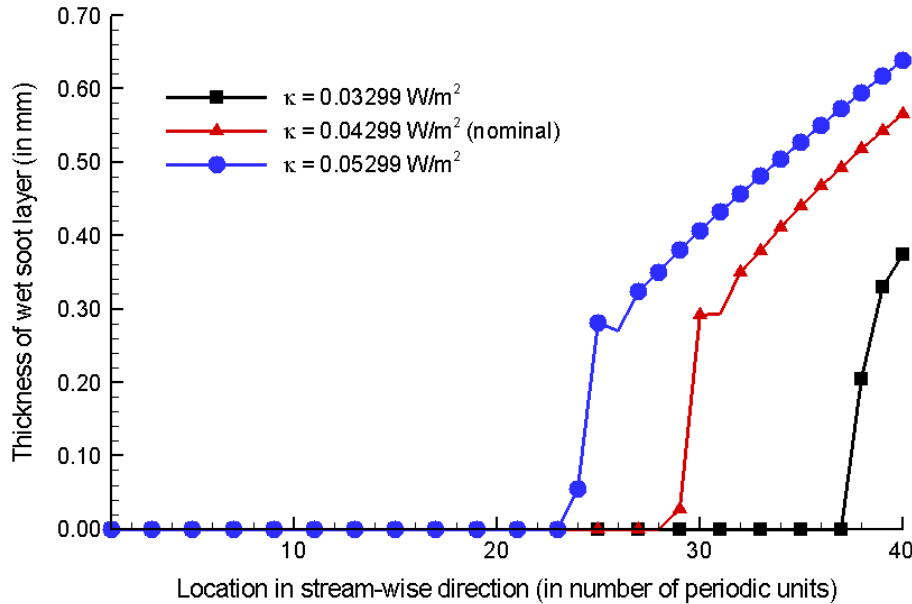


Figure 6-9 Wet soot thickness after 5 hours of operation of the EGR cooler predicted for different values of thermal conductivity of exhaust gas for $\text{Re}_{D_H} = 3800$

Thermal conductivity of the fouling layer

Computations are performed with various values of the thermal conductivity of the fouling layer κ_f^* . Figure 6-10 and Figure 6-11 show the variation of thickness of dry and wet soot layers respectively after 5 hours of operation for various values of κ_f^* . It is observed in Figure 6-10 that dry soot layer thickness increases only slightly with an increase in κ_f^* . The difference in thickness increases as the cooler is operated for longer durations. The increase is due to the increased heat transfer rates resulting from the higher κ_f^* value. Similarly, the wet soot layer also exhibits an increase in the $\delta_{f,wet}^*$ value with increase in κ_f^* and is shown in Figure 6-11. The higher heat transfer in the upstream section of the cooler causes the temperature of the exhaust gas to cool below the saturation temperature, resulting in more condensation. The increase in wet soot layer thickness due to an increase in κ_f^* is higher than the increase in dry soot layer indicating that the sensitivity of wet soot formation to κ_f^* is higher.

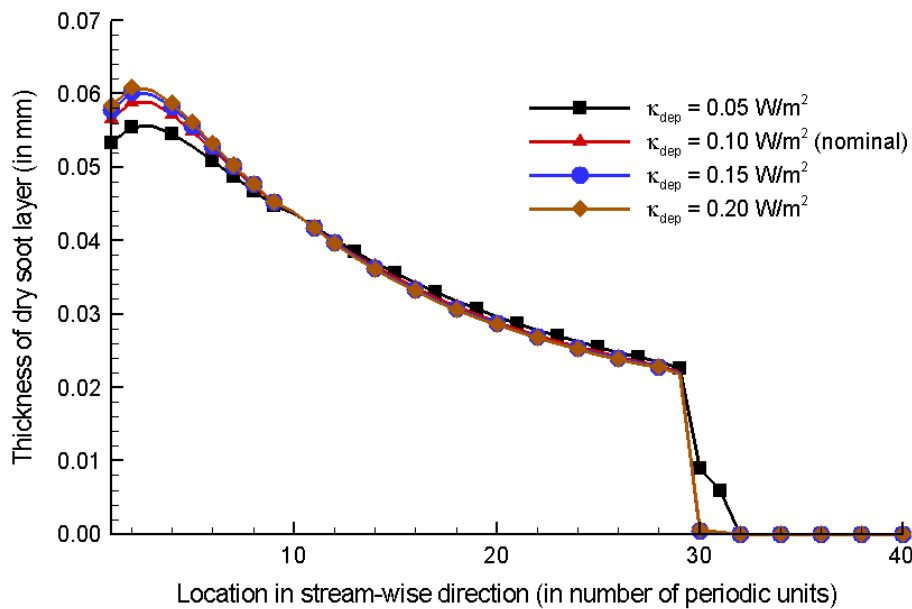


Figure 6-10 Dry soot thickness after 5 hours of operation of the EGR cooler predicted for different values of thermal conductivity of fouling layer for $Re_{D_H} = 3800$

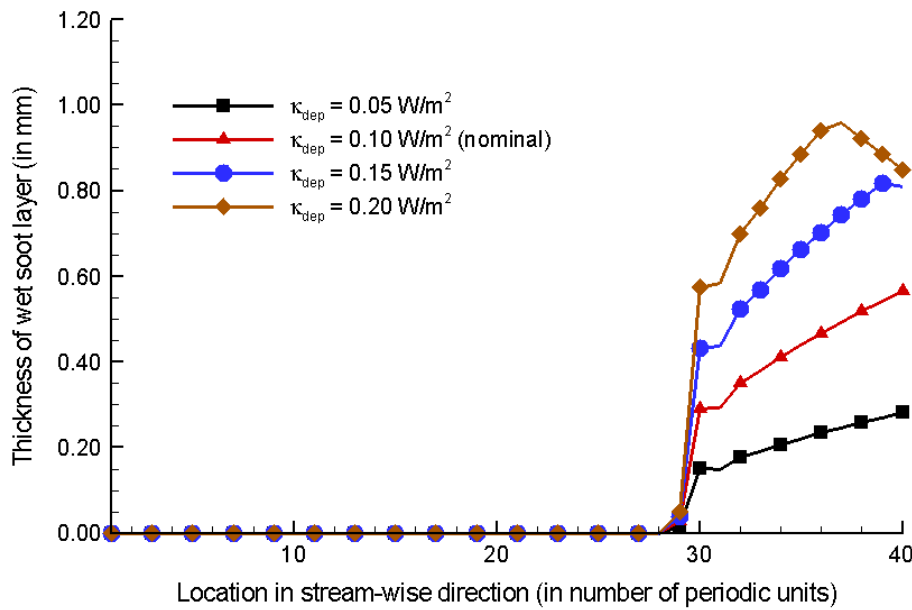


Figure 6-11 Wet soot thickness after 5 hours of operation of the EGR cooler predicted for different values of thermal conductivity of fouling layer for $Re_{D_H} = 3800$

Inlet exhaust gas temperature

The total heat transfer from the exhaust gas to the walls of the EGR cooler is dependent on the inlet temperature of the exhaust gas. Calculations are performed for different inlet exhaust gas temperatures for the same wall temperature distribution. The fouling layer thicknesses observed after 5 hours of operation are presented in Figure 6-12 and Figure 6-13. It is seen that with an increase in the inlet temperature, the dry soot layer thickness increases. This is due to the increased heat transfer occurring due to a higher temperature difference between the gas and the walls.

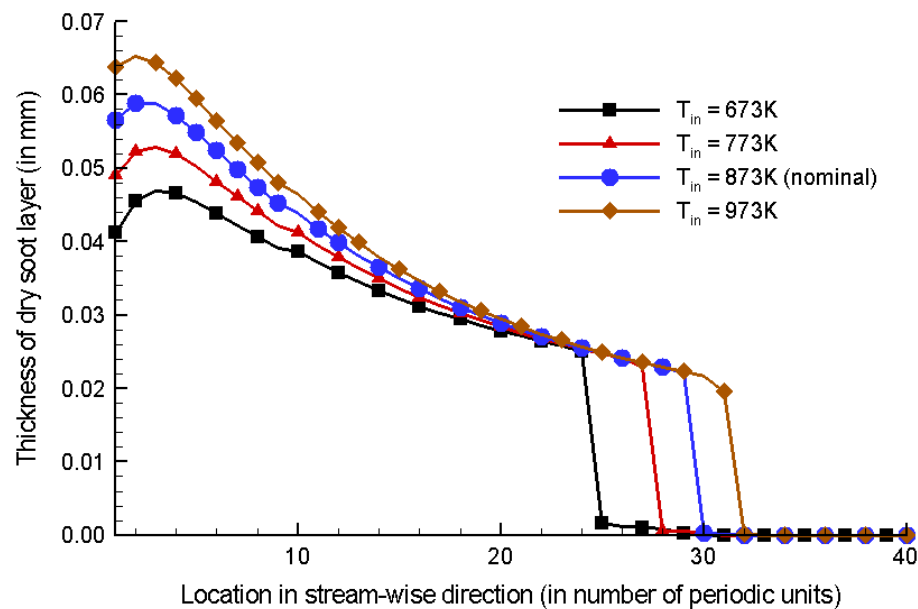


Figure 6-12 Dry soot thickness after 5 hours of operation of the EGR cooler predicted for different values of inlet gas temperatures of hydrocarbon species of fouling layer for $\text{Re}_{D_H} = 3800$

The wet soot layer exhibits an opposite trend, with the layer thickness decreasing with an increase in inlet temperature of the exhaust gas. The layer build-up also is observed to shift downstream with increase in inlet temperature. The reason for these trends again is the increased heat transfer rate in the initial parts of the EGR cooler. With the increase in inlet temperature, the cooling of gas temperature below the saturation temperature occurs further downstream, resulting in the shifting of the wet soot

layer. The relatively higher temperatures of the exhaust gas in the downstream parts of the cooler, thus also leading to lesser wet soot layer formation.

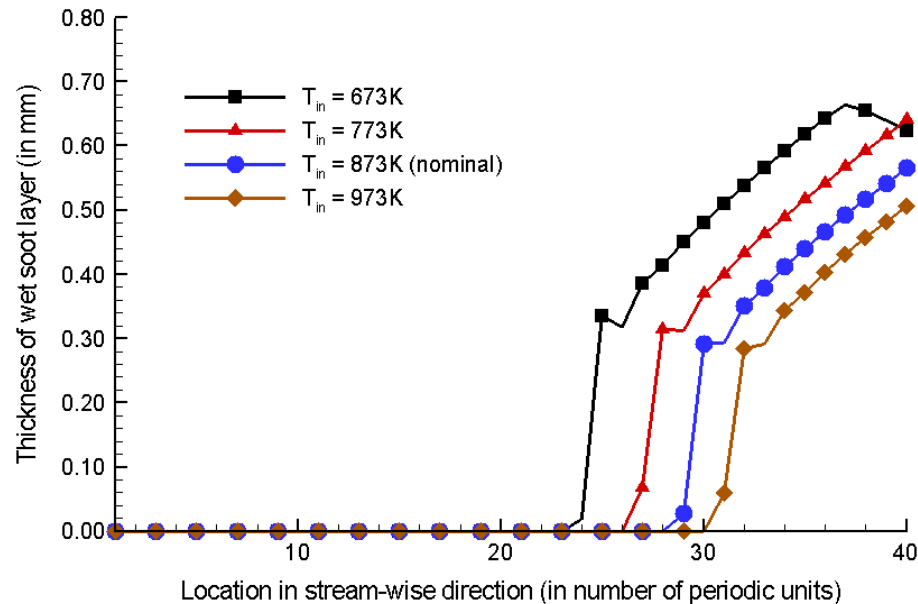


Figure 6-13 Wet soot thickness after 5 hours of operation of the EGR cooler predicted for different values of inlet gas temperatures of hydrocarbon species of fouling layer for $\text{Re}_{D_H} = 3800$

Initial concentration of hydrocarbon species

The nature of fouling layers formed for different values of initial concentration of hydrocarbon species entering the EGR cooler is studied. Figure 6-14 and Figure 6-15 show plots of dry and wet soot layer thicknesses after 5 hours of operation respectively. The dry soot thickness shows no change with increase in the inlet concentration of hydrocarbon species, which is expected as the condensation process takes place downstream. The wet soot layer exhibits higher values of thickness with increase in the initial concentration. Though this increase is trivially expected, the corresponding behavioral trend is of importance. The condensate formation occurs in the comparatively upstream parts of the EGR cooler since for higher volume or mole fractions of hydrocarbon species, condensation takes place at slightly higher values of temperature and hence in the upstream locations of the cooler.

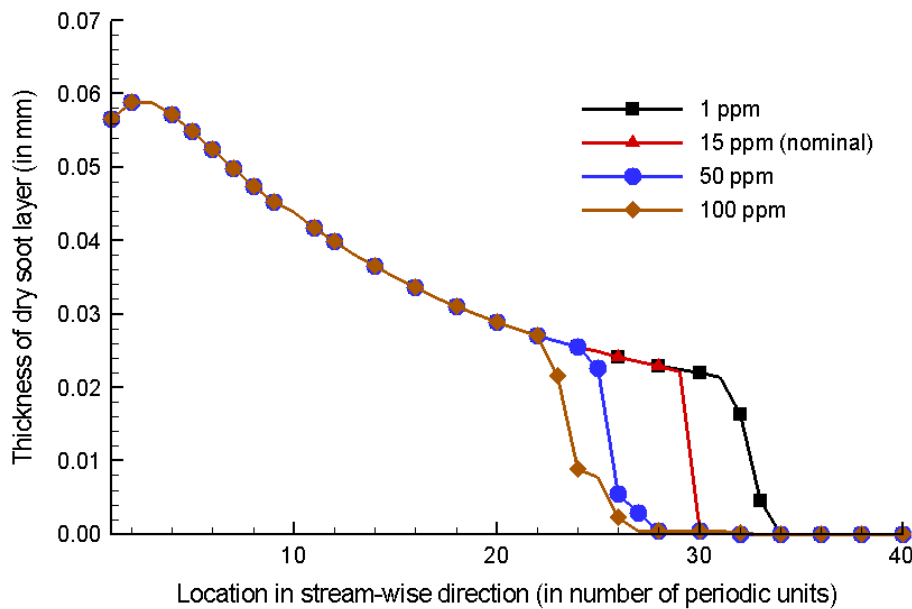


Figure 6-14 Dry soot thickness after 5 hours of operation of the EGR cooler predicted for different values of initial concentration of hydrocarbon species of fouling layer for $Re_{D_H} = 3800$

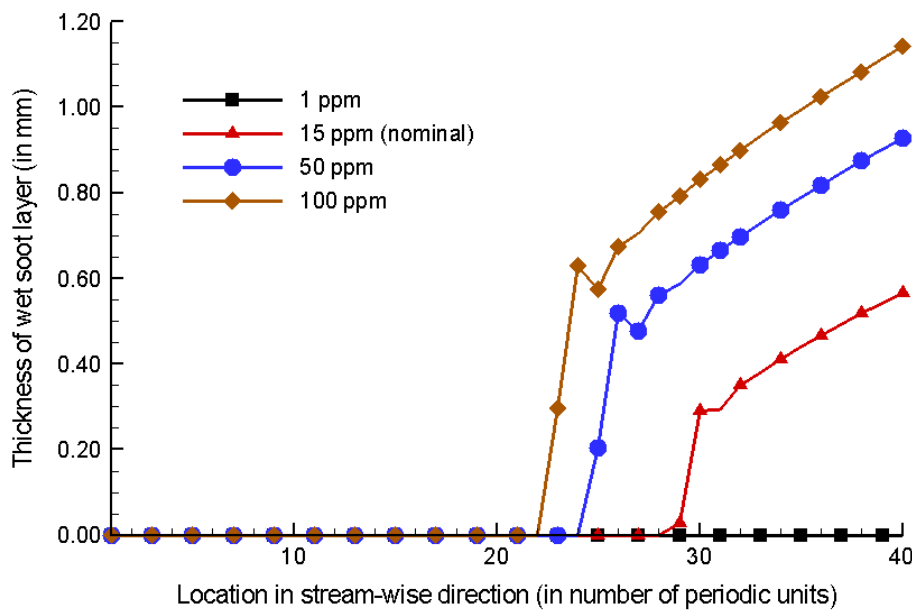


Figure 6-15 Wet soot thickness after 5 hours of operation of the EGR cooler predicted for different values of initial concentration of hydrocarbon species of fouling layer for $Re_{D_H} = 3800$

6.6 Summary and conclusions

A detailed study of the processes involved in EGR cooler fouling is undertaken. The two modes of fouling – (i) Dry soot deposition and (ii) Hydrocarbon condensation are studied in detail. For dry soot fouling, deposition correlations are used to compute the deposition fraction values for the resulting heat flux at the walls. A simple procedure to compute the amount of condensation of the heavy hydrocarbon species present in exhaust gases is described. The two aforementioned methods are combined together to present a post-processing framework to perform quasi-steady calculations and thereby provide the spatial and time growth of the fouling of EGR coolers. Various calculations are performed using the post-processing methodology to analyze the fouling process. The main conclusions from the results obtained are outlined below:

1. Dry soot fouling occurring due to the deposition of soot particles is predominantly observed in the initial parts of the EGR cooler. The wet soot layer which occurs due to the condensation of hydrocarbon species is seen mostly toward the downstream parts of the EGR cooler.
2. The maximum thickness of dry soot layer is observed near the entrance of the cooler. This trend is a direct consequence of the variation of heat flux at the walls of the EGR cooler. Likewise, a peak in the wet soot layer is observed towards the exit of the cooler where the gas attains the lowest temperature in the EGR cooler.
3. The saturation temperature for the three heavy hydrocarbon species mainly present in heavy-duty diesel exhaust is approximately in the range of 405 K to 422 K and does not vary much for the range of pressures existing in the EGR cooler. Hence, the amount of condensation can be reduced if the exhaust gas temperature is not cooled below this temperature.
4. The fouling layers exhibit considerable sensitivity to properties such as the thermal conductivity of exhaust gas and the fouling layer itself. An increase in fouling is observed for an increase in the values of these properties.

5. Increase in the inlet gas temperature results in a higher dry soot deposition due to the higher heat transfer. On the other hand, the wet soot condensation decreases and shifts further downstream due to the higher overall temperature through the EGR cooler.
6. An increase in the concentration of hydrocarbon species at inlet leads to an increase in the wet soot layer and also shifts the condensate formation further upstream. The dry soot layer remains unaffected.

It should be noted however, that the methodology involves use of certain inherent assumptions. The lack of experimental data and numerical models describing the processes involved in the fouling process necessitated the use of these assumptions. Nevertheless, the methodology enables us to study the fouling process in a broad sense and provides useful trends which govern the fouling of EGR coolers. Nature of the fouling layer growth in space and time is predicted and explained in terms of the physics involved. Certainly, improvements can be made to better predict the fouling process. A brief list of possible improvements in the methodology is given below:

1. More accurate values of the physical properties of the fouling layer (both dry and wet soot) such as density, thermal conductivity and the variation of these properties with change in layer thickness.
2. Use of temperature dependent properties for the exhaust gas since the range of temperatures existing in an EGR cooler is quite large.
3. Better modeling of the removal process of both dry and wet soot will help produce better predictions.
4. Deposition correlation that is used in the model should be able to provide deposition fraction values at lower heat flux values also, so that there need not be any approximation as to when the deposition stops. This will result in a smooth curve for the thickness of dry soot layer instead of the present one which shows sudden drop after the heat flux drops below a certain value.

Appendix A

Particle forces

Various particle forces are considered in the calculations. The non-dimensional formulations of each force acting on a particle per unit mass are provided here.

All formulations are non-dimensionalised by the fluid reference velocity and length scale U_{ref}^* and L_{ref}^* , respectively and a characteristic temperature scale T_0^* .

Viscous drag force

$$\vec{F}_{drag} = \frac{1}{Stk} (\vec{u}_f - \vec{u}_p)$$

Here, the Stokes number Stk is defined as the ratio of the particle time scale to the fluid time scale and is given by:

$$Stk = \frac{\rho_p^* \cdot d_p^{*2} \cdot U_{ref}^*}{18 \cdot C_m \cdot \mu^* \cdot L_{ref}^*}$$

Millikan's modification to Stokes' drag law to allow for slip at the particle surface is given by:

$$C_m = \frac{1}{1 + Kn \cdot \left(1.2 + 0.41 \cdot e^{-0.88} \right)}$$

where, the particle Knudsen number is the ratio of the mean free path of the carrier fluid to particle radius.

Knudsen number:

$$Kn = 2\lambda^*/d_p^*$$

Mean free path:

$$\lambda^* = \frac{2 \cdot \mu^*}{\rho_f^* \cdot c^*}$$

Mean molecular velocity:

$$c^* = \sqrt{\frac{8 \cdot R \cdot T^*}{\pi}}$$

Buoyancy force

$$\vec{F}_{buoyancy} = \frac{1}{Fr} \left(1 - \frac{\rho_f^*}{\rho_p^*} \right)$$

where, the Froude number is given by:

$$Fr = \frac{U_{ref}^*}{\bar{g} \cdot L_{ref}^*}$$

Added mass force

$$\vec{F}_{added\ mass} = \frac{1}{2} \cdot \frac{\rho_f^*}{\rho_p^*} \cdot \frac{d}{dt} (\vec{u}_f - \vec{u}_p)$$

Pressure force

$$\vec{F}_{pressure} = \frac{\rho_f^*}{\rho_p^*} \cdot \frac{d\vec{u}_f}{dt}$$

Basset force

$$\vec{F}_{basset} = \frac{9}{\sqrt{\pi}} \cdot \frac{\rho_f^*}{\rho_p^*} \cdot \frac{1}{d_p} \cdot \frac{1}{\sqrt{Re}} \cdot \int_{t_o}^t \frac{1}{\sqrt{t-t'}} \cdot \frac{d}{dt'} (\vec{u}_f - \vec{u}_p) dt'$$

Lift force

$$\vec{F}_{lift} = 5.2 \cdot \frac{1}{\sqrt{Re}} \cdot \frac{\rho_f^*}{\rho_p^*} \cdot \frac{1}{d_p} \cdot \frac{S_{ij}}{(S_{kl} S_{kl})^{\frac{1}{4}}} \cdot (\vec{u}_f - \vec{u}_p)$$

where,

$$S_{ij} = \frac{1}{2} \left(\frac{\partial u_f}{\partial x_j} + \frac{\partial u_f}{\partial x_i} \right)$$

Brownian force

$$\vec{F}_{brownian} = \vec{Z} \sqrt{\frac{2 \cdot \pi \cdot S_0}{\Delta t}}$$

where, \vec{Z} is the directional Gaussian white noise with zero mean and unit variance and S_0 is the spectral intensity is given by:

$$S_0 = \frac{216}{\pi^2 \cdot d_p^5 \cdot \left(\frac{\rho_p^*}{\rho_f^*}\right)^2 \cdot C_m} \cdot \frac{1}{Re} \cdot \frac{k_b^* \cdot T_f^*}{\rho_f^* \cdot L_{ref}^{*3} \cdot U_{ref}^{*2}}$$

Thermophoretic force

$$\vec{F}_{thermophoresis} = -\frac{36}{Re^2} \cdot \frac{1}{d_p} \cdot \frac{\rho_f^*}{\rho_p^*} \cdot \frac{1.17 \left(\frac{\kappa_f^*}{\kappa_p^*} + 2.18 \cdot Kn \right)}{(1 + 3.42 \cdot Kn) \cdot \left(1 + 2 \cdot \frac{\kappa_f^*}{\kappa_p^*} + 4.36 \cdot Kn \right)} \cdot \frac{\vec{\nabla} T_f}{T_{f0}}$$

Bibliography

1. Kittelson, D.B., *Engines and nanoparticles: A review*. Journal of Aerosol Science, 1998. **29**(5-6): p. 575-588.
2. Morawska, L., N.D. Bofinger, L. Kocis, and A. Nwankwoala, *Submicrometer and supermicrometer particles from diesel vehicle emissions*. Environmental Science and Technology, 1998. **32**(14): p. 2033-2042.
3. Messerer, A., R. Niessner, and U. Poschl, *Thermophoretic deposition of soot aerosol particles under experimental conditions relevant for modern diesel engine exhaust gas systems*. Journal of Aerosol Science, 2003. **34**(8): p. 1009-1021.
4. Lee, B.U., D. Sub Byun, G.-N. Bae, and J.-H. Lee, *Thermophoretic deposition of ultrafine particles in a turbulent pipe flow: Simulation of ultrafine particle behaviour in an automobile exhaust pipe*. Journal of Aerosol Science, 2006. **37**(12): p. 1788-1796.
5. Brock, J.R., *On the theory of thermal forces acting on aerosol particles*. Journal of Colloid Science, 1962. **17**(8): p. 768-780.
6. Talbot, L., R.K. Cheng, R.W. Schefer, and D.R. Willis, *Thermophoresis of particles in a heated boundary layer*. Journal of Fluid Mechanics, 1980. **101**(pt 4): p. 737-758.
7. Batchelor, G.K. and C. Shen, *Thermophoretic deposition of particles in gas flowing over cold surfaces*. Journal of Colloid and Interface Science, 1985. **107**(1): p. 21-37.
8. Zheng, F., *Thermophoresis of spherical and non-spherical particles: A review of theories and experiments*. Advances in Colloid and Interface Science, 2002. **97**(1-3): p. 255-278.
9. Guha, A., *Transport and deposition of particles in turbulent and laminar flow*. Annual Review of Fluid Mechanics, 2008. **40**: p. 311-341.
10. Stratmann, F. and H. Fissan, *Experimental and theoretical study of submicron particle transport in cooled laminar tube flow due to combined convection, diffusion, and thermophoresis*. Journal of Aerosol Science, 1989. **20**(8): p. 899-902.

11. Montassier, N., D. Boulaud, and A. Renoux, *Experimental study of thermophoretic particle deposition in laminar tube flow*. Journal of Aerosol Science, 1991. **22**(5): p. 677-687.
12. Munoz-Bueno, R., E. Hontanon, and M.I. Rucadio, *Deposition of fine aerosols in laminar tube flow at high temperature with large gas-to-wall temperature gradients*. Journal of Aerosol Science, 2005. **36**(4): p. 495-520.
13. Tsai, C.J. and H.C. Lu, *Design and evaluation of a plate-to-plate thermophoretic precipitator*. Aerosol Science and Technology, 1995. **22**(2): p. 172-180.
14. Romay, F.J., S.S. Takagaki, D.Y.H. Pui, and B.Y.H. Liu, *Thermophoretic deposition of aerosol particles in turbulent pipe flow*. Journal of Aerosol Science, 1998. **29**(8): p. 943-959.
15. Tsai, C.-J., J.-S. Lin, S.G. Aggarwal, and D.-R. Chen, *Thermophoretic deposition of particles in laminar and turbulent tube flows*. Aerosol Science and Technology, 2004. **38**(2): p. 131-139.
16. Li, A. and G. Ahmadi, *Dispersion and deposition of spherical particles from point sources in a turbulent channel flow*. Aerosol Science and Technology, 1992. **16**(4): p. 209-26.
17. He, C. and G. Ahmadi, *Particle deposition with thermophoresis in laminar and turbulent duct flows*. Aerosol Science and Technology, 1998. **29**(6): p. 525-546.
18. Brahim, F., W. Augustin, and M. Bohnet, *Numerical simulation of the fouling process*. International Journal of Thermal Sciences, 2003. **42**(3): p. 323-334.
19. Thakurta, D.G., M. Chen, J.B. McLaughlin, and K. Kontornaris, *Thermophoretic deposition of small particles in a direct numerical simulation of turbulent channel flow*. International Journal of Heat and Mass Transfer, 1998. **41**(24): p. 4167-82.
20. Ristimaki, J., K. Vaaraslahti, M. Lappi, and J. Keskinen, *Hydrocarbon condensation in heavy-duty diesel exhaust*. Environmental Science and Technology, 2007. **41**(18): p. 6397-6402.

21. Stull, D.R., *Vapor pressure of pure substances. Organic and inorganic compounds*. Industrial & Engineering Chemistry, 2002. **39**(4): p. 517-540.
22. Campanella, E.A., *Vapor pressure equation for heavy compounds*. Chemical Engineering and Technology, 1997. **20**(2): p. 101-107.
23. Zheng, M., G.T. Reader, and J.G. Hawley, *Diesel engine exhaust gas recirculation - a review on advanced and novel concepts*. Energy Conversion and Management, 2004. **45**(6): p. 883-900.
24. Sluder, C.S., J.M.E. Storey, S.A. Lewis, D. Styles, J. Giuliano, and J.W. Hoard, *Hydrocarbons and particulate matter in egr cooler deposits: Effects of gas flow rate, coolant temperature, and oxidation catalyst*. SAE International Journal of Engines, 2008. **1**(1): p. 1196-1204.
25. Teng, H., *Characteristics of soot deposits in egr coolers*. SAE Paper No. 2009-01-2671, 2009.
26. Kim, J., P. Moin, and R. Moser, *Turbulence statistics in fully developed channel flow at low reynolds number*. Journal of Fluid Mechanics, 1987. **177**: p. 133-166.
27. Wang, G. and S.P. Vanka, *Convective heat transfer in periodic wavy passages*. International Journal of Heat and Mass Transfer, 1995. **38**(17): p. 3219-30.
28. Niceno, B. and E. Nobile, *Numerical analysis of fluid flow and heat transfer in periodic wavy channels*. International Journal of Heat and Fluid Flow, 2001. **22**(2): p. 156-167.
29. Nishimura, T., Y. Kajimoto, A. Tarumoto, and Y. Kawamura, *Flow structure and mass transfer for a wavy channel in transitional flow regime*. Journal of Chemical Engineering of Japan, 1986. **19**(5): p. 449-455.
30. Snyder, B., K.T. Li, and R.A. Wirtz, *Heat transfer enhancement in a serpentine channel*. International Journal of Heat and Mass Transfer, 1993. **36**(12): p. 2965-76.

31. Rush, T.A., T.A. Newell, and A.M. Jacobi, *An experimental study of flow and heat transfer in sinusoidal wavy passages*. International Journal of Heat and Mass Transfer, 1999. **42**(9): p. 1541-53.
32. Oviedo-Tolentino, F., R. Romero-Mendez, A. Hernandez-Guerrero, and B. Giron-Palomares, *Experimental study of fluid flow in the entrance of a sinusoidal channel*. International Journal of Heat and Fluid Flow, 2008. **29**(5): p. 1233-1239.
33. Pham, M.V., F. Plourde, and S.K. Doan, *Turbulent heat and mass transfer in sinusoidal wavy channels*. International Journal of Heat and Fluid Flow, 2008. **29**(5): p. 1240-57.
34. Tafti, D.K. *Genidlest - a scalable parallel computational tool for simulating complex turbulent flows*. 2001. New York, NY 10016-5990, United States: American Society of Mechanical Engineers.
35. Shah, A. and D.K. Tafti, *Transport of particulates in an internal cooling ribbed duct*. Transactions of the ASME. The Journal of Turbomachinery, 2007. **129**(4): p. 816-25.
36. Rozati, A. and D.K. Tafti, *Effects of syngas ash particle size on deposition and erosion of a film cooled leading edge*, in *ASME Turbo Expo*. 2008: Estrel Berlin Hotel and Convention Center, Berlin, Germany.
37. Patankar, S.V., C.H. Liu, and E.M. Sparrow, *Fully developed flow and heat transfer in ducts having streamwise-periodic variations of cross-sectional area*. Transactions of the ASME. Series C, Journal of Heat Transfer, 1977. **99**(2): p. 180-6.
38. Zhang, L.W., D.K. Tafti, F.M. Najjar, and S. Balachandar, *Computations of flow and heat transfer in parallel-plate fin heat exchangers on the cm-5: Effects of flow unsteadiness and three-dimensionality*. International Journal of Heat and Mass Transfer, 1997. **40**(6): p. 1325-1341.

39. Rudinger, G., *Fundamentals of gas-particle flow*. 1980, Amsterdam; New York: Elsevier Scientific Pub. Co.
40. Tippayawong, N., *Analytical investigation of fine particle deposition in automotive exhaust pipes*. Thammasat International Journal Science and Technology, 2001. **6**(2): p. 57-68.
41. Incropera, F.P., *Fundamentals of heat and mass transfer*. 2006: John Wiley & Sons.
42. Chong, M.S., A.E. Perry, and B.J. Cantwell, *A general classification of three-dimensional flow fields*. Physics of Fluids A: Fluid Dynamics, 1990. **2**(5): p. 765-777.